MINES PARIS
Paris**Tech**

T H È S E

pour obtenir le grade de
Docteur de l'École des Mines de Paris
Spécialité "Informatique temps réel, robotique et automatique"

présentée et soutenue publiquement par
María Jimena COSTA

le 14 mars 2008

Segmentation de Structures Anatomiques du Bas Abdomen à l'aide de Surfaces Deformables 3D

Directeurs de thèse : Nicholas Ayache et Hervé Delingette
Equipe-Projet Asclepios, INRIA Sophia Antipolis

Jury

Jocelyne TROCCAZ, CNRS	Rapporteur
Marinette REVENU, ENSICAEN	Rapporteur
Jean–Pierre GÉRARD, C. Antoine Lacassagne	Président
Hanna KAFROUNI, Dosisoft	Examinateur
Sebastien NOVELLAS, Hôpital de l'Archet	Invité
Pierre–Yves BONDIAU, C. Antoine Lacassagne	Invité

First they ignore you, then they laugh at you, then they fight you, then you win.
– Mahatma Gandhi

Segmentation de Structures Anatomiques du Bas Abdomen à l'aide de Surfaces Deformables 3D.

Abstract: Le principal objectif de cette thèse est la conception et la production d'outils à destination des radiologues et onco–radiothérapeutes pour le contourage des organes à risque dans le cadre du traitement par radiothérapie du cancer de la prostate.

Les images testées sont des images CT. Elles sont d'abord placées dans un repère commun à l'aide d'un recalage log-euclidien concentré sur les structures osseuses du pelvis. Une suite progressive de traitements est ensuite appliquée: dans un premier temps, la vessie est segmentée, puis la prostate est ensuite localisée paralellement à la vessie, pour finir avec l'intégration de le contourage du rectum.

Compte tenu de l'hétérogénéité des images de la base de données sur laquelle nous avons travaillé, notre contribution principale est la *flexibilité*.

La vessie est une structure à forte variabilité en termes de forme et d'intensité, notamment à cause du degré de remplissage et la présence ou l'absence d'un produit de contraste. La méthode proposée s'adapte non seulement aux formes très différentes des vessies de notre base de donnée, mais aussi au degré de replissage donnant lieu, dans le cas ou un produit de contraste a été administré, une h'etérogénéité notable dans la structure à segmenter.

Le contraste de la prostate avec les tissus environnants est quasi-nul; son interface avec la vessie est souvent très difficile à distinguer, même par les experts médicaux. L'incorporation d'informations anatomiques sur la forme et d'informations images, couplée à une nouvelle contrainte d'interaction entre deux maillages, permet d'obtenir une bonne segmentation de la prostate et d'éliminer les ambiguités au niveau de l'interface entre les deux structures.

L'incorportation du rectum est l'étape la plus délicate: les différences entre les protocoles d'acquisition de la base de données utilisée interdisent toute modélisation de l'intérieur du rectum: présence de granités stercorales, insufflation d'air, présence d'un produit de contraste, présence d'une sonde etc. Les hypotheses faites sur les tissus voisins du rectum ainsi qu'une nouvelle contrainte tubulaire couplée a une pré-segmentation du squelette du rectum permettent d'obtenir un résultat probant. La chaîne de traitement qui a conduit a l'élaboration de cette thèse est en cours d'incorporation dans le logiciel Isogray produit par DOSIsoft, ce qui permet une validation plus approfondie dans des conditions cliniques.

Mots clés: Segmentation, prostate, vessie, rectum, bas abdomen, recalage non–rigide, radiothérapie.

Segmentation of Anatomical Structures of the Lower Abdomen using 3D Deformable Surfaces.

Abstract: The main objective of this thesis is to provide radio–oncology specialists with automatic tools for delineating organs at risk of a patient undergoing a radiotherapy treatment of prostate tumors.

In order to achieve this goal, we work with CT Scan images. The images are first put in a common frame of reference by means of locally–affine registration based on the pelvic bone structures. A progressive approach consisting of three stages is then applied: the bladder is first delineated, the prostate is later included, and the rectum segmentation is finally integrated.

Given the highly heterogenous nature of the images in our database, our contribution for the segmentation process is centered on *flexibility.*

The bladder is a highly variable structure, both in terms of shape (fillings, compression by surrounding organs) and of intensity levels, the latter due to inhomogeneities caused by the presence or absence (to various levels) of a contrast agent. We propose a segmentation approach that is able to automatically adapt both to the shape and, most remarkably, to the intensity variability.

The prostate shows no distinct "edge" in the image itself; its interface with the bladder is often very difficult (if not impossible) to discern, even for the trained eye of medical experts. We have incorporated anatomical information and taken the intensity similarities into account in our approach to contour this structure. An original non–overlapping constraint optimizes the result in terms of image and shape prior information, in order to avoid ambiguities in the delineation of the common boundaries.

Finally, the rectum is incorporated in the segmentation. Different acquisition protocols for the CT scans result in images containing rectums with very different characteristics in terms of shape and intensity (due to filling level and nature, air insufflation, contrast agent, etc.). A flexible method that makes no assumptions about the interior of the structure has been developped and thoroughly tested.

The developments that resulted from this thesis have been incorporated to the Isogray software by DOSIsoft, allowing further validation in clinical conditions.

Keywords: Segmentation, prostate, bladder, rectum, lower abdomen, non rigid registration, radiotherapy.

Contents

Introduction

Contents

1.1 Context

The volume of medical images that is produced has known a continuous growth for several years. Images are now a part of the clinical practice routine, and the use of three–dimensional data has become increasingly frequent, demanding in turn faster and more accurate ways for process them.

Most of the acquisition modalities for medical images are capable of producing 3D output, be it X–rays (CT), magnetic resonance (MRI), ultrasound (echography) or nuclear imaging (PET).

Three–dimensional images are often produced as a sequence of 2D slices, but the volume is not sampled at the same frequency in the three dimensions. In fact, the medical expert is confronted to a series of slices that he must mentally stack to reconstruct a volumetric representation of the observed data. This reconstruction is therefore subjective. Furthermore, manually performed image processing slice by slice entails a partial loss of information, since the third dimension is often neglected.

In order to automatically interpret medical images to aid in the diagnosis and/or geometrical modelisation of the anatomical structures, these structures must be isolated or *segmented* from the image. Given the amount of information that must be processed in 3D images to this end, it is essential to automate this task as much as possible.

This is particularly evident in the case of medical treatments that are administered through several sessions, and that require one or more images of the patient's

anatomy to be processed each time. Radiation therapy and, in particular, *three–dimensional conformal radiotherapy* (denoted 3D–CRT in this manuscript) are flagrant examples, since they involve a series of daily treatments to accurately deliver radiation to the affected structures. Before each treatment, a CT scan allows the radiation oncologist to check the location and possible extension of a tumor and adjust the radiotherapy dose to the target location as precisely as possible. Tailoring each of the radiation beams to accurately focus on the tumor allows doctors to target the diseased tissue while keeping radiation away from healthy nearby organs (organs at risk).

The prostate is the tumor site that has generated the greatest attention for 3D–CRT, largely due to its dose–response relationship, the close proximity of sensitive, dose limiting normal structures (bladder, rectum), and the high prevalence of the disease.

Since the structure(s) to be irradiated must be contoured or *segmented* as fast and as accurately as possible each time, the task becomes hardly manageable without the aid of an automatic tool.

1.2   Image Segmentation

Image segmentation, or the isolation of visible structures by the delimitation of their contours, is one of the main challenges in image analysis. In three–dimensional medical imaging, automatic segmentation becomes indispensable given the amount of data to be exploited.

The spectrum of different approaches that have been proposed to solve this problem automatically is quite broad. The segmentation task becomes even more difficult due to the sometimes mediocre quality of the images, as well as the varying contrast that may help or hinder a clear distinction of the different structures' frontiers.

Segmentation approaches may be roughly divided into two categories:

- **Direct approaches** extract the pertinent information from the image alone, while

- **Model approaches** make use of a model of the image or of the sought data itself.

The direct approach consists on the application of operations that concern the image intensities. Examples of this include thresholding techniques, mathematical morphology and region growing approaches. These operations lead to a series of transformations of the image, but they do not allow for the interpretation or the modelisation of the information contained in them. Isosurface extraction does, however, render a geometrical reconstruction of the different structures, but it needs highly contrasted or even previously segmented images.

Based on the knowledge available about the data to be treated, the model approach introduces in the segmentation process some *a priori* information about the

target. This information may include the shape, regularity, texture and environment of the sought structures.

A further distinction can be made between geometric models and image models. Geometric models include deformable models, while image models include, among others, Markov fields and Bayesian processes.

1.3 Deformable Models

Deformable models are objects that are capable of evolving in such a way as to contour or correspond to the data that is being processed. A model comprises a geometric representation and a law of evolution that guides its deformation. Deformable models are often represented by surfaces that model the border of one or many target structures. In a 2D image, it is often a contour, like the well–known "snakes" ([Kass 1988]), while in 3D images, models are often surfaces ([Terzopoulos 1988]). The evolution law is based on the establishment of correspondences between the surface and characteristic points extracted from the image.

In the presence of noisy data containing outlier points, the introduction of a model in the image segmentation process becomes key for the implementation of a reliable method that can be independent of human interaction. Medical image processing might become particularly difficult depending on the acquisition modalities and protocols involved. It is therefore important to introduce prior knowledge about the target structures. Deformable models allow for the introduction of such knowledge about the target object's shape as well as many other informations such as statistical variability, structure intensity information, etc. They can produce a direct geometric representation of the segmented objects.

In three dimensions, their surface representation is particularly adapted to the visualisation of the objects that they model (see Figure 1.1), which is one of the first requirements of medical experts. The fast development and availability, with decreasing cost, of specialized processors in the processing of graphic primitives allows for the construction of visualization tools that are both fast and accessible. Furthermore, several image processing methods including Computed Aided Diagnosis (C.A.D.) or surgery simulation rely on the interpretation of quantitative data extracted from images.

Several factors may render the process of segmentation and geometrical reconstruction of anatomical structures in medical images difficult, including image quality, and both the variability and complexity of the target structures. Image artifacts generated during the image acquisition process, low contrast and partial volume effects make the data even more difficult to interpret and cause discontinuities in the observed organ contours. Surface deformable models are therefore adapted to this problem, since they reinforce spatial coherency and directly provide a geometrical model of the segmented structures.

Many deformable surface representations have been proposed for model–based segmentation of medical images ([McInerney 1996]). In particular, **S**implex Meshes
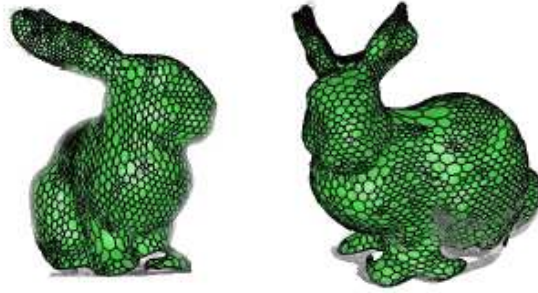
Figure 1.1: The surface representation of deformable models is useful for visualisation of the modeled objects [Montagnat 1999a].

(Figure 1.2) are discrete model representations (set of vertices and edges) with prescribed vertex connectivity. They are curves or surfaces that evolve in a 2D or 3D space to get to delimit an anatomical (or pathological) structure.
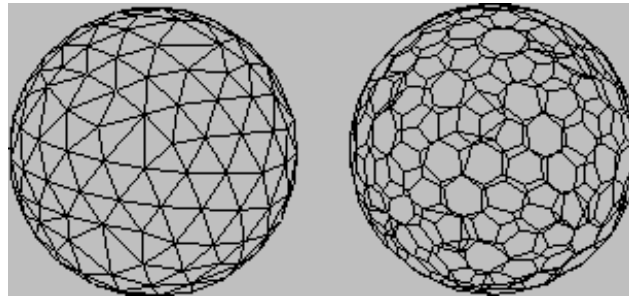
Figure 1.2:   A   triangular   mesh   (left)   and   a   dual   simplex   mesh   (right) [Montagnat 1999a].

To encode the structure surfaces, 2–simplex meshes are used: each vertex is then connected to exactly three neighbors. This inherent geometric simplicity allows for a simple approximation of the mean curvature, and greatly eases the imposition of constraints to bias the segmentation process. J. Montagnat and H. Delingette propose in [Delingette 2001] a way to combine global and local deformations in a hierarchical manner in order to improve robustness. Additionally, "zones" (subsets of vertices with their associated edges) can be defined on a simplex mesh to further adapt the constraints. This is very useful for the segmentation of structures with non–homogenous intensities.

We have focused on devising a segmentation system where maximum use is made of the available medical expertise, concerning the shape of the structures, their appeerence, etc. The desirable characteristics of the models and the constraints imposed by the variability of the target structures in our image database motivated us to choose, among existing deformable models, *simplex meshes* to represent the

organs to be segmented.

1.4 Objective

In this manuscript, we study the application of discrete deformable models to the segmentation of lower abdomen structures in 3D CT scans in the context of radio-therapy treatment planning.

We propose a segmentation algorithm and demonstrate its application to our motivating problem: the segmentation of the prostate, as well as adjacent radiation–sensitive organs (e.g., the bladder and the rectum) from 3D CT imagery, for the purpose of aiding the radiotherapy dose planning process (see Figure 1.3).
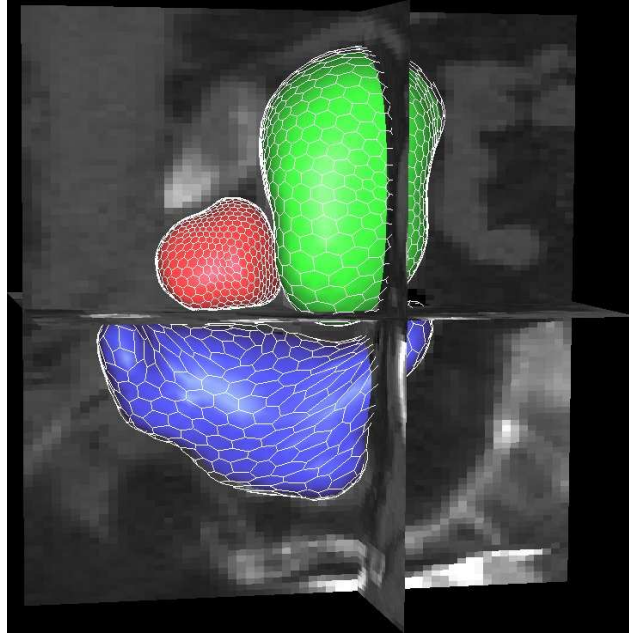
Figure 1.3: 3D view of bladder (green), prostate (red) and rectum(blue) deformable models in a CT image of the lower abdomen of a male patient.

Typically, a patient undergoing radiation therapy is treated on thirty to forty separate occasions, and the goal of the therapy is to reliably irradiate the same tissue at each session by localizing the organs of interest immediately before treatment. This is a difficult problem, since the shape and appearance of the prostate are influenced by the position, shape and appearance of the bladder and rectum, and the latter can change quite dramatically from day to day.

Manual segmentation of these structures has been attempted and is still widely performed nowadays; however, it suffers from many drawbacks. Among them, we highlight the time factor (a radiation oncologist can take 20 minutes to outline the prostate alone, while treatment sessions are typically scheduled in half–hour slots),

and inter–expert as well as intra–expert variability (interslice inconsistencies and bumps). Hence, an efficient and accurate computer vision method for automatically estimating the organ outlines in the daily CT images, using a patient–specific model and preservind 3D smoothness, would be of enormous benefit to the radiotherapy planning process.

Several more automated approaches have been proposed to solve the segmentation problem in the context of radiotherapy planning, whose advantages and disadvantages will be discussed in chapter 3. Most of these methods choose to make assumptions about the shape and/or the appearance of the target organs in the images, which limits their applicability to a certain patient preparation routine (contrast agent, probe, air insufflation, etc.) or to a subset of images generated at a particular treatment center.

In the presence of such heterogenous characteristics, and much to the contrary of other proposed approaches, we have chosen to privilege **adaptability** in our segmentation method. Our goal is to automatically adjust to different protocols, contrasts, shapes and intensities with little or no assumptions that would limit the applicability of the approach.

1.4.1   Outline

We initiate the segmentation process by putting the images in a common frame of reference. This is achieved through non–rigid registration that is not biased by the characteristics of the target structures.

Since no rigid assumptions concerning the bladder's shape or intensity are made, a characterization and subsequent approximation of the structure in each image is obtained by means of mathematical morphology tools. This characterization serves to adapt and guide a deformable model that will perform the segmentation.

As will be shown in this manuscript, the shape of the bladder influences that of the neighboring prostate. The lack of contrast makes the latter hard to distinguish, making its interface with the bladder often unclear. Their intensity similarity brings forward the need of further information, such as a shape prior, which is introduced as a factor in the deformation of a prostate model. Unnatural overlaps that may occur between the bladder and prostate models are handled through a non–overlapping constraint, and the common frontier of the two structures is established through the coupled deformation of the models. The non–overlapping constraint has been formulated to adapt to different shapes and contrast (in–)homogeneities in the shared border.

The rectum presents further challenges. The variable (and temporary) nature of its fillings renders any assumption concerning its appearance either inaccurate or overly–specific throughout treatment sessions. We have therefore chosen to approach its segmentation by isolation from its surrounding structures.

In this manuscript, our method for the segmentation of the bladder, prostate and rectum will be presented as follows:

- Chapter 2 describes the medical background concerning the radiation therapy planning in general, and more specifically in the case of prostate cancer.

- Chapter 3 is an overview of several methods proposed in the literature to address the challenge of prostate, bladder and rectum segmentation.

- Chapter 4 focuses solely on the segmentation of the bladder, with its possible intensity inhomogeneities, together with its application to our image database and the subsequent results. A new approach is proposed to first characterize and approximate the structure in terms of shape and appearance. A novel force that guides the deformation of a 3D simplex mesh so as to enforce intensity homogeneity in each zone is then developped.

- Chapter 5 details the prostate segmentation and its coupling with that of the bladder, including overlap control. A shape constraint is applied to a 3D deformable model of the prostate, and a specially devised, adaptable non–overlapping constraint helps establish a reasonable interface between the two organs. The evaluation and results of the method are also presented in this chapter.

- In chapter 6, a novel segmentation method for the rectum by means of structure isolation is proposed. To this end, the computed bladder and prostate segmentations are taken into account, and other surrounding structures are also eliminated from the images. A 3D deformable model incorporating a specifically designed tubular constraint refines and completes the segmentation. No assumption is made about the interior of the rectum, which, given its high intensity variability, allows for a broad applicability of the method to CT images acquired under different protocols and previous patient preparations.

- Conclusions that have been drawn will be presented in chapter 7.

1.5 Contributions of our work

Given the highly heterogenous nature of the images in our database, our contribution for the segmentation process is centered around **adaptability**, to both shape and intensity variability.

The **bladder** is a highly variable structure, both in terms of shape (fillings, compression by surrounding organs) and of intensity levels, the latter due to inhomogeneities caused by the presence or absence (to various levels) of a contrast agent. We propose a segmentation approach that is able to automatically adapt both to the shape and, most remarkably, to the intensity variability.

The **prostate** shows no distinct "edge" in the image itself; its interface with the bladder is often very difficult (if not impossible) to discern, even for the trained eye of medical experts. We have incorporated anatomical information and taken the intensity similarities into account in our approach to contour this structure. A

novel non–overlapping constraint optimizes the result in terms of image and shape prior information, in order to avoid ambiguities in the delineation of the common boundaries.

Finally, a **rectum** model is incorporated in the segmentation. Different acquisition protocols for the CT scans result in images containing rectums with very different characteristics in terms of shape and intensity (due to filling level and nature, air insufflation, contrast agent, etc.). A flexible method that makes no assumptions about the interior of the structure has been developped and thoroughly tested.

1.6   Publications

The work developed in this thesis has been the subject of several publications [Costa 2005, Commowick 2006, Costa 2007b, Costa 2007a, Commowick 2008].

1.7   Applications

The work described in this article was performed in the framework of the European Integrated Project MAESTRO (Methods and Advanced Equipment for Simulation and Treatment in Radio Oncology), which is granted by the European Commission. The developments that resulted from this thesis have been incorporated to the Isogray software by DOSIsoft, allowing further validation in clinical conditions.

Medical Context

Contents

We begin with some notions pertaining to anatomical and medical background of our work. Specifically, prostate cancer and several treatment possibilities, including radiation therapy, are described in sections 2.2 through 2.4. We close this chapter by explaining the motivations behind some crucial choices that we have made throughtout our work.

2.1   Anatomy of the male lower abdomen

The prostate is a gland about the size and shape of a walnut that sits under the bladder and in front of the rectum (see Figure 2.1). The urethra, the narrow tube that runs the length of the penis and that carries both urine and semen out of the body, runs directly through the prostate.
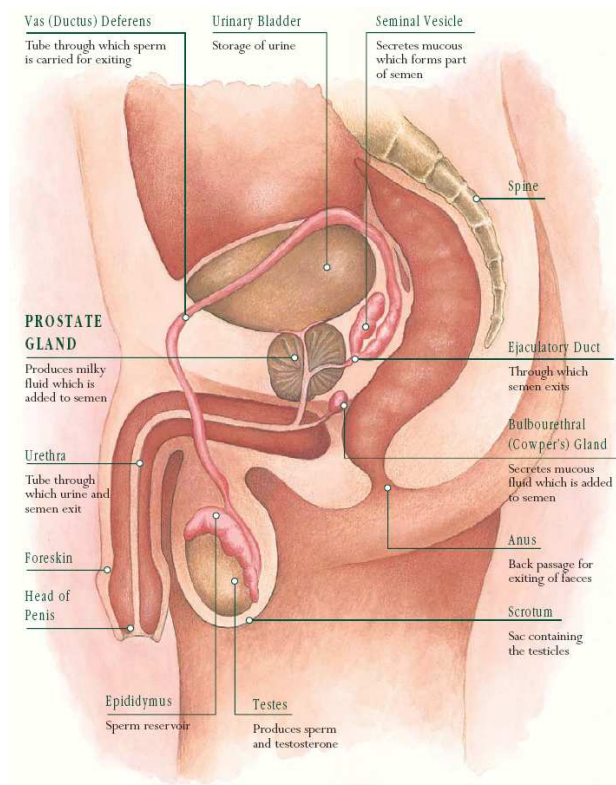
Figure 2.1: Anatomy of male lower abdomen.

The prostate produces the semen in which sperm travel. During orgasm, semen mixes with nutrients from the seminal vesicles and sperm produced by the testicles (testes). The semen then exits the body through the urethra. Testicles also produce testosterone (the main male hormone), which affects how the prostate functions.

After the kidneys filter out waste products from the blood, the resultant urine is stored in the bladder. Under normal circumstances, the urinary sphincters, bands of muscle tissue at the base of the bladder and at the base of the prostate, remain tightly shut until they are relaxed during urination.

Just above the prostate are the seminal vesicles, two glands that secrete about 60% of the substances that makes up semen.

Finally, behind the prostate and the bladder is the rectum, the lower end of the bowel just above the anal sphincter. Solid waste that is filtered out of the body moves slowly down the intestines, and, under normal circumstances, the resultant

stool is excreted through the anus following conscious relaxation of the sphincter.

2.2 Prostate Cancer

Inside the prostate, groups of cells may form benign or malignant tumors. These tumors may cause symptoms. In some cases, cancerous cells may form within the prostate but grow too slowly to cause problems. In other cases, cancerous tumors may grow inside the prostate, then spread.

- Noncancerous growths. These may grow inside the prostate as a man ages. This condition is called benign prostatic hyperplasia (BPH). These growths often squeeze the urethra, causing symptoms such as difficulty urinating.

- Precancerous cells. These cells don't appear normal, but they don't present all the characteristics of cancerous cells. They can't be felt during a physical exam and they don't produce symptoms.

- Cancerous tumors. These form most often in the prostate's outer tissue. Cancer cells may stay inside the prostate. Or they may spread to nearby organs and tissues, such as the bladder and seminal vesicles (local spread), or to the lymph nodes near the prostate (regional spread). Cancer cells can also spread through the bloodstream to more distant structures such as the bones (distant metastasis). Many early–stage tumors don't squeeze the urethra, so they may not cause symptoms. In some cases, tumors can be felt during an exam.

2.2.1 Facts About Prostate Cancer

Prostate cancer is the second most frequently diagnosed cancer in men, with 782,600 new cases projected to occur in 2007. Nearly three-quarters of these cases are expected to be diagnosed in economically developed countries. Incidence rates of prostate cancer vary by more than 50-fold worldwide (figure 2.2).

With an estimated 254,000 deaths in 2007, prostate cancer is the sixth leading cause of cancer death in men [Society 2007].

In France, prostate cancer is the most frequent cancer among men over 50 years old. In 2000 it represented 25% of the new cases of cancer in men. It is estimated that one french man out of eight will have prostate cancer during the course of his life [Grosclaude 1998], [Jemal 2002]. Facts about prostate cancer, together with its detection and treatment are also discussed in [Bondiau 2004].

2.2.2 Diagnosing Prostate Cancer

2.2.2.1 Initial Screening

Prostate cancer is most often found through a blood test measuring the amount of prostate specific antigen (PSA) in the body. Most men diagnosed with prostate cancer have no symptoms and only find their cancer due to screening.
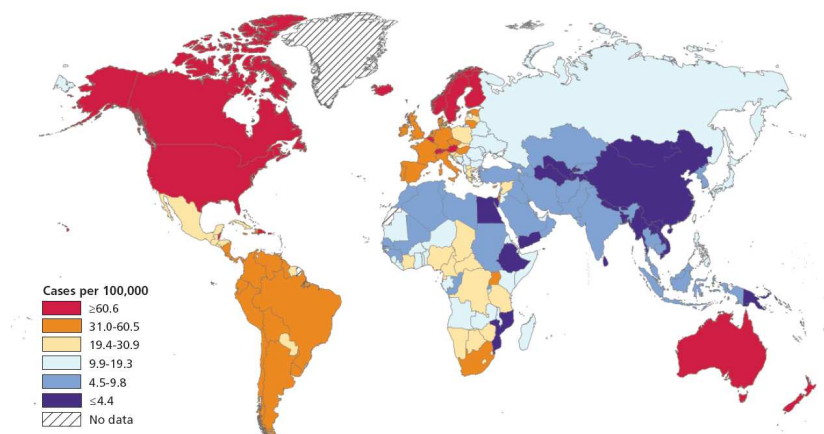
Figure 2.2: International variation in age–standardized prostate cancer incidence rates [Society 2007].

Initial screening for prostate cancer consists of a digital rectal exam (DRE) and a prostate specific antigen (PSA) test.

If either of these tests raise concerns, the doctor may perform a transrectal ultrasound (TRUS) to study the patient's prostate more closely. During this test, a small, cigar sized probe is inserted into the patient's rectum and sound waves are used to get views of the prostate gland.

2.2.2.2 Further Evaluation

If initial screening and examination suggest prostate cancer, the healthcare professional may order a prostate biopsy. During a biopsy, small tissue samples are taken and analyzed at a lab to determine if cancer cells are present. If biopsies indicate the need for further testing to determine the spread of the cancer, one or several tests may be ordered. These include:

- **CT scans** can show swollen lymph nodes or abnormalities in organs.

- **Ultrasound of surrounding tissues** may be performed to show if cancer may have spread to the nearby tissue.

- **MRI** can help look for evidence of the spread of prostate cancer to other tissues.

- **Bone scans or bone scintigraphy** are used to determine if the cancer has spread to the bones.

- **Lymph node biopsy**. One or several lymph nodes near the prostate are removed and examined for cancerous cells.

2.2.2.3 Result Analysis

Based on the results of testing, the oncologist determines the proper course of action through different steps:

- **Tumor Grading** The cancerous cells are studied to determine how aggressive they are. The samples are studied and compared with healthy prostate cells. The more difference that is found, the more aggressive the cancer cells tend to be.

- **Gleason Scoring** Biopsy samples are examined under a microscope by a pathologist to look for groups of cells making up tissue that is markedly different from healthy prostate tissue. The more different this tissue looks, the more likely the chance that it is malignant and will become aggressive and metastasize. The study involves two tissue samples for different areas of the tumor and gives each sample a score from one to five. The higher the number, the more abnormal the sample. The pathologist adds those two numbers together for that tumor to give it a number known as the "Gleason Score". A Gleason score of 2–4 (well differentiated) means that the tissue is mildly aggressive; a score of 5 to 7 indicates that the cancer is moderately aggressive. A score of 8–10 shows a very aggressive tissue. Pathologists use the term "differentiation" to describe how normal a cancer cell is. If a cell is well differentiated, it is quite normal. A poorly differentiated cell suggests that the tumor will be very aggressive and require quick and aggressive treatment.

- **Staging** is used to classify how far the cancer has spread. Cancer is assigned to one of four stages:

  * Stage I: Early cancer that is confined to a microscopic area and is too small to feel when palpated.

  * Stage II: The doctor can palpate the tumor, but it is confined only to the prostate gland.

  * Stage III: The cancer has spread to nearby tissues.

  * Stage IV: The cancer has spread to the lymph nodes, bones, lungs or other areas distant from the original tumor.

- **PSA Test** This test measures the amount of prostate specific antigen (PSA) in the blood. A rising trend in PSA test results over a period of time combined with other findings, such as an abnormal digital rectal exam, positive prostate biopsy results, or abnormal CT (computed tomography) scan results, may lead to a recommendation for further treatment. The National Comprehensive

Cancer Network (NCCN) Clinical Practice Guidelines in Oncology for Prostate Cancer [National Comprehensive Cancer Network 2007], proposes additional treatments that may be indicated based on the patient's PSA test results.

Based on this analysis, the medical expert will decide on the best treatment for the patient.

2.3   Prostate Cancer Treatment

Options for dealing with prostate cancer include:

- Surgery (section 2.3.1).

- Radiotherapy (section 2.3.2).

- Prostate brachytherapy (section 2.3.3).

- Hormone therapy (section 2.3.4).

- Cryotherapy (section 2.3.5).

Sometimes a combination of treatments is best, such as surgery followed by external beam radiation.

2.3.1   Surgery

Radical prostatectomy is an operation to remove the prostate gland and some of the tissue around it. This operation may be done by open surgery or by laparoscopic surgery through small incisions.

In *open surgery*, the surgeon uses an incision to reach the prostate gland. When the incision is made in the lower belly, it is called the retropubic approach. A radical prostatectomy using the retropubic approach is the most common treatment for prostate cancer. In this procedure, the surgeon may also remove lymph nodes in the area so that they can be tested for cancer. When the incision is made in the groin, it is called the perineal approach. The recovery time after this surgery may be shorter than with the retropubic approach. If the surgeon wants to remove lymph nodes for testing, he must make a separate incision. If the lymph nodes are believed to be free of cancer based on the grade of the cancer and results of the PSA test, the surgeon may skip the lymph node removal.

For *laparoscopic surgery*, the surgeon makes several small incisions in the belly. A lighted viewing instrument called a laparoscope is inserted into one of the incisions. The surgeon uses special instruments to reach and remove the prostate through the other incisions.

The main goal of either type of surgery is to remove all the cancer. Sometimes that means removing the prostate as well as the tissues around it. Some tumors can

be removed using a nerve–sparing technique, which means carefully cutting around those nerves to leave them intact.

Risks and complications of radical prostatectomy include:

- Excessive bleeding, the most common surgical complication, is usually the result of a blood vessel being injured during the operation.

- Bladder neck contracture, usually the result of scar tissue encircling and narrowing the bladder neck, causes a dribbling urinary stream. In a recent study of over 1000 men who had undergone radical prostatectomy, 2.8 percent reported persistent difficulty with bladder neck contracture.1 Outpatient surgery performed with a cystoscope can relax the contracture.

- Damage to rectum or ureters is rare and can usually be repaired during surgery.

- Blood clots, due to sluggish blood flow in the legs, are another rare occurrence with prostate surgery. During recovery, compression stockings help maintain a continuous blood flow in the legs. Walking after surgery is another important way to pump blood from the legs to the heart.

- Death is a risk of all surgery involving anesthesia, but an extremely rare occurrence in radical prostatectomy.

2.3.2 Radiotherapy

Radiation therapy uses controlled high–energy rays to treat malignant tumors. One of the main effects of radiation is the damage of DNA cells, making them unable to divide and reproduce, or simply die. Cancer cells are more sensitive to radiation because they divide more quickly than normal cells. Normal cells can also be damaged by radiation, but they can repair themselves more effectively.

The goal of radiation therapy is to maximize the dose to abnormal cells while minimizing exposure to normal cells (Figure 2.3). The effects of radiation are not immediate; the treatment benefit occurs over time. Typically, more aggressive tumors, whose cells divide rapidly, respond more quickly to radiation.

However, there is no gain in simply increasing the total radiation dose, since increased tumour control coupled with an equally increased complication rate yields no better therapeutic margin. The goal is to increase tumour control without increasing normal–tissue injury. It is radiation injury in normal tissues that limits the dose that can be delivered to tumors, even with the best physical 3D dose distributions.

Smaller doses per fraction (and therefore more of them) has been found to spare late complications for the same acute response and tumour effect. Using smaller doses enables higher total doses to be delivered, without increasing undesired side–effects.

Radiation is given with the intent of destroying the tumor and curing the disease (curative treatment). However, not all disease or cancer can be cured with radiation.
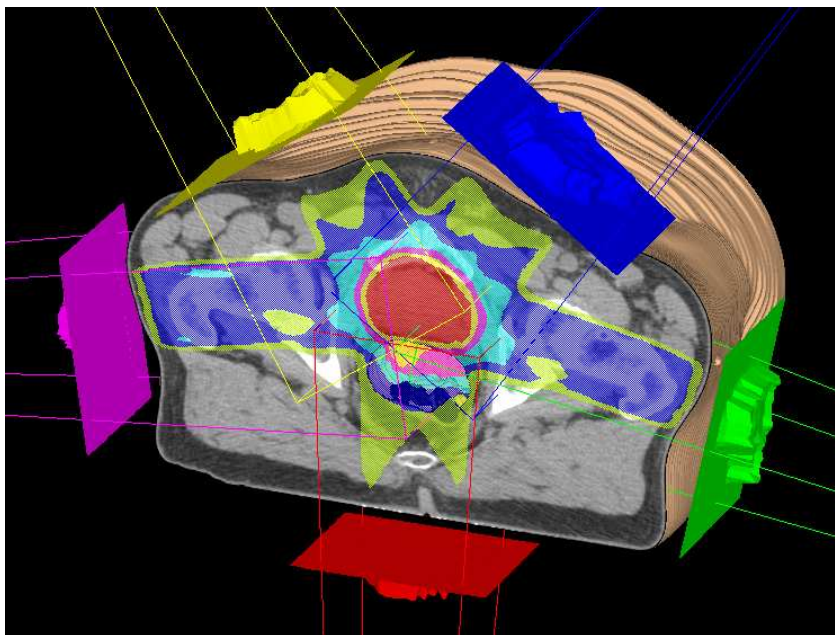
Figure 2.3: 3D view of a radiotherapy prostate treatment displaying 5 field beam arrangement and resultant dose distribution.

Sometimes radiation is used to prevent tumors from developing or spreading (prophylactic treatment, after surgery). Radiation may be used alone or in combination with other treatments such as surgery, chemotherapy or immunotherapy. If used before surgery, radiation will shrink the tumor to make it easier to remove. If used after surgery, radiation will destroy tumor cells that may have been left behind.

Further details about radiotherapy are given are given in section 2.4.

Risks of radiation therapy include:

- Urinary side effects: An increased urgency to urinate and/or a stinging sensation when urinating. These side effects can be alleviated by medication. Only rarely do more serious problems like urinary retention occur which might necessitate the temporary use of a catheter. A very small minority might experience more serious problems like urinary retention, blood in the urine and so on. This minority may require major medical intervention to deal with their problems.

- Rectal side effects: Rectal discomfort or a tendency to diarrhoea, abdominal pains or rectal bleeding. The occurrence of rectal bleeding is certainly a function of the dose and treatment at 80 Gy or thereabouts is likely to lead to about a doubling of rectal bleeding cases compared to 70 Gy treatments but the incidence is still reasonably low. Nevertheless, it does emphasise the increasing importance of more accurate targeting methods like IMRT at higher doses.

2.3.3 Prostate Brachytherapy

Brachytherapy is a minimally invasive procedure where the radiation oncologist implants tiny permanent radioactive seeds (about the size of a grain of rice) into the prostate where they irradiate the cancer from inside the gland. The implanted seeds are small enough that they will not be felt by the patient. Depending on the patient's circumstances, either radioactive Iodine (I–125) or palladium (Pd–103) will be used. Brachytherapy is also referred to as interstitial radiation therapy or seed implant therapy.
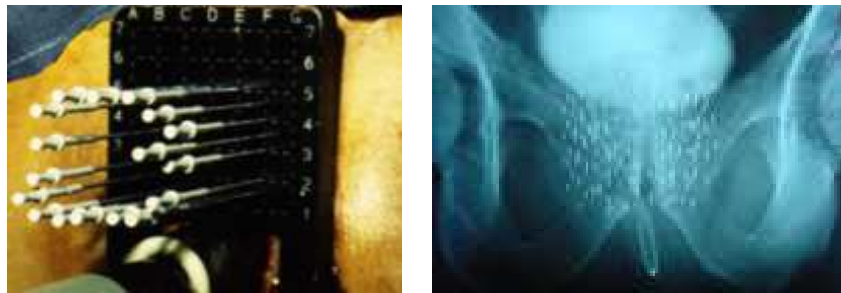
Figure 2.4: Needles containing the seeds are inserted through the skin using ultrasound guidance. A posterior x–ray of the patient shows the disposition of the implanted seeds (right handside).

Before the seeds are implanted, the patient receives anesthesia. Needles containing the seeds are then inserted through the skin of the perineum (the area between the scrotum and anus) using ultrasound guidance, as can be seen in Figure 2.4. The seeds remain in the prostate, where the radioactive material gives off localized radiation for a number of months to destroy the prostate cancer.

Seed implantation is an effective treatment for men with localized prostate cancer. It requires no surgical incision and offers patients a short recovery time. Brachytherapy can be an outpatient procedure, and most men go home the same day as their treatment. Additionally, most men can return to their normal activities a few days after treatment

Depending on the type of cancer, prostate brachytherapy may be combined with external beam radiation therapy.

2.3.4 Hormone Therapy

All prostate cells are stimulated by the male hormone called testosterone. Some types of prostate cancer cells actually require high doses of this hormone. By eliminating testosterone, hormonal therapy can temporarily slow down the growth of the prostate cancer cells but not stop it. The testicles produce 95% of a man's testosterone.

There are three basic methods of hormonal deprivation therapy:

- Orchiectomy, a surgical procedure to remove the testicles.

- LHRH therapy administers "luteinizing hormone-releasing hormone," or LHRH analogs. Usually taken orally by the patient, LHRH prevents the testicles from producing male hormone. The therapy saves the testicles and works as well as surgical castration.

- Combined androgen blockage orally administers the female hormone estrogen (or other substance) to stop the testicles from producing the male hormone.

2.3.5 Cryotherapy

The goal of cryotherapy is to eradicate prostate cancer by freezing the prostate gland. After receiving anesthesia, the doctor inserts needles into the prostate gland through the perineum, the area between the scrotum and anus. The needles produce very cold temperatures. Freezing destroys the entire prostate, including any cancerous tissue within it.

Cryotherapy uses ultra–thin needles to produce ice balls of extreme sub-zero temperatures. The doctor uses ultrasound to accurately guide insertion of the needles, precisely control the size and shape of the ice balls and monitor the freezing.

2.4 Radiation Therapy

2.4.1 Principles of radiation therapy

All types of radiation therapy follow these general principles:

1. Precisely locate the target

2. Shape the radiation beam to the target

3. Hold the target in place

4. Accurately aim the radiation beam

5. Deliver a radiation dose that damages abnormal cells yet spares normal cells

2.4.1.1 Precisely locate the target

Any tumor, lesion or malformation to be treated with radiation is called a target. When locating a target, the doctor needs to know several things: its location in the body, its size and shape, and how close it is to important organs and structures (organs at risk). Diagnostic scans such as computerized tomography (CT) and magnetic resonance imaging (MRI) have greatly improved over the years, allowing doctors to locate tumors and diseases earlier, when they are smaller. Also, positron emission tomography (PET) and functional MRI (fMRI) scans provide information about the function of critical areas next to the target.

Determining the exact location and border of a target within normal tissue is not always clear on diagnostic scans. Radiation oncologists can use a technique called stereotaxis to precisely locate targets, especially small deep ones. Stereotactic means to locate a structure by use of three dimensional coordinates (x, y, and z axis). First, a stereotactic head or body frame is attached over the target area. Next, a CT or MRI scan is taken and interpreted by computer software. The stereotactic frame shows up on the scan and helps the doctor pinpoint the exact location of the target (Figure 2.5). In some cases, stereotactic localization is performed using internal landmarks, such as bones, and a frame is not necessary.
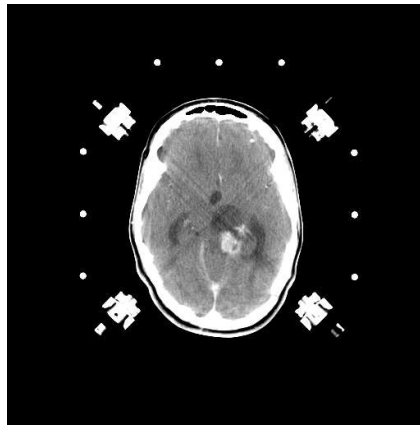
Figure 2.5: The stereotactic frame serves as a reference on the MRI scan allowing the doctor pinpoint the exact location of the target.

2.4.1.2 Shape the radiation beam

It is crucial that the radiation dose is delivered only to the target. Shaping the beam to match the target minimizes exposure to normal tissue. The problem is that most tumors are irregularly shaped and most radiation beams are round. Beams can be shaped using treatment planning software and hardware.

Treatment planning software High-end computers and software are used to plan the treatment so that all beams meet at a central point within the target, where they add up to a very high dose of radiation. The software uses the patient's CT or MRI images to form a 3D view of his anatomy and the target (Fig. 5). The radiation oncologist uses different settings in the software to create a final radiation prescription adapted to each patient. The prescription includes:

- correct radiation dose of each beam (measured in rads or Gy)

- correct size and shape of the beams

- number and angle of treatment arcs

- number of treatment sessions

Hardware . Radiation beams can be shaped by attaching blocks or collimators to the radiation machine to block a portion of the beam. The goal is to shape the beam to the exact contour of the tumor and minimize exposure to normal tissue. Block devices shape the beam in a linear fashion and are only able to squarely shape the beam (Figure 2.6). Collimator devices are able to shape the beam into circular or elliptical shapes (Figure 2.7). Multileaf collimators can focus and shape the beam in infinite ways and are the most precise method at this time (Figures 2.8 and 2.9).

Figure 2.6: Conventional radiotherapy delivers a radiation beam along a single treatment arc. It uses blocks to shape the radiation beam in a square-edged fashion.

2.4.1.3 Hold the target in place

Once the target is located, the radiation oncologist must hold the body as still as possible to accurately aim the radiation only at the target and to avoid healthy tissue. This is especially difficult in areas that are normally moving, such as the lungs and abdominal organs. Immobilization is also important for smaller targets, because a slight shift in position can move the target out of the radiation beam's path. Immobilization devices are used to prevent movement and secure the body area to the treatment table. These devices include molds, masks and stereotactic head or body frames (Figure 2.10). Molds and masks are custom-made from plastic to fit the patient's body exactly and are used during each treatment.

2.4.1.4 Accurately aim the radiation

Multiple radiation beams are aimed so that they all focus at a central point within the target, where they add up to a high dose of radiation. In order to accurately

Figure 2.7: 3D conformal radiotherapy delivers radiation beams in multiple arcs at various angles. It uses collimators to shape each radiation beam in an elliptical-shaped fashion to conform the dose to the tumor (orange).
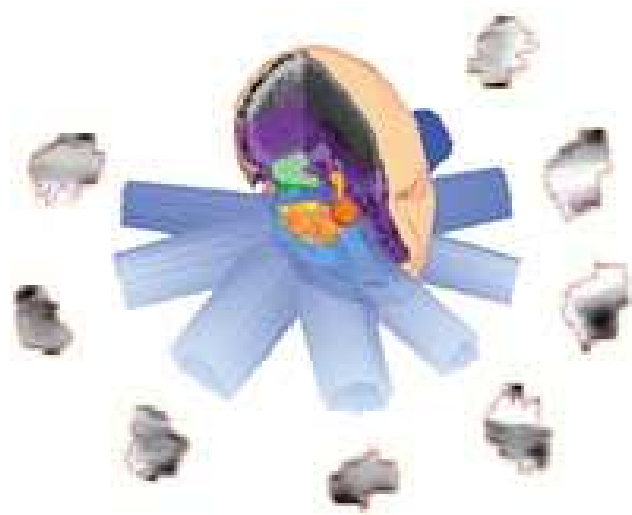
Figure 2.8: Intensity modulated radiotherapy (IMRT) delivers radiation beams in multiple arcs, similar to 3D conformal. It uses sophisticated inverse planning software and multileaf collimators to both shape the radiation beam and change the intensity within each beam to deliver the optimum dose.
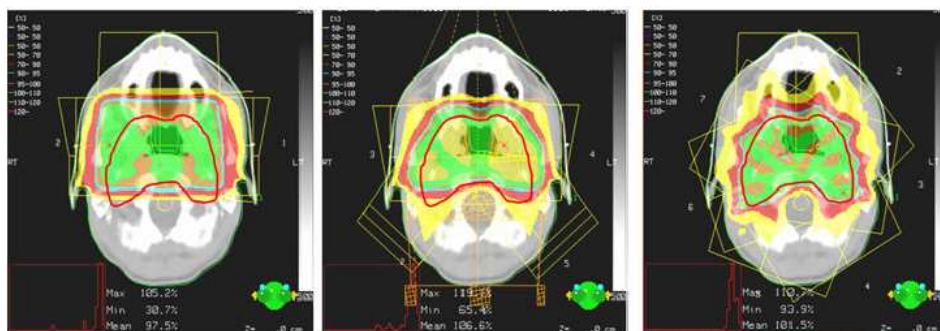
Figure 2.9: A dosimetry comparison between a 3–beam conventional 2D treatment (left), a 6–beam 3D conformal radiation treatment (center), and a 7–beam intensity modulated radiotherapy (IMRT) treatment. The Planning Target Volume (PTV) is represented by the solid red line. A better dose conformity to the PTV can be achieved in the IMRT treatment.

Figure 2.10: Immobilization devices: stereotactic frame used for treatments of the brain, head and neck (left) and body cradle for treatments of the lower abdomen (center and right). Credit to http://www.medint.de/43.0.html.

deliver radiation, both the patient and the machine must be correctly aligned with each other.

- *Patient Alignment* Depending on the body area to be treated, different techniques may be used to position the patient's body, including: skin markers, laser lights and x-ray positioners. Laser lights are used to make sure the patient is level and straight on the table. X-ray positioners take stereoscopic x-rays of the patient's anatomy and match them to the position in the treatment plan images (Figure 2.11). The Electronic Portal Imaging Device (EPID) has become an important tool for the clinician to verify the shape and the location of the therapy beam with respect to the patient's anatomy. The device uses the high energy treatment beam to project the body interior of the patient onto a fluorescent screen that is scanned by a camera. A treatment simulation takes place as a result of which a simulator image is captured. The EPI allows a verification of patient position relative to bony structures.

- *Machine Alignment* Several types of machines used to create a radiation beam and aim it at the target. Each machine offers a different level of accuracy and ability to deliver various radiation techniques to treat the target.
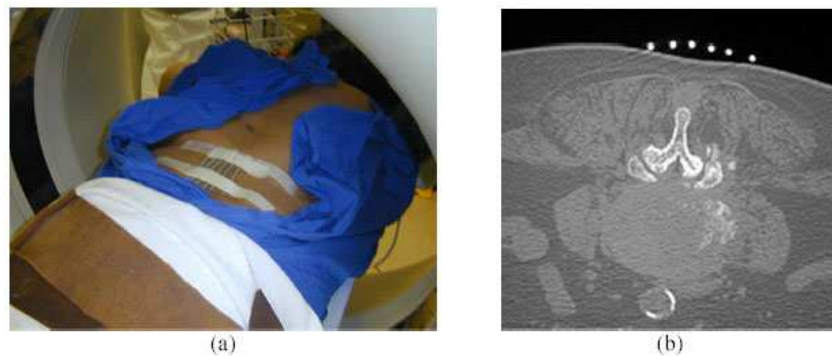
Figure 2.11: Using radio–opaque skin markers, the patient's anatomy is matched to the position in the treatment planning software to verify correct positioning.

A **Linear Accelerator** (LINAC, figure 2.12), is the most common type of radiation machine. It accelerates electrons using a specialized high–powered vacuum tube (magnetron or klystron) and a complex bending magnet arrangement which produces a beam of between 6 and 30 million electron–volt (MeV) of energy. The electrons can be used directly or they can be collided with a target (usually made of tungsten) to produce a beam of X–rays. The radiation beam produced by a LINAC can be shaped and aimed from a variety of directions by rotating the machine and moving the treatment table. The advantage of LINAC-based systems is their versatility. They:

- are used for both radiotherapy and radiosurgery treatments

Figure 2.12: Multiple beams are delivered by rotating the patient table and the gantry. Specific systems are proposed by Common LINAC, Siemens and Accuray.

- treat any area of the body

- treat large and small tumors

- use highly focused radiation sources

- produce high intensity radiation

- can use techniques such as Intensity Modulated Radiotherapy (IMRT)

The **Cyber Knife** system (figure 2.13), is an SRS system utilizing contemporary technology that is designed to be the most accurate and flexible tool available for aggressive therapeutic irradiation. The CyberKnife was designed to address the limitations of frame–based SRS systems and expands the application of radiosurgery to sites outside of the head. It is the only system to incorporate a miniature linear accelerator mounted on a flexible, robotic arm. An image–guidance system that can track target location during treatment also enables the CyberKnife to offer superior targeting accuracy without the need for the invasive head frame. While Gamma Knife and LINAC–based systems can perform stereotactic radiotherapy in the brain, true radiosurgery for areas outside of the brain is difficult if not impossible to perform with these systems. Advantages of the CyberKnife include:

- No invasive head frame or other rigid immobilization device is required

- The ability to deliver radiation (1-5 fractions) on targets throughout the body, not just the brain

Figure 2.13: The CyberKnife combines continuous image-guidance technology with a compact linear accelerator that has the flexibility to move in three dimensions according to the treatment plan (www.accuray.com).

- Precise targeting (within 1 mm) of selected lesions in the brain and body

- A unique ability to provide real time monitoring of the treated target throughout treatment using an advanced image-guidance system

- Tracking during treatment for limited target motion (e.g. due to small patient movements)

The **Gamma Knife** system uses 201 converging beams of gamma radiation (cobalt-60). All 201 beams meet at a central point within the target, where they add up to a very high dose of radiation. In contrast to LINAC, the Gamma Knife does not move around the patient. Rather, the patient is placed in a helmet unit that allows the target to be placed exactly in the center of the converging beams. The features of Gamma Knife systems include:

- used for radiosurgery only

- limited to treating head and neck lesions

2.4.1.5 Deliver an optimal dose

Radiation is most effective if a high and homogenous dose is given to the tumor while surrounding normal tissues are maximally spared. Accurate determination of the (smallest possible) volume to be irradiated is therefore essential.

To avoid ambiguity in the definition of the radiotherapy target volumes, the International Commission on Radiation Units and Measurements (ICRU) has defined a number of treatment volumes for use in RT planning ([ICR 1993, ICR 1999]). The **Gross Tumor Volume** (GTV) is the gross palpable or visible malignant growth, which is normally outlined by hand in CT or MRI slices. A margin is added around

the GTV to take into account potential "subclinical" invasion. This margin added to the GTV defines the **Clinical Target Volume** (CTV). To ensure that all parts of the CTV receive the prescribed dose, additional safety margins for geometric variations and uncertainties must be considered. The **Planning Target Volume** (PTV) is defined as the CTV plus a margin taking into consideration all possible geometrical variations of the CTV during treatment, such as internal organ motion and patient positioning errors during subsequent fractions.

The risk of missing part of the cancer cell population must be balanced against the reduction of the risk of severe and serious normal tissue complications. The balance between disease control and risk of complications often entails the acceptance of reduced probability of cure in order to avoid severe and serious treatment-related complications [Beasley 2005] (Figure 2.14).

Example scenarios are described.
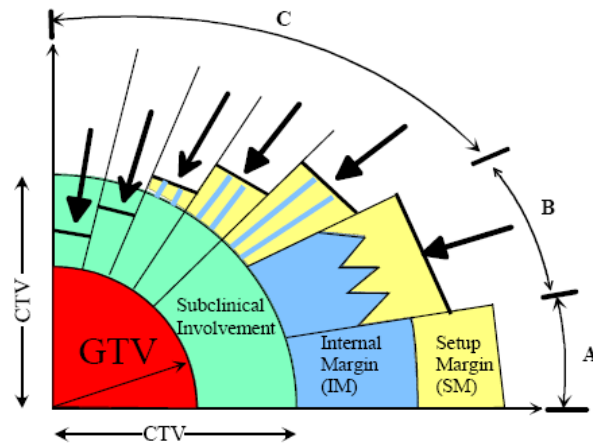
Figure 2.14: Schematic representations of the relations between the different volumes (GTV, CTV, PTV, and PRV) in different clinical scenarios.

Scenario A: A margin is added around the Gross Tumor Volume (GTV) to take into account potential "subclinical" invasion. The GTV and this margin define the Clinical Target Volume (CTV). In external beam therapy, to ensure that all parts of the CTV receive the prescribed dose, additional safety margins for geometric variations and uncertainties must be considered. An Internal Margin (IM) is added for the variations in position and/or shape and size of the CTV. This defines the Internal Target Volume. A Set–up Margin is added to take into account all the variations/uncertainties in patient-beam positioning. CTV + IM + SM define the Planning Target Volume (PTV) on which the selection of beam size and arrangement is based.

Scenario B: The simple (linear) addition of all factors of geometric uncertainty, as indicated in Scenario A, often leads to an excessively large PTV, which would be incompatible with the tolerance of the surrounding normal tissues. In such instances, instead of adding linearly the Internal Margin and the Set Up Margin, a compromise has to be sought and a smaller PTV has to be accepted.

Scenario C: In the majority of the clinical situations, a "global" safety margin is adopted. In some cases, the presence of Organs at Risk dramatically reduces the width of the acceptable safety margin (e.g., presence of the spinal cord, optical nerve, etc.).

Organs at Risk The compromise to be accepted when delineating the PTV is due to the presence of **Organs at Risk**. Such organs at risk are normal tissues whose radiation sensitivity and location in the vicinity of the CTV may significantly influence treatment planning and/or absorbed dose level. A dose above the tolerance limit, even to a small volume, might totally impair the function of certain organs, as is the case with the spinal cord (myelitis). A precise delineation of the Organs at Risk is of vital importance.

Therefore, and as for the CTV, movements and changes in shape and/or size, as well as the set-up uncertainties, must be considered for the organs at risk.

2.4.2 Dose–Volume Histograms and Isodose lines

The purpose of the Dose–Volume Histogram (DVH) is to assist the physician in evaluating the selection of complicated treatment plans and objectively determining the ideal plan for a given patient by summarizing the 3–D dose distribution data for the organs at risk (OAR) in the treatment volume and displaying it in a graphical format.

In a DVH, the variables are the dose received by the patient (measured in **Grays**) and the volume(s) of tissue receiving any dosage. These can be visualized in either of two ways; through "cumulative" ("integral") or "direct" ("differential") dose–volume histograms. The direct DVH is a histogram of the dose bins and the frequency of occurrence of each dose. (Figure 2.15, left and center) These are not frequently used in plan evaluation.

Rather, the cumulative DVH is most frequently utilized (Figure 2.15, right). In this type of DVH, the vertical axis can represent the percent of total tissue volume that receives a dose greater than or equal to a specified dose. The horizontal axis, however, represents cumulative dose. For example (Figure 2.16, left), the first bin displays the volume of tissue that received at least zero Gray (Gy), 100 percent; the second bin displays the volume that received at least 1Gy, 99 percent; etc. DVHs can also be specified in terms of total volume. Ideally, the DVH displays 100 percent of the planning target volume (PTV), receiving 100 percent of the prescribed dose and very low volumes of normal structures receiving very little dose (Figure 2.16, right).
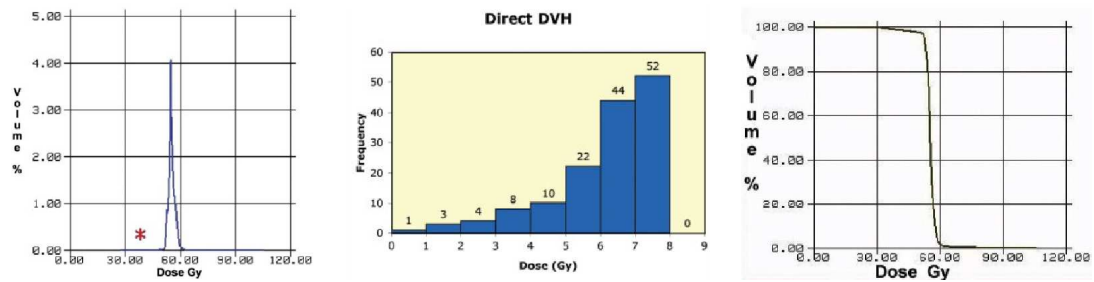
Figure 2.15: Different dose–volume histograms (DVHs).
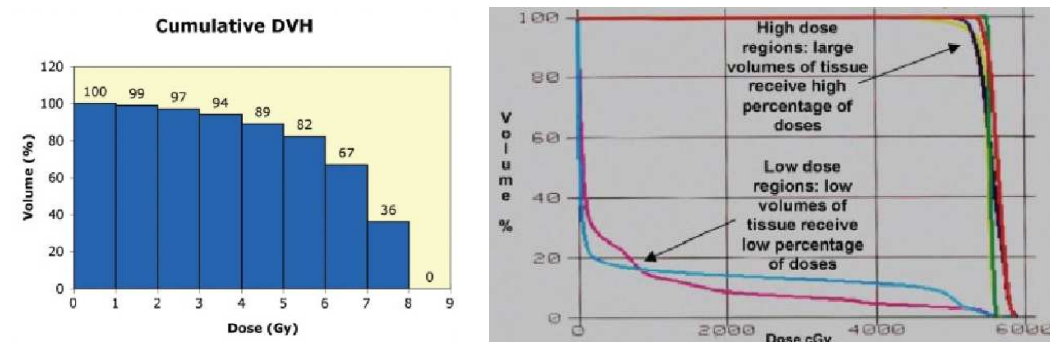
Figure 2.16: Cumulative dose–volume histograms (DVHs).
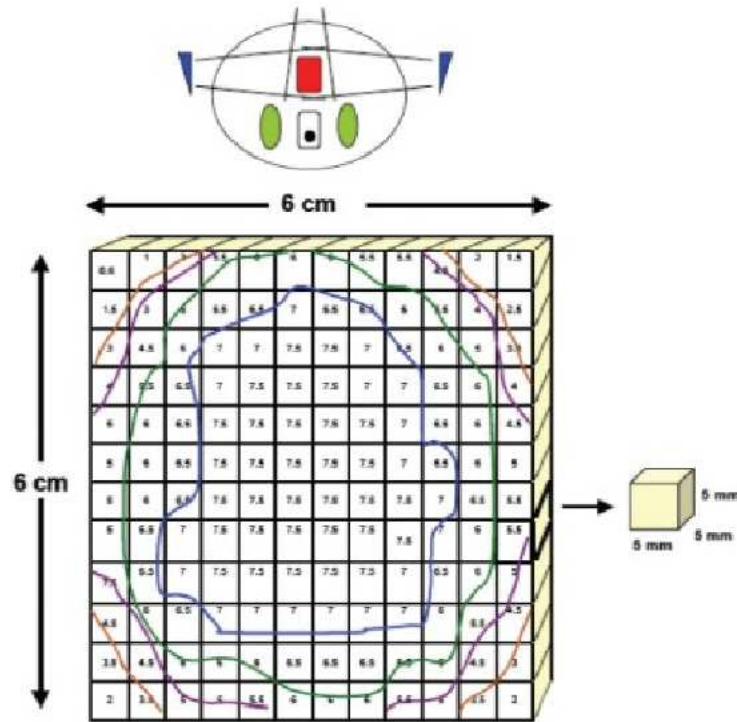
Figure 2.17: Isodose lines.

For the DVH to be calculated, the volumes of interest are outlined on each contiguous and parallel slice of a given patient's CT scan. The anatomy is then divided into a volume grid. By defining the grid's matrix size, the resolution is defined. This, in turn, establishes the volume elements – or voxels – for the identified anatomy; the volume being the product of the three dimensions of the voxel (Figure 2.17).

2.4.3 Radiotherapy for prostate carcinoma

Dose escalation has shown to be effective in radiotherapy treatment of prostate cancer. Especially intermediate risk patients benefit from high, concentrated doses (higher than 70Gy) [Kupelian 2005]. Because prostate cancer is often found to be multifocal, the entire gland is commonly considered the gross tumor volume for radiation treatment planning purposes [Michalski 2006].

Rectal and bladder toxicity are the main limiting factors in dose escalation [Schultheiss 1997]. The Patterns of Care Study stated that the incidence of severe rectal and bladder complications almost doubled when dose levels were increased beyond 70Gy with conventional treatment [Leibel 1984]. Three dimensional conformal radiotherapy (3D–CRT) in comparison to conventional radiotherapy resulted in lower rates of late rectal toxicity [Dearnaley 1999a] and allowed the safe administration of doses up to 80Gy. Intensity–modulated radiotherapy (IMRT) has been

indicated to be beneficial in comparison with 3D–CRT and made further dose escalation to 86.4Gy possible [Zelefsky 2002].

The improvements from conventional RT to 3D–CRT and from 3D–CRT to IMRT are due to more conformal dose distributions with the high dose region confined to the target volume and sparing of organs–at–risk [Oh 1999, Zelefsky 2000]. The correlation between the volume of the rectum within the high dose region and the risk for late rectal toxicity suggested a dose volume effect [Lee 1996a].

Reliable tools for a robust delineation of the prostate, bladder and rectum are therefore essential for a successful treatment plan.

2.4.4   Adverse Effects and Quality of Life

Despite advances such as 3-dimensional conformal radiotherapy and intensity-modulated radiotherapy, the bladder and rectum still sustain scatter radiation.

The adverse effects of external beam radiotherapy often are grouped into 3 major categories: bowel, urinary, and sexual. Adverse effects may be **acute** (occurring during or shortly after external beam radiotherapy) or may persist or appear several months after treatment is completed (**chronic**). The distinction between acute and chronic is made from the time frame during which the adverse effect is experienced, with chronic conventionally defined as more than 90 days from initiation of external beam radiotherapy. The incidence and severity of adverse effects is influenced by several factors, including coexistent medical conditions (i.e., diabetes), prostate localization accuracy, treatment technique (ie, conventional external beam radiotherapy, 3D-CRT, or IMRT) [Zelefsky 2001, Dearnaley 1999b, Ryu 2002, Michalski 2003] dose conformity to the prostate, and the radiotherapy dose level and volume of the structure that is irradiated (ie, the dose-volume relationship) [Pollack 2002]. Thus, the likelihood of complications can be mitigated by treatment planning that considers these factors.

2.4.4.1   Bowel Toxicity

Acute bowel toxicity may begin after the first few weeks of external beam radiotherapy and manifests as acute enteritis from its effect on the small intestine (when the pelvic lymph nodes are included in the treatment field) or the rectum. The severity of this adverse effect is proportional to the volume of irradiated bowel. Serious long-term bowel complications may occur in a small proportion of patients and may manifest as diarrhea, proctalgia, mucous discharge, or hematochezia; anorectal strictures, obstruction, ulceration, or perforation are decidedly uncommon. Lawton et al [Lawton 1991] found that 3% of patients treated more than 2 decades ago in 2 large-scale prospective trials experienced moderate or severe bowel sequelae. However, diarrhea and proctopathy are self-limited in half of patients within the first year, and nearly three quarters resolve within 2 years [Pilepich 1988]. Recent studies showed that considerably higher doses (78-81 Gy) given with 3D-CRT techniques resulted in either no or minimal long-term morbidity in approximately 90% of patients,

with severe toxicity limited to 1% of patients [Zelefsky 2001, Ryu 2002]. Restricting the volume of rectum exposed to more than 70 Gy and using IMRT were associated with a reduced risk of long-term complications [Zelefsky 2001, Pollack 2002].

2.4.4.2 Urinary Toxicity

Most patients experience some degree of urinary morbidity during external beam RT. Cystitis is caused by irritability of the bladder detrusor musculature or inflammation of the urothelium and is characterized by urinary urgency, frequency, or dysuria. Prostatic edema may aggravate preexistent urinary retention from benign prostatic hypertrophy, which may lead to urinary hesitancy, diminished force of stream, or incomplete voiding. These symptoms often are lessened with short–term use of medication (e.g., tamsulosin) and typically resolve within 2 to 3 weeks after treatment is completed. Chronic urinary complications are uncommon, but bladder neck contracture and reduced bladder capacity may result in urinary urgency and frequency. Bladder neck contracture or urethral stricture may cause urinary retention, and submucosal bladder or urethral telangiectasia may produce hematuria. Lawton et al [Lawton 1991] concluded that approximately 8% of patients experienced moderate or severe chronic urinary toxicity. Nonetheless, more than half of these complications were urethral strictures, which generally can be dilated on an outpatient basis, and most patients experience spontaneous resolution within a year of symptom onset [Pilepich 1988]. These observations were confirmed in more contemporary series in which doses of 79.2 to 81.0 Gy were used [Zelefsky 2001, Ryu 2002]. Urinary incontinence is uncommon after external beam RT; Lee et al [Lee 1996b] reported a rate of 1.3% at 5 years with a greater likelihood among patients who underwent prior transurethral prostatic resection (2% vs 0.2%).

2.4.4.3 Sexual Function Side–effects

Assessment of sexual function after external beam radiotherapy is complex and may be fraught with inaccuracy due to the limitations and variations in the definition of erectile dysfunction and the methods used to establish its presence and origin. Some patients have compromised erectile function due to concurrent illnesses such as diabetes mellitus or arteriosclerosis or from certain medications taken for these or other conditions. As summarized by Robinson et al [Robinson 1997] the likelihood of maintaining erectile function after radiotherapy ranges from 20% to 86%, depending on the definition of potency and the institutional report. It appears that the primary etiology of RT-induced erectile dysfunction is from a disruption in the vascular system of the penile corporal structures [Zelefsky 1998]. The proportion of the corpus spongiosum that receives various radiotherapy dose levels is associated with erectile dysfunction [Roach 2004, Wernicke 2004]; therefore, measures that reduce radiotherapy dose to these structures lessen the risk of dysfunction [Roach 2004, Wernicke 2004].

Unlike reports of complication rates, health-related quality of life refers to the

physical, psychological, and social domains of health that are influenced by a person's experiences, beliefs, expectations, and perceptions. These domains typically concentrate on items relevant to sexual, urinary, and bowel dysfunction [Altwein 1997]. Several publications describe quality-of-life outcomes in patients who underwent external beam radiotherapy [Wei 2002, Clark 2003, Potosky 2004] for localized prostate cancer. Most reports identified patients from a medical institution's cancer registry, applied various restrictions for study inclusion, and mailed questionnaires to potential study participants as a 1–time investigation. Many such efforts were compromised by the study design, leading to uncertainty in interpretation and clinical application of the results. Furthermore, the demographic features, overall state of health, and baseline symptom status influence the type of treatment rendered [Clark 2003, Potosky 2004] , which makes it difficult to compare the effects of various treatments on quality of life.

Accurate delineation methods could greatly help to reduce these side effects, with a significant impact on the the patient's quality of life.

2.5   Motivations behind our proposed method

The aim of our work is the development of a fast, automatic approach that allows the treatment planning time to be accelerated as much as possible. This would alleviate the work load of the medical experts in the delineation process, reduce the patient's waiting time before each treatment session, and augment the accuracy of the radiation therapy, resulting in an improvement of the patient's quality of life and a reduction of possible side effects.

We have therefore designed and implemented a fully automatic method for the localization and (coupled) delineation of the prostate and its organs at risk and in CT scans (section of the lower abdomen of patients undergoing radiation therapy. The approach must be adaptable and, if needed, the result may be manually improved by a medical expert. The motivations behind this are explained in the next subsections.

2.5.1   Why Automatic Delineation (vs. Manual Segmentation)

The day–to–day positional changes in the target volumes of cancers such as prostate, bladder, and rectum, can be a limiting factor in a radiation therapy treatment. This is particularly true for dose escalation, whose effects rely heavily on the delineation of the target structures as well as the organs at risk. In the case of prostate cancer, the characteristics of the organs at risk (bladder, rectum) are highly variable and have an important influence on the shape and location of the target organ itself (prostate). The variability of these soft tissues includes shape, size and intensity, the latter depending on the presence (partial or total) or absence of a contrast agent.

The segmentation task has traditionally been assigned to medical experts. However, manual editing is not only tedious and time consuming, but also particularly prone to variability and errors [Gao 2007].

Semi–automatic or interactive approaches for segmentation allow the pratician to have better control over the segmentation process [Freedman 2005a, Lee 2004]. However, they remain time consuming and, especially for large databases, an automatic approach is desirable.

2.5.2 Why coupled deformation? Influence of Bladder and Rectum shape on Prostate

Several studies have been carried out to assess the movement and deformation of the prostate caused by its surrounding organs (bladder and rectum)([Melian 1997, Crook 1995, Haken 1991, Schild 1993]).

Organ displacements from each patient are combined to form a data set from which a mean organ displacement (MODorgan) is calculated with corresponding standard deviation. MODprostate values of 1 to 8 mm, due to rectal and bladder distension, were measured by Ten Haken et al[Haken 1991] using the centre of mass of the prostate derived from CT images. Greater movements of a Foley catheter balloon (i.e. 0 to 20 mm) due to rectal and bladder distension were also measured. The effects of rectal wall and bladder movement have been separately measured using CT images[Schild 1993]. A 3D CT scan registration method based on Chamfer matching has been used to quanty the correlations between rectal filling, leg motions, and prostate motion during conformal therapy of the prostate in [van Herk 1995]. In the study, a strong correlation was found between rectal volume and anterior–posterior translation and rotation around the left–right axis of the prostate. Bladder filling, leg and pelvic rotations were found to have much less influence on prostate motion.

Given the neighbouring position and the marked interaction between bladder, prostate and rectum deformations, a joint study of these organs is the natural direction for segmentation purposes.

2.5.3 Why Prostate, Bladder and Rectum?

A precise delineation of the treatment volume as well as the organs at risk in the frame of radiotherapy dose planning is of vital importance.

In the radiation treatment planning for prostate carcinoma the entire prostate gland is commonly considered the Gross Tumor Volume. Since the organs at risk (OARs) in this case are the bladder and rectum, our study comprises the delineation of the three of them.

2.5.4 Why CT Scans and not MRI?

CT scans have various uses in the context of cancer detection and treatment. They can be used as a tool to aid diagnosis of a problem; the radiographer may spot something during an ultrasound scan which needs a closer look – the CT scan can offer a more detailed picture. A series of CT scans at different stages of radiotherapy treatment can be used to assess the response of a tumour to that treatment, giving

the radiographer and oncologist a series of "before" and "after" pictures of the patient's body. The CT scanner is also used prior to starting a course of radiotherapy, to help the specialist plan a course of radiotherapy, i.e. deciding exactly where to aim the radiotherapy X–rays, and at what intensity. During the planning CT scan some indelible marks may be put on the patient's skin to ensure a perfect alignment under the radiotherapy machine for each session. Furthermore, since a CT scan's information is based on the density of the tissues, it may be directly "fed" to the machine that performs the dose calculation in the radiation treatment planning.

The X–Ray attenuation unit used for CT Scan voxel intensity determination is called a *Hounsfield Unit*. It characterizes the relative density of a substance. Each pixel is assigned a value between -1000 to +1000. These standards were chosen as they are universally available references and suited to the key application for which computed axial tomography was developed: imaging the internal anatomy of living creatures based on organized water structures and mostly living in air, e.g. humans. Common substance densities are shown in Table 2.1.

Substance	Density in H.U.
Air	-1000
Fat	-50
Water	0
Soft tissue such as muscle	+40
Soft tissue with contrast agent	+200 to +1000
Calculus	+100 to +400
Bone	+1000

Table 2.1: Substance densities in Hounsfield Units

Contrary to CT scans, the use of MRI for treatment planning in patients with prostate cancer is quite limited. This is owing to the lack of tissue density information for the correction of inhomogeneities used in dose calculation as well as to the presence of intrinsic system–related and object–induced image MR distortions [Khoo 1999].

It could indeed be useful to incorporate both the information in CT scans and in MRI images. The registration of both image modalities has been studied, in the frame of prostate segmentation for radiotherapy planning, in [van Herk 1998, C.C. 2003, van Dalen J.A.] among others. Although interesting, the frameworks are not directly applicable in our case, due to the high variability in tissue appearance, as well as the geometric uncertainties of MR reconstruction.

For the above reasons, we have based our studies on CT scans.

2.5.5 Why Adaptable? Variability in the target structures

As shall be precised throughout the chapters, the segmentation of the prostate, bladder and rectum is very challenging. All three of them are soft tissues, which entails
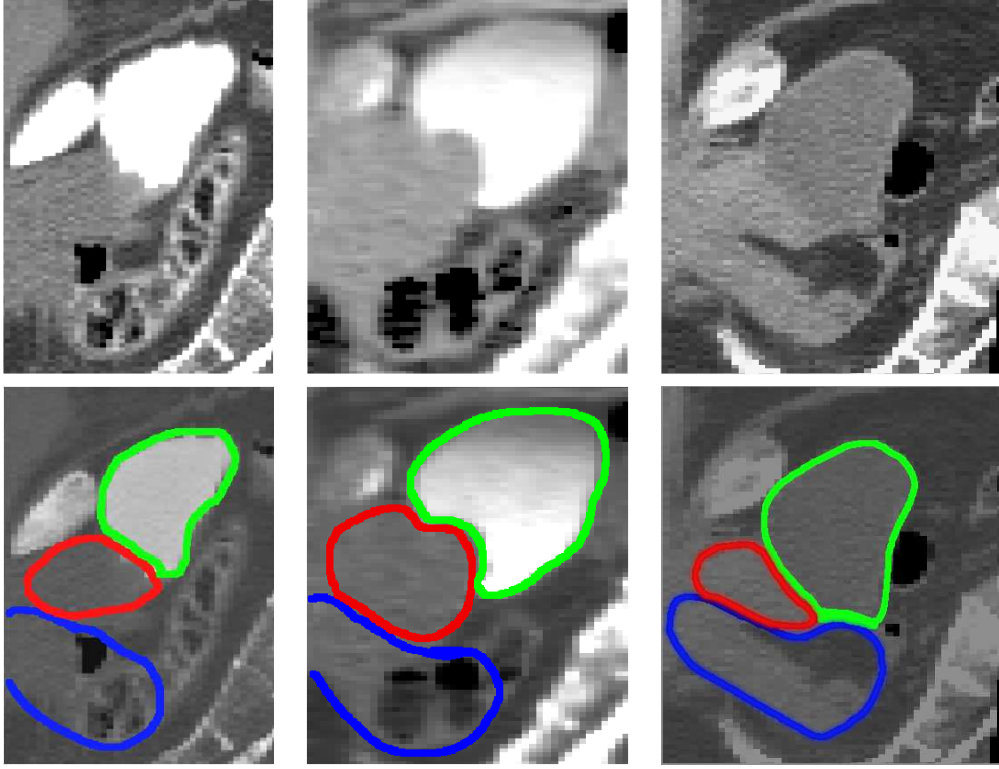
Figure 2.18: Different bladder characteristics make the segmentation task challenging and have an influence on the prostate. From left to right: homogenous contrasted bladder, non–homogenous bladder and homogenous non–contrasted bladder (sagittal views). For illustrative purposes, the second row shows the same images with the target organs outlined in blue (rectum), red (prostate) and green (bladder).

a large variability in *shape* (knowing that they influence each other's shapes, as seen in section 2.5.2). The bladder's and rectum's fillings change among patients, and within the same patient throughout the day (see figures 2.18 and 3.6). Furthermore, different patient preparations may have been carried out before the image acquisition process (contrast agent administered to the bladder or not, air insufflation for the rectum, the presence or absence of a probe, variability in the fillings). These factors greatly influence the *size, shape and appearance* (intensities, homogeneity) of the structures. Since the three structures are neighbors, they have borders or frontiers that touch. Consequently, the size, shape and appearance of one organ influence the characteristics of its neighbors and or their touching borders.

In chapter 3 we will show that authors have chosen to address these challenges by proposing different approaches. Interestingly, hypotheses are often made concerning the characteristics of the structures. The more assumptions they make, the more restricted the applicability of their method becomes.

We, on the other hand, have taken the problem of structure variability as a challenge: **adaptability** has been fully incorporated into our goals. We would like
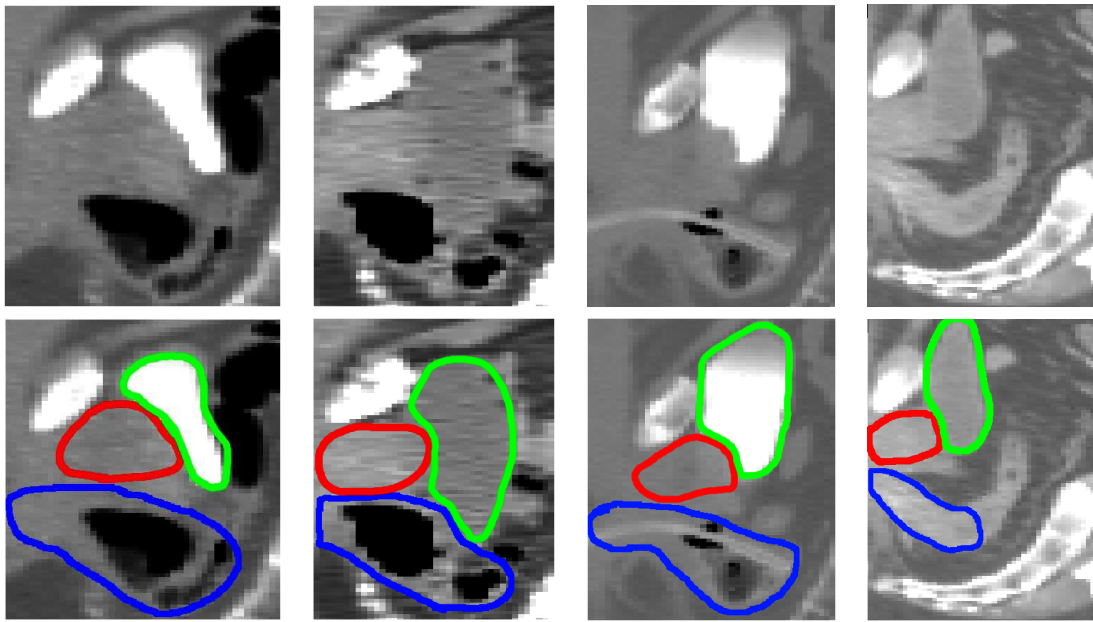
Figure 2.19: Different rectum characteristics make the segmentation task challenging and also have an influence on the prostate. In the first row, sagittal views of rectums with heterogenous fillings (left), air insufflation (center left), presence of both a probe and a slight contrast agent (center right), and one almost empty (right). For illustrative purposes, the second row shows the same images with the target organs outlined in blue (rectum), red (prostate) and green (bladder).

to be able to automatically adapt to different bladder, prostate and rectum shapes and appearances, without hindering the quality of the segmentation result.

Each organ we have targeted presents specific challenges that will be addressed in detail in chapters 4 (bladder), 5 (prostate) and 6 (rectum).

2.6 What's next

Before proceeding to fully develop our approach (chapters 4 to 6), we review in the next chapter several approaches that have been proposed to deal with some or all of the challenges that we face.

Lower Abdomen Segmentation Methods

Contents

    In this chapter, we introduce several families of methods that can be applied to the segmentation problem. Section 3.1 gives a general description, while section 3.2 shows how they have been applied to the problem that interests us, i.e., the segmentation of lower abdomen structures. The advantages and disadvantages of the methods when applied specifically to the segmentation of the bladder, prostate and rectum will be detailed in section 3.2.

3.1 Overview of Segmentation Methods

We briefly describe several common approaches that have appeared in the literature on medical image segmentation. A comprehensive review on the subject can be found in [Sonka 2000].

A wide variety of image properties can be used to guide the segmentation process, such as intensity, edges, and texture. In addition to information derived from the image, prior knowledge can also be incorporated to further improve performance. According to the use of these informations, segmentation methods may be grouped into several families:

1. Manual segmentation approaches,

2. Thresholding approaches,

3. Classifiers,

4. Clustering approaches,

5. Markov random field models,

6. Artificial neural networks,

7. Deformable models, and

8. Atlas–guided approaches.

3.1.1   Manual Segmentation Approaches

Because of the difficulty to accurately and reliably delineate structures in medical images, this task has traditionally been assigned to human operators. However, given the improvements achieved over the past years by imaging tools (commercial MR scanners now routinely resolve images at millimetric resolution, digital cameras can convert histological sections into million-pixel images) the manual segmentation phase has become an intensive and time–consuming task. A trained operator typically has to go through around eighty 256x256 images, slice by slice, to extract the contours of the target structures, one after the other. This manual editing is not only tedious but particularly prone to errors, as assessed by various intra or inter-operator variability studies ([Collier 2003, Saarnak 2000, Fiorino 1998] among others). The results are often difficult if not impossible to reproduce; even experienced operators display significant variability with respect to their own previous delineation for difficult structures, as illustrated in figure 3.1.

For 3D delineation, editing tools usually display 3D data in the form of a 3 synchronized, 2D orthogonal views (sagittal, coronal and axial) onto which the operator draws the contour of the target structure. The output data therefore consists of a series of 2D contours from which a continuous 3D surface has to be extracted. This is a non–trivial post–processing task, itself prone to errors. Moreover, since the operator has to mentally reconstruct the 3D shape of the structure from a series of 2D views, interslice inconsistencies and bumps are inevitable (see figure 3.1). More robust segmentation methods can usually be derived from true 3D structure models in that they can ensure globally smoother and more coherent surfaces across slices.
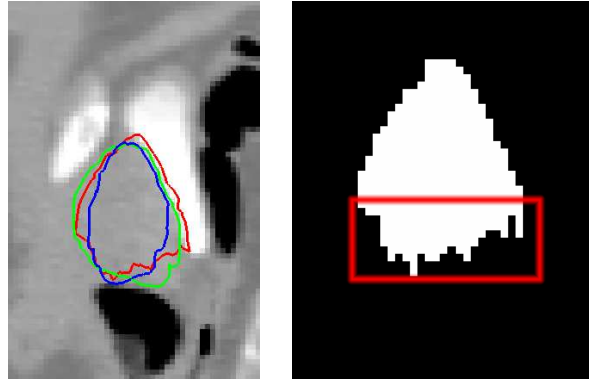
Figure 3.1: Sagittal view of three experts' delineations of the prostate in the same image (left). Since the delineation is usually performed slice by slice in the axial plane, inter–slice bumps and inconsistencies are visible in the other planes (sagittal plane inconsistencies outlined in red on the right).

3.1.2 Thresholding and Image–Processing

A *thresholding* procedure attempts to determine an intensity value, called the threshold, which separates the desired classes. The segmentation is then achieved by grouping all pixels with intensity greater than the threshold into one class, and all other pixels into another class. The partition is usually generated interactively, although automated methods do exist [Sahoo 1988, Sezgin 2004]. Thresholding typically does not take into account the spatial characteristics of an image; this causes it to be sensitive to noise and intensity inhomogeneities.

The *watershed* algorithm uses concepts from mathematical morphology [Gonzalez 1992] to partition images into homogeneous regions [Vincent 1991]. It can be considered as a thresholding applied to gray-level images, which are interpreted as topographic surfaces (i.e., "height maps"). This method can suffer from oversegmentation, which occurs when the image is segmented into an unnecessarily large number of regions. Thus, watershed algorithms in medical imaging are usually followed by a postprocessing step to merge separate regions that belong to the same structure.

*R*egion growing is a technique for extracting a region of the image that is connected based on some predefined criteria [Haralick 1985]. In its simplest form, region growing requires a seed point that is manually selected by an operator, and extracts all pixels connected to the initial seed with the same intensity value. Region growing can be sensitive to noise, causing extracted regions to have holes or even become disconnected. Conversely, partial volume effects can cause separate regions to become connected.

A survey on thresholding techniques is provided in [Sahoo 1988].

3.1.3   Classification

Classifier methods seek to partition a feature space derived from the image using data with known labels [Schalkoff 1992, Bezdek 1993]. The features used can be related to texture or other properties, or they can simply be intensity values. Classifiers require training data that are manually segmented and then used as references for automatically segmenting new data.

A simple classifier is the *nearest–neighbor* classifier [Duda 1973], where each pixel or voxel is classified in the same class as the training datum with the closest intensity.

The *k–nearest–neighbor* (kNN) classifier is a generalization of this approach, where the pixel is classified according to the majority vote of the closest training data (see [Tapley 1995] for details). The kNN classifier is considered a nonparametric classifier since it makes no underlying assumption about the statistical structure of the data.

Another nonparametric classifier is the *Parzen window* (see [Tapley 1995]), where the classification is made according to the majority vote within a predefined window of the feature space centered at the unlabeled pixel intensity.

A commonly used parametric classifier is the *Bayes classifier* (see [Androutsos 1997] for numerous examples). It assumes that the pixel intensities are independent samples from a mixture of probability distributions, usually Gaussian. Training data is collected by obtaining representative samples from each component of the mixture accordingly. Classification of new data is obtained by assigning each pixel to the class with the highest posterior probability.

A disadvantage of classifiers is that they generally do not perform any spatial modeling. The use of the same training set for a large number of images can lead to biased results which do not take into account anatomical and physiological variability between different subjects.

3.1.4   Clustering

Clustering algorithms essentially perform the same function as classifier methods without the use of training data. Thus, they are termed unsupervised methods. In a sense, clustering methods train themselves using the available data. Three commonly used clustering algorithms are the k-means algorithm [Coleman 1979], the fuzzy k-means algorithm [Dunn 1974, Bezdek 1993], and the expectation-maximization (EM) algorithm [Lei 1992, Liang 1994]. The *k-means* clustering algorithm clusters data by iteratively computing a mean intensity for each class and segmenting the image by classifying each pixel in the class with the closest mean [Jain 1988]. The *fuzzy k–means* algorithm generalizes the k–means algorithm [Bezdek 1993], allowing for soft segmentations based on fuzzy set theory [Zadeh 1965]. The *EM* algorithm applies the same clustering principles with the underlying assumption that the data follows a Gaussian mixture model. It iterates between computing the posterior probabilities and computing maximum likelihood estimates of the means, covariances, and mixing coefficients of the mixture model. Like classifier methods, clustering al-

gorithms do not directly incorporate spatial modeling and can therefore be sensitive to noise and intensity inhomogeneities.

3.1.5   Markov random field models

Markov Random Field (MRF) models spatial interactions between neighboring or nearby pixels [Li 1995]. In medical imaging, they are typically used to take into account the fact that most pixels belong to the same class as their neighboring pixels. MRFs are often incorporated into clustering segmentation algorithms such as the k–means algorithm under a Bayesian prior model [Pappas 1992, Rajapakse 1997, Held 1997, Goldszal 1998]. The segmentation is then obtained by maximizing the posterior probability of the segmentation given the image data using iterative methods such as iterated conditional modes [Besag 1986] or simulated annealing [Geman 1984]. A difficulty associated with MRF models is proper selection of the parameters controlling the strength of spatial interactions [Li 1995]. Computation time is also often an issue.

3.1.6   Artificial neural networks

Artificial neural networks (ANNs) are networks of nodes that are capable of performing elementary computations. The learning process is achieved through the adaptation of weights assigned to the connections between nodes.

An example application to abdominal organs can be found in [Koss 1999]. ANNs can also be used in an unsupervised fashion as a clustering method [Zaim 2005], as well as for deformable models [Vilariño 2003].

Neural networks are appealing for a number of reasons, namely; they seem to "learn" without supervision, they can be created by users with very little mathematical model building experience, and software for building neural networks is now readily available. Neural networks have perhaps a special appeal to the medical community because of their superficial resemblance to the human brain (a structure with which most physicians are comfortable), and seem to promise "prediction" without the difficulties associated with use of mathematics.

ANNs are rich and flexible nonlinear systems that show robust performance in dealing with noisy or incomplete data and have the ability to generalize from the input data. They may be better suited than other modeling systems to predict outcomes when the relationships between the variables are complex, multidimensional, and nonlinear as found in complex biological systems.

The difficulty in developing models using artificial neural networks is that there are no set methods for constructing the architecture of the network. Another limitation of neural network models is that standardized coefficients and odds ratios corresponding to each variable cannot be easily calculated and presented as they are in regression models. Neural network analysis generates weights, which are difficult to interpret as they are affected by the program used to generate them [Baxt 1995]. This lack of interpretability at the level of individual variables (predictors) is one of

the most criticized features in neural network models [Ohno-Machado 1999].

3.1.7   Deformable models

Deformable models [Kass 1988, Staib 1992, Cohen 1993], whether implicitly or explicitly represented (see section 3.1.7.1), are physically motivated, model–based techniques for delineating region boundaries using closed parametric curves or surfaces that deform under the influence of internal and external forces.

To delineate an object boundary in an image, a closed curve or surface must first be placed near the desired boundary and then allowed to undergo an iterative relaxation process.

Internal forces are computed from within the curve or surface to keep it smooth throughout the deformation (section 6.7.1). External forces are usually derived from the image to drive the curve or surface towards the desired feature of interest (section 3.1.7.3).

These models provide a global vision of the structure to be segmented, and they allow for the incorporation of relevant information such as regularisation (section 6.7.1) and shape constraints (section 3.1.7.4), among others.

A general review on deformable models in medical image analysis can be found in [McInerney 1996] and in [Montagnat 2001].

3.1.7.1   Model representation

There are two forms of deformable models.

In the parametric or **explicit** form [Kass 1988, Metaxas 1993, Delingette 1994, Fischler 1973, Terzopoulos 1991, Staib 1992, Cohen 1993, Xu 1998], contours are represented explicitly as parameterized curves or surfaces that evolve in a Lagrangian fashion. This form is not only compact, but is robust to both image noise and boundary gaps as it constrains the extracted boundaries to be smooth. However, it can restrict the degree of topological adaptability of the model, especially if the deformation involves splitting or merging of parts.

Geometric or **implicit** deformable models [Osher 1988, Osher 2003, Sethian 2001, Mumford 1989, Caselles 1995a, Caselles 1995a, Chan 2001, Suri 2002] are implemented in the level set based curve evolution framework. Contours are embeded implicitly as level sets of higher–dimensional level set functions, and evolve according to an Eulerian formulation. They are designed to handle topological changes naturally but, unlike the parametric form, they are not robust to boundary gaps and require a greater computation time (mostly in 3 dimensions and higher).

3.1.7.2   Internal or regularisation forces

Internal forces play a key role for regularisation purposes. They render the energy functional locally convex, thus allowing the model to deform while respecting certain regularity criteria.

Several internal forces have been proposed in the literature [Kass 1988, Cohen 1991]. In general, they involve contour curvature or differential characteristics of superior order.

3.1.7.3   Data–driven forces

In traditional deformable models, image forces come primarily from edge (i.e., significant image intensity gradient) information. Such reliance on edge information, however, makes the models sensitive to noise and highly dependent on the initial estimate. There have been significant efforts to integrate region information into deformable models. In [Ron 1994], local region analysis strategies are introduced for Active Contour Models. But the optimization of the integrated energy function is mostly heuristic. In [Zhu 1995], a generalized energy function that integrates region growing and boundary-based deformations was proposed. They proposed the idea of a region competition to control the model deformation. In this formulation, however, the parameters of the regional intensity statistics can not be updated simultaneously with the boundary shape parameters so that the energy function has to be minimized in an iterative way. A method using explicit parametric deformable models that take into account model interior texture information is proposed in [Huang 2004]. Chan and Vese [Chan 2001] present a level–set method based on the Mumford–Shah model [Mumford 1989], whose main idea is also to consider the information inside the regions, and not only at their boundaries.

3.1.7.4   Introduction of shape models

The image data may not be sufficient to extract the structure of interest; therefore, prior knowledge has to be introduced. When the structure's shape remains similar from one image to another, a shape model can be built from training samples. Several types of shape models have been proposed [Cootes 1995a, Leventon 2000, Freedman 2005b, Tsai 2004, Cremers 2004, Rousson 2004, Dam 2004]. Such models can be used to constrain the extraction of similar structures in other images. A straightforward approach is to estimate the "allowable" model shape that best fits the structure in the observed image [Tsai 2004, Dam 2004, Rousson 2005b]. This assumes the shape model to be generic enough to describe the new structure. A noise model may also be added to the shape prior [Lecellier 2006].

3.1.8   Atlas–guided registration approaches

The atlas is generated by compiling information on the anatomy that requires segmenting. This atlas is then used as a reference frame for segmenting new images. The standard atlas-guided approach treats segmentation as a registration problem [Maintz 1998]. It first finds a one-to-one transformation that maps a pre–segmented atlas image to the target image that requires segmentation.

Because the atlas is already segmented, all structural information is transferred to the target image. An advantage of atlas-guided approaches is that labels are

transferred as well as the segmentation. Even with non-linear registration methods however, accurate segmentations of complex structures is difficult due to anatomical variability.

An atlas–guided approach to the segmentation of abdominal structures (liver, kidneys and spinal cord) can be found in [Park 2003]. A feasibility study for an atlas–guided segmentation of bladder, prostate, rectum and femoral heads can be found in [Bondiau 2004].

3.2   Segmentation of target and organs at risk for prostate radiotherapy

Accurate contouring of the Gross Tumor Volume (GTV) (defined in section 2.4.1.5) and critical organs is a fundamental prerequisite for successful treatment of cancer by radiotherapy. This task is specifically more challenging in the case of the prostate cancer. The main reasons are first, there is almost no intensity gradient at the bladder-prostate interface. Second, the bladder and rectum fillings change from one treatment session to another and that causes variation in both shape and appearance. Third, the shape of the prostate changes mainly due to boundary conditions, which are set (due to pressure) from bladder and rectum fillings. In addition, the presence of structures such as the seminal vesicles and the bladder neck near the base, urethra, pelvic musculature, and the posterior part of the pubic arch near the apex, makes the automatic boundary delineation difficult.

Several approaches to automate this process have been proposed. In this section, we give an overview of recent semi–automatic and automatic techniques that have been investigated for the segmentation of bladder, prostate and rectum volumes.

3.2.1   Bladder Segmentation

The bladder is a soft–tissue structure which, in different pelvic CT scans, may show very different characteristics. Variability includes size, shape, intensity and contrast among different patients, and even within the same patient at different times of the day.

Size and Shape Variabilities are mainly due to bladder fillings, and the deformation caused by surrounding organs. CT scans of the same patient throughout treatment planning sessions (or even during the same day) may show the bladder with completely different characteristics. See figure 3.3 for some examples.

Intensity Variability If the patient has been given a contrast agent before the scan, the bladder can appear as an homogenous, highly contrasted structure in which the contrast agent is fully visible. However, if the contrast agent has not fully arrived in the bladder, the latter may appear as a non–homogenous structure. In this case, and since the contrast agent is more dense than urine, the gravity pulls it towards the ground, thus defining a highly contrasted lower zone where the contrast agent has settled, a non–contrasted upper zone, and an intermediate
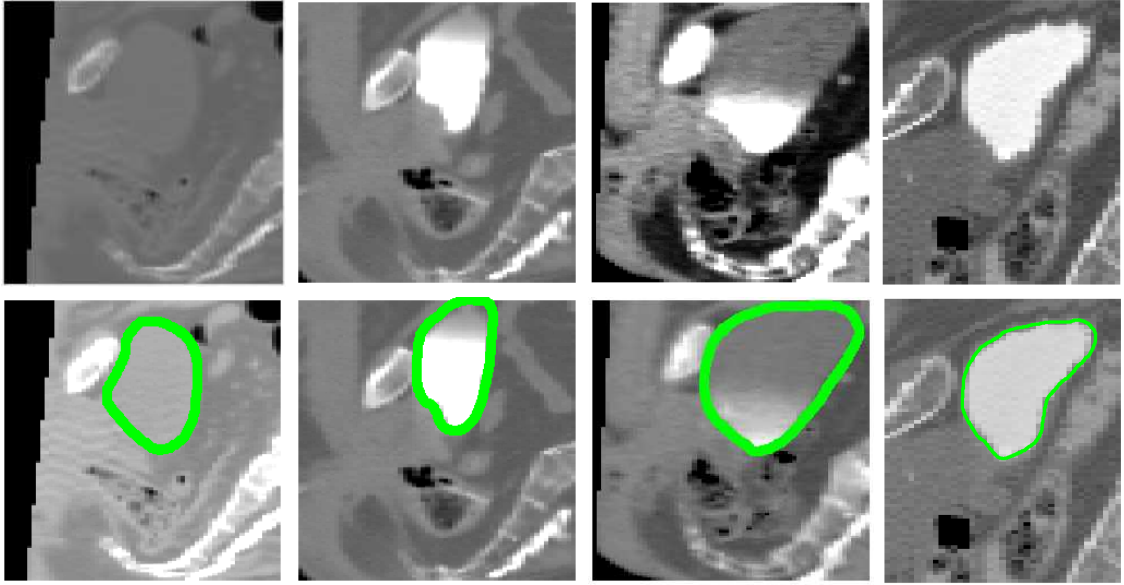
Figure 3.2: Different intensity characteristics make the bladder segmentation task challenging. From left to right, homogenous non–contrasted bladder, two non–homogenous bladders (up to different levels) and an homogenous contrasted bladder (sagittal views). The second row shows the bladders outlined in the same images.

"intensity gradient" region where between the two. If no contrast agent has been administered whatsoever, the bladder appears as an homogenous, non–contrasted structure. All of the above cases are illustrated in figure 3.2.

We present an overview of different semi–automatic and fully automatic bladder segmentation methods that have been proposed in the literature.

3.2.1.1 Non–rigid registration approaches

These methods have been tested for CT bladder segmentation (see [Unal 2005] for a combined segmentation and registration approach). However, the considerable inter and intra–patient variation in soft tissue (slimmer and less slim patients, filling of the bladder at the moment of the CT scan, presence of contrast agent) may cause nearby structures to undergo "unnatural" deformations necessary for the atlas to adapt to each patient's specific bladder shape.

3.2.1.2 Mathematical morphology approaches

Mathematical morphology approaches are useful for bladder segmentation, for several reasons: the topology of the shape is known, the methods are easier to automate, and they can be quickly tuned and computed. Variations of these approaches have been tested in [Camapum 2004] and [Mazonakis 2001] (region growing based algorithms) and in [Bueno 2001] (watershed based algorithm). However, they are quite
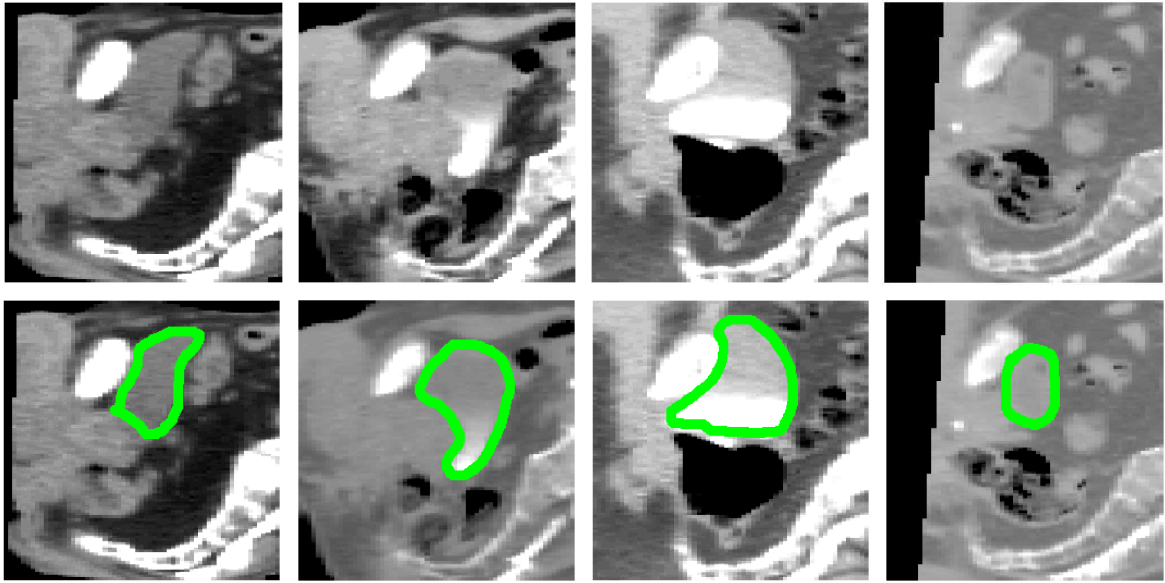
Figure 3.3: Different bladder shapes and sizes (sagittal views). The second row shows the bladders outlined in the same images.

dependent on the quality of the image, and intensity inhomogeneities within the structures are not taken into account.

3.2.1.3   Shape deformation approaches

Shape deformation approaches include geometric [Gibou 2005, Broadhurst 2005, Stough 2007] and parametric [Bueno 2004] deformable models. They are quite flexible, since shape priors may be incorporated [Gibou 2005, Fenster 2001, Rousson 2005a, Freedman 2004, Freedman 2005a, Broadhurst 2005], an atlas can serve as initialization [Ripoche 2004], they can be made to follow fuzzy criteria [Bueno 2004], and they allow for more than one structure to evolve simultaneously (e.g. the prostate and bladder, as in [Rousson 2005a]). However, they often require either training [Freedman 2004], user interaction [Gibou 2005, Freedman 2005a], or assume homogenous intensity structures [Stough 2007].

3.2.2   Prostate–Bladder Segmentation

The main factors at the source of the variability of the prostate are patient movement and the influence of the neighboring (and highly variable) bladder and rectum. The influence of the bladder's fillings on the shape of the prostate while it interacts with an endorectal echographic probe has been addressed in [Marchal 2005]. The lack of intensity gradient at the bladder–prostate interface in the case of non–contrasted bladders accounts for the fact that both organs are often segmented simultaneously, in order to find a viable common border. A non–homogenous intensity bladder will
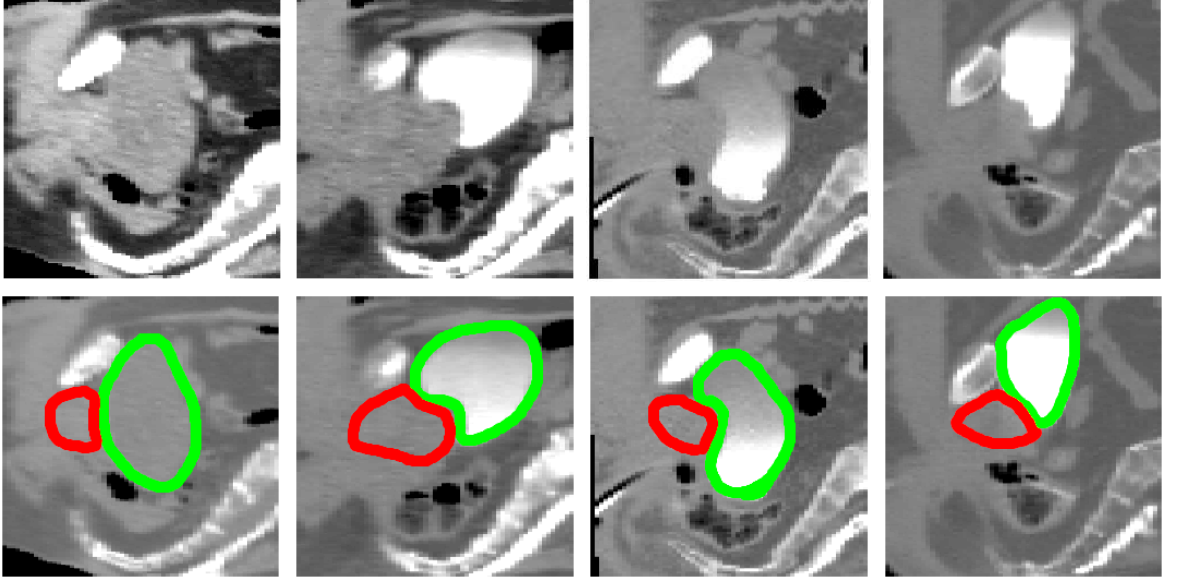
Figure 3.4: Different prostate shapes and border conditions for the bladder and prostate. Both structures are outlined in green (bladder) and red (prostate) in the second row of images.

make the prostate–bladder interface defined in some regions and fuzzy in others. If a flexible approach is sought, this frontier variability should be taken into account.

Examples of the complexity of the bladder–prostate segmentation method are illustrated in figure 3.4. The high variability of the bladder and rectum shapes which, in turn, change the boundaries of the prostate, also add to the difficulty of the segmentation process (see figure 3.5).

Several automated and semi–automated approaches for prostate and coupled bladder–prostate segmentation have been proposed. An overview of these methods is presented in the following section.
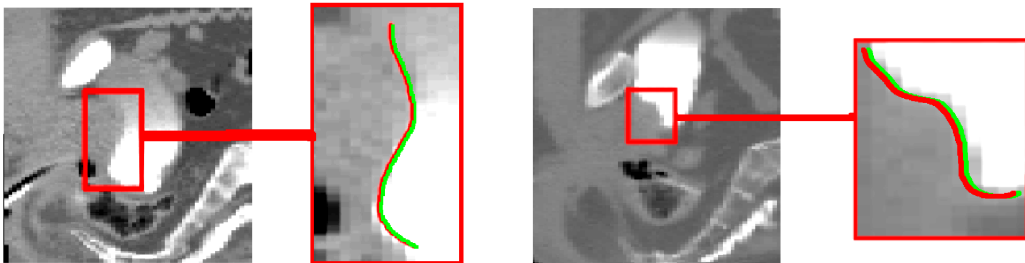
Figure 3.5: Different bladder intensities condition its shared border with the prostate, making their segmentation process challenging.

3.2.3   Un–coupled Bladder and Prostate Segmentation

3.2.3.1   Registration Approaches

These methods have been tested for CT bladder[Unal 2005] and prostate[Davis 2005, Malsch 2006] segmentation.

In particular, [Davis 2005] presents an automatic approach to quantify prostate motion based on deformable image registration, as well as on a bowel gas deflation algorithm to minimize correspondence errors.

However, heavy variations in soft tissue (shape, size, intensity) are difficult to capture by these approaches, but they remain quite useful for initialization purposes.

3.2.3.2   Mathematical Morphology Approaches

Variations of these approaches have been tested in [Camapum 2004, Mazonakis 2001]. They are easy to automate and can be quickly tuned and computed, but they are strongly dependent on the quality of the image.

3.2.3.3   Shape Deformation Approaches

Deformable models are quite flexible, since they can include shape priors[Rousson 2005a, Freedman 2005a, Broadhurst 2005], atlas initialization[Ripoche 2004], fuzzy criteria[Bueno 2004] and multiple structure deformation[Rousson 2005a]. *Explicit models* have been used for both prostate[Freedman 2004, Dam 2004, Pekar 2004] and bladder[Bueno 2004] segmentation. *Implicit models* have also been used to this end (see [Broadhurst 2005] for prostate and [Tsai 2003] for bladder segmentation).

3.2.3.4   Other Approaches

Other approaches include neural networks[Lee 2004], radial searching[Xu 2003], polar transform based methods[Zwiggelaar 2003] and genetic algorithms[Cosío 2005, Ghosh 2006], among others.

3.2.4   Multiple Structure Segmentation

When multiple neighboring structures are segmented simultaneously, a purely independent approach for each of them may lead to unnatural results. For instance, the resulting segmentations may show overlaps and intersections that are virtually impossible with real life organs. Several authors have approached this issue and proposed different solutions.

3.2.4.1   Overlap penalization

This is an *a–posteriori* solution, in which overlaps must occur in order to be penalized. Variations have been proposed for both explicit[Zimmer 2005] and implicit[Rousson 2005a] deformable models. In both cases, overlaps are punished in terms of energy minimization. The first approach couples multiple active contours in 2D video sequences

through a unique energy function. The second presents a Bayesian inference framework where a shape prior can be applied on any of the structures. However, neither approach have been applied in contexts in which intensity inhomogeneities must be handled.

3.2.4.2 Statistical shape and appearance model approaches

These methods attemps an *a–priori* solution to overlaps. Prior information has a strong influence on the segmentation processes of the individual structures, in an effort to avoid overlaps instead of letting them happen and then resolving them.

Approaches in this category have been used in [Freedman 2004, Paragios 2002, Pizer 2005, Vese 2002, Yezzi 2002], among others. In [Pizer 2005], a segmentation method using both an intensity prior based on intensity profiles at each point and a geometric typicality (shape prior) is proposed. In [Paragios 2002, Vese 2002, Yezzi 2002], a perfect partition of the image into classes of similar intensities or textures is achieved. However, these techniques treat objects sharing similar image characteristics as a single item; thus, topological constraints between them cannot be enforced in the absence of a clear delimitation of the structures (as is the case with several non–contrasted bladders and prostates in our database).

3.2.5 Rectum Segmentation and Integration

Several approaches for rectum segmentation, although not as many as for that of the bladder or prostate, can be found in the literature.

The complexity of the rectum segmentation task lies mainly in the varied and temporary nature of its fillings and on the preparation of the patient prior to image acquisition. Indeed, the shape and appearance of the rectum are influenced by several factors:

- **Contrast Agent** A contrast substance may have been given to the patient, making the rectum walls' intensity lighter when compared with its surroundings.

- **Air Insufflation** Some patient's rectums are insufflated with air in order to expand it and facilitate the visibility.

- **Fillings** An empty rectum's shape is quite different from that of a full one. The unpredictability of the fillings' nature are also a factor (solid, gas).

- **Probe** A probe is sometimes used during the patient's examinations, which is fully visible in the resulting images.

These factors render a flexible approach to the segmentation of the rectum even more challenging. Example images are shown in figure 3.6.

We present, in the following subsections, several approaches that have been proposed and applied in the frame of rectum segmentation.
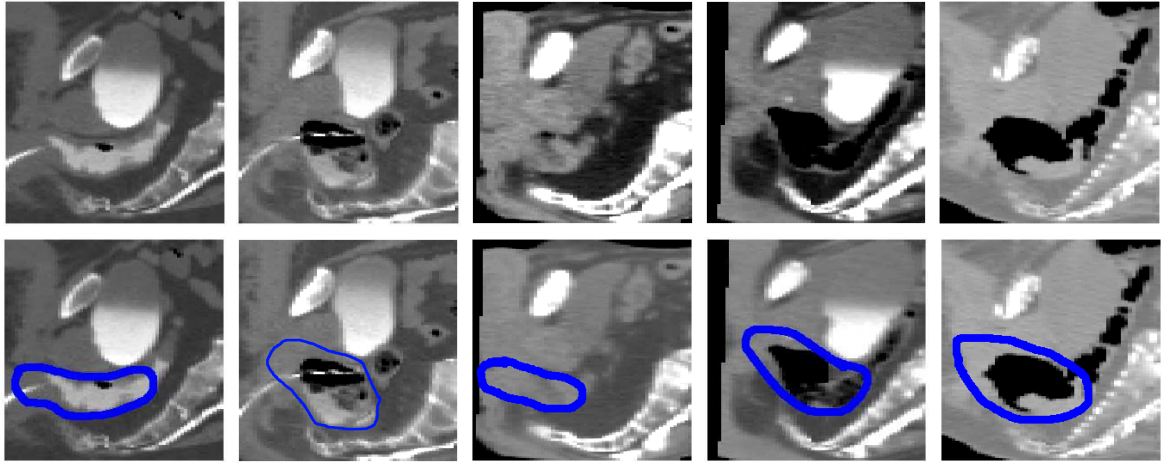
Figure 3.6: Different rectum shapes and appearances. From left to right, presence of contrast agent and probe, no contrast agent but probe, empty rectum, different fillings, and air insufflation. The rectums have been delineated in blue in the second row of images.

3.2.5.1 Mathematical Morphology Approaches

O. Silva *et al.*[Silva 2004] propose a 2D region growing method with multiple seeds to construct a mosaic image, followed by a watershed transform.

Mazonakis et al. [Mazonakis 2001] also assess a region growing approach for the segmentation of the (homogenous intensity) rectum, bladder and prostate.

[Bueno 2001] test a morphological segmentation technique for the segmentation of 2D CT scans of the lower abdomen.

These methods are limited to homogenous structures, and tend to perform poorly when an organ's limits with respect to surrounding structures are not clearly defined.

3.2.5.2 Implicit Model Deformation Approaches

[Gibou 2005] propose an intensity–based speed function for the evolution of an implicit deformable model. Using a Mumford–Shah functional, they seek to separate the image into regions with respect to their respective average intensity value. In the presence of organ regions where adjacent structures have similar average intensity values, it is left to the user to place a wireframe in the region where the boundary is not clearly characterized by jumps in the image intensity. They apply their approach, among others, to the segmentation of the bladder and rectum (independent of each other).

This semi–automatic approach does not seem appropriate for segmentation of highly intensity–variable structures (such as the rectum) whose boundaries with many surrounding structures, and thus in large regions, are not clearly defined.

Tsai *et al.*[Tsai 2004] present an extension to the shape–based deformable active contour model, in order to allow simultaneous multiple structure segmentations.

Multiple signed distance functions are employed as the implicit representations of the multiple shape classes within the image. The coupling among shapes is achieved by deriving a parametric model by applying principal component analysis to the collection of these multiple signed distance functions. Their method is applied to the joint segmentation of the prostate, rectum and the internal obturator muscles in MRI images.

Although the resulting algorithm is able to utilize the co–dependencies among the different shapes to aid in the segmentation process, the inter–dependence in the shape of lower abdomen structures such as rectum and bladder is not necessarily clear. The fact that the bladder is filled in one patient's case does not necessarily mean that the rectum is full as well, and vice–versa. Since their variability is mainly due to their respective fillings, and since the latter are independent of one another, the study of their joint shapes would yield an inaccurate relationship that would bias the segmentation process.

3.2.5.3 Explicit Model Deformation Approaches

The authors in [Freedman 2004] present a segmentation algorithm, applied to the prostate and the joint segmentation of prostate and rectum, that uses learned models for both the shape and appearance of objects to achieve segmentation. Based on matching probability distributions of photometric variables and learned shape and appearance models, the result is the segmentation that best aligns the apriori information. In [Freedman 2005b] a similar approach is used to segment bladder, prostate and rectum. The method relies on an intensity model of the interior of the structures, thus making assumptions about their fillings. However, in the case of the rectum, the *highly* variable nature of its fillings could be hardly captured by an appearance model, making their approach inaccurate in a database like ours. The images are not previously put in a common frame of reference (registration), and the initial position of the model is fixed, which provides little flexibility. In the case where neighboring structures have very similar intensities, an indistinguishable boundary and similar topology, there is a risk of mistakenly segmenting one with the model destined to the other (this may occur, for instance, with the bladder and prostate). A similar risk exists in the case where rectum and prostate share intensity characteristics (for empty rectums, for example).

[Xiao 2001] propose an extended active contour framework for the segmentation of the rectal wall multilayer in ultrasound images. They detect the rectal layers from inner to outer using deformable models. The currently segmented layer serves as initialization for the segmentation of the next, by means of a cost function with low local costs on features that exhibit strong edge features, as well as a local cost function that compensates broken image segments. In our case, given the high variability in the rectum's fillings, an intensity–guided segmentation method based on the interior of the structure would be inaccurate.

3.2.5.4   Related Approaches

Since the rectum is, essentially, a tubular organ, its segmentation can be compared to that of other tube–like structures. Numerous approaches for the segmentation of structures with similar characteristics can be found in the literature, including blood vessels extraction approaches, centerline computation and skeletonization algorithms, and tubular constraint enforcement.

Vessel extraction   A comprehensive survey and review of **vessel extraction** approaches can be found in [Kirbas 2004]. However, there are several differences with respect to the rectum:

- The rectum is unique, and its position somewhat known, as opposed to the several vessels that must first be detected to be segmented.

- Blood vessels are tubular structures with relatively small and constant diameter, which cannot be said of the rectum.

- Vessels have homogenous intensity, as opposed to the rectum.

- Vessels show complex tree or network structures with tubular branches, similar to those present in neural networks, lymphatic, tracheas etc. These are challenges not present in the case of the rectum.

The above differences make the vessel extraction techniques interesting, yet not suitable for the rectum delineation.

Centerline computation   The tubular structure of the rectum can be exploited for its segmentation by computing, for instance, a centerline. Several approaches to *automatic centerline extraction* have been proposed. We briefly review some representative approaches.

- A first class of methods attempts to find centerlines of tubular structures as they are manifest directly in intensity (MR or CT) images. These methods do not assume that the surfaces of such structures have first been extracted (see, for example, [Santamaría-Pang 2007]). Aylward and Bullit [Aylward 2002], Wink et al. [Wink 2004] and Frangi et al [Frangi 1998] present centerline tracking approaches in which tubular structures are identified using properties of the Hessian matrix. However, in order to be detected this way, the tubular structures must be sufficiently "thin", which is not the case of the rectum.

- A second class of methods aims to find centerlines of tubular structures which have first been segmented from 3D MR or CT intensity images. Some representative approaches include those by Bitter et al. [Bitter 2001], Paik et al. [Paik 1998], [Flasque 2000] and Ge et al. [Ge 1999]. These methods are often used in the frame of CT colonography since, in these cases, the colon

is assumed to show a contrast agent and to have been air insufflated, which greatly facilitates the segmentation task.

In the case of the rectum, its variability from a constant diameter tube structure as well as its intensity variability renders the first class of method inadequate. The second class assumes that the structure has already been segmented, which is not our case.

Some deformable model approaches include the "skeleton" in the model itself, as opposed to extracting it from the binary segmentation of the structure. This is the case of *M–Reps*, which are representations of figures by medial atoms [Pizer 2003].

Tubular constraints   Explicit deformable model approaches may incorporate *tubular constraints*. Cylindrical or line–like shapes parametrized by centerlines have been proposed in ([Frangi 1998, Krissian 2000, de Bruijne 2003, Wink 2004, Yim 2001, Fridman 2004, Volkau 2005, Montagnat 1999b]). These models often require user interaction, and the strong tubular constraints prevent them from representing shapes that differ more than slightly from a fixed diameter tube. A symmetry–seeking approach that depends on a user–placed centerline has been proposed in [Terzopoulos 1987].

Other model approaches   Implicit deformable models have become very popular due to their ability to handle changes of topology and adapt to the shape of complex structures. Geometric models may be based on gradient information (Geodesic Active Contours, [Caselles 1995b]) or region–based intensity information [Paragios 2000, Chan 2001, Rousson 2003, Pichon 2004]. In the first case, a variable interior with unpredictable gradients, such as that of the rectum, would hinder its evolution. In the second case, the estimation of the region statistics is based on the assumption that image intensity is a discriminant tissue descriptor, again not the case in the rectums of our database.

Geometric deformable models have been used for the segmentation of tubular structures by specific adaptations that include smart initializations of the model [Deschamps 2001, Bemmel 2003], modifications in the energy functional[Hernandez 2004] or hybrid approaches[Chen 2004].

3.3   Overview of our Methodology

Our goal is the fully automatic delineation of the prostate and its organs–at–risk in the context of radiotherapy planning. In the process of selecting a methodology to be the building block of our method, we had to take into account several points:

1. The (highly) **heterogenous nature of our database of images**. The growing number of CT scans in the database we use for training and testing has been acquired in different imaging centers and under different protocols (including Hôpital de l'Archet in Nice, and images from different centers provided

by DOSIsoft) strongly limit the assumptions that can be made about shape
and appearance. Homogenous (contrasted and non–contrasted) as well as
non–homogenous bladders, prostates with fuzzy and less fuzzy borders, and
rectums showing contras agent or not, filled, empty, or with a probe, are all
combined in our database. Our method must be able to automatically adapt
to and segment all these kinds of structures. Throughout the course of this
thesis, the size of our CT database has grown from 5 to 20 CT images. The
preparation protocols for the patients vary to a considerable extent (contrast
agent administered to the patient or not, presence of a probe, rectum air in-
sufflation and mixed fillings). The images themselves can be divided into 3
groups: the first consists of CT scans of around 80 axial slices of 256x256 vox-
els each. The distance between voxel centers in successive slices is of 3 mm,
and the voxel sizes in the sagittal and coronal planes are of 1.87 mm each. The
second group includes images of about 125 axial slices of 512x512 voxels each.
Their voxel size is of 0.97mm x 0.97 mm x 2 mm (sagittal, coronal and axial
planes, respectively). The third group comprises images of size 256x256x40
(sagittal, coronal and axial, respectively), with voxel sizes of 1.67 mm x 1.67
mm x 4 mm.

2. The **(in–)homogeneities in bladder intensity** make its segmentation more
challenging. However, we would like to be able to exploit the information con-
cerning the localization of these zones. That includes the fact that homogenous
bladders can be either contrasted or non–contrasted, and that, in the case of
non–homogenous structures, the contrast agent is pulled by gravity and thus,
the contrasted zone would be located *under* (i.e., closer to the ground) the
non–contrasted zone. An approach that would allow us to define "zones" that
could serve to segment the different regions in the bladder would be interesting.

3. The often **fuzzy prostate borders** would need more information than just
image intensity in order to be correctly segmented. The introduction of other
information for the prostate, such as the results of a shape study, as well as
information on the type of bladder in the image and their common interface
would be desirable in those cases. An approach that could allow a "collabo-
rative" approach for the joint segmentation of both structures might also be
desirable.

4. The **different fillings of the rectum** (air insufflation, clean, not clean,
probe, contrast agent or not) according to various acquisition protocols deter-
mine its characteristics in each image. We would like a method to be flexible
enough in terms of intensity to accommodate the different appearances, while
preserving shape coherency and avoiding an invasion of surrounding organs
and their segmentations.

Any assumptions concerning shape, size or intensity that we made concerning
bladder, prostate or rectum would limit the amplitude of applicability of our method.

The key factor that has therefore guided and inspired the approaches presented throughout this manuscript has been, therefore, **adaptability** both to shape and to intensity variability.

In general, the approaches that we have found in the literature impose quite strong shape and/or appearance constraints on the structures involved. The methods are therefore restricted to homogenous structures, or structures with characterizable inhomogeneities, which are not always the case in our database of images.

We are thus motivated to propose a fully automatic framework for coupled bladder–prostate segmentation. The method should adjust itself to different kinds of bladder (homogenous, different levels of inhomogeneities). The characteristics of the interface between bladder and prostate in the image may be taken into account in the application of a non–overlapping constraint on the deformable models. Since the prostate shows a much better statistical coherency in shape among patients than the bladder ([Rousson 2005a]), a prostate shape prior could prove to be useful. For the rectum, the proposed method must be flexible enough to accommodate large intensity variations that are unpredictable in advance, but should maintain a certain coherency in terms of shape, not too distant from a certain reference which might be, for example, an average rectum shape.

To comply with all these requirements, we have chosen our method to be based on explicit deformable models and, more specifically, **simplex meshes**.

Bladder Segmentation

Contents

4.1 Challenges in Bladder Segmentation

The bladder is a hollow organ located in the lower abdomen that holds urine (see figure 4.1). It is held in place by ligaments that are attached to other organs and the pelvic bones. The bladder's walls relax and expand to store urine, and contract and flatten to empty urine through the urethra.

    The bladders in our CT image database show quite different shape, size and intensity characteristics, as detailed in the next section.
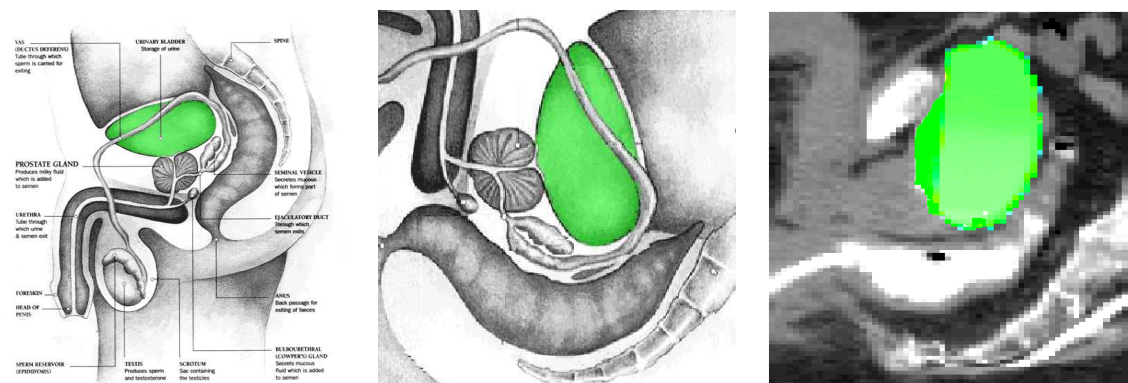
Figure 4.1: The bladder (green) on a standing patient (left), and how we see it when the patient is lying down (center) and on an actual CT scan (right).

4.1.1 Intensity variability

Sometimes an intravenous contrast is used to highlight and to enhance certain organs such as the bladder. The contrast agent (usually an iodine compound) is injected into the bloodstream, and it circulates throughout the body. The kidneys and liver quickly eliminate the contrast, which is then temporarily stored in the bladder. The CT's x–ray beam is weakened as it passes through the blood vessels and the organs that have "taken up" the contrast. The bladder is enhanced by this process and shows up as an hypersignal area on the CT images, with an intensity similar to that of the bones (between +200 and +1000 H.U.).

1. If **no contrast agent** has been administered to the patient, the bladder is seen as an homogenous structure with an intensity range similar to other soft tissues (around +40 H.U.). An example is shown at the center of figure 4.2.

2. If a contrast agent has been administered to the patient, two situations may arise:

   - If the **contrast agent is fully visible** in the bladder image, the result is an homogenous, contrasted structure, such as the one at the left hand side of figure 4.2.
   - However, if the time between contrast administration an CT scan acquisition is not sufficiently long, the **contrast agent may enhance only a part of the bladder**. This is due to the patient's position (lying down) and the fact that the contrast agent, being a dense product, is pulled by gravity and therefore concentrates in the portion of the bladder that is closer to the ground. In this case, the bladder can be seen as a non–homogenous structure, showing both a contrasted and a non–contrasted portion, as well as an intermediate zone between the two, where an intensity gradient can be appreciated. An example of this case is shown on the right handside of figure 4.2.
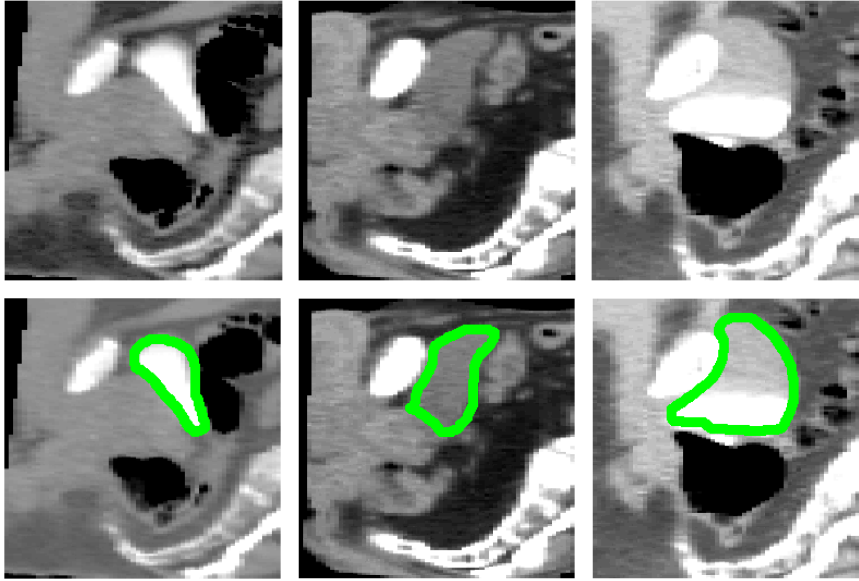
Figure 4.2: Examples of shape and size variability for the bladder (sagittal views). From left to right, homogenous contrasted bladder, homogenous non–contrasted bladder, and heterogenous bladder showing a lower contrasted zone and an upper non–contrasted zone. The second row shows the bladders outlined in green.

This is summarized in figure 4.3.

4.1.2 Shape and Size Variability

Since the bladder is a soft tissue structure, patient movement, position and its surrounding structures may modify its shape. The variable nature of its fillings further influence the shape and size of the bladder. Although homeomorphic to a sphere, significant changes in size and shape can be noticed in figure 4.2

The concept that summarizes the challenges involved in the automatic segmentation of the bladder is, therefore, that of **adaptability** (to different shapes, sizes and intensities), without the need for human interaction. Different bladders present
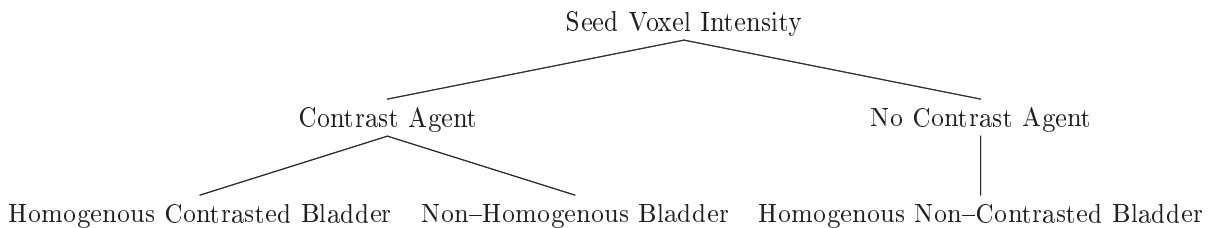
Figure 4.3: The presence or absence of a contrast agent greatly influences the bladder's appearance.

in our database are illustrated in figure 4.4.

The eventual intervention of an expert may be interesting, since perhaps medical experts may wish to manually improve the final results. Our method contemplates that possibility, and allows for human intervention at the end of the automatic segmentation process.

4.2 Contribution and Outline

The bladders that appear in the CT images used in the approaches cited in section 3.2.1 are homogenous and mainly non–contrasted. The interaction of an expert is often required either for initialization, or to choose patient–specific parameters. Strong assumptions are often made concerning its shape and/or intensity.

The novelty of our approach resides in the automatic initialization method (seed voxel detection) and the ability to adapt to different bladder images (homogenous intensity with high contrast, homogenous intensity with low contrast, or non–homogenous intensity with different contrast zones). We take full advantage of the capacity of simplex meshes to be divided into zones. A new histogram–based external force is developed to guide the deformation of these zones, so that they adjust to the underlying bladder intensity zones in the case of non–homogenous structures.

Our approach is three–fold. It incorporates *non–rigid registration* based on surrounding bone structures to provide a reliable spatial initialization, *mathematical morphology* based operations to compute a good initialization of the underlying structure and *deformable models* to refine and smooth the segmentation while enforcing model constraints and forbidding segmentation "leakage" to neighboring soft tissue structures.

The overall framework for the segmentation of the bladder that we propose is as follows:

1. First, preliminary treatments are performed (section 4.3) in order to put the images in a common frame of reference. This is achieved through registration using a special polyaffine method. Next, the region in the image on which computations are perfomed is reduced in order to save processing time.

2. As described in section 4.3.3, the bladder is then located and classified as homogenous or non–homogenous, contrasted or non–contrasted (Figure 4.3). The segmentation begins by computing an approximation of the structure using a method that has been specifically designed to this end.

3. A simplex mesh is deformed to fit the approximation of the bladder. This step is described in section 4.5.

4. The mesh segmentation is eventually refined and smoothed using the bladder in the CT image itself as a guide (section 4.6).
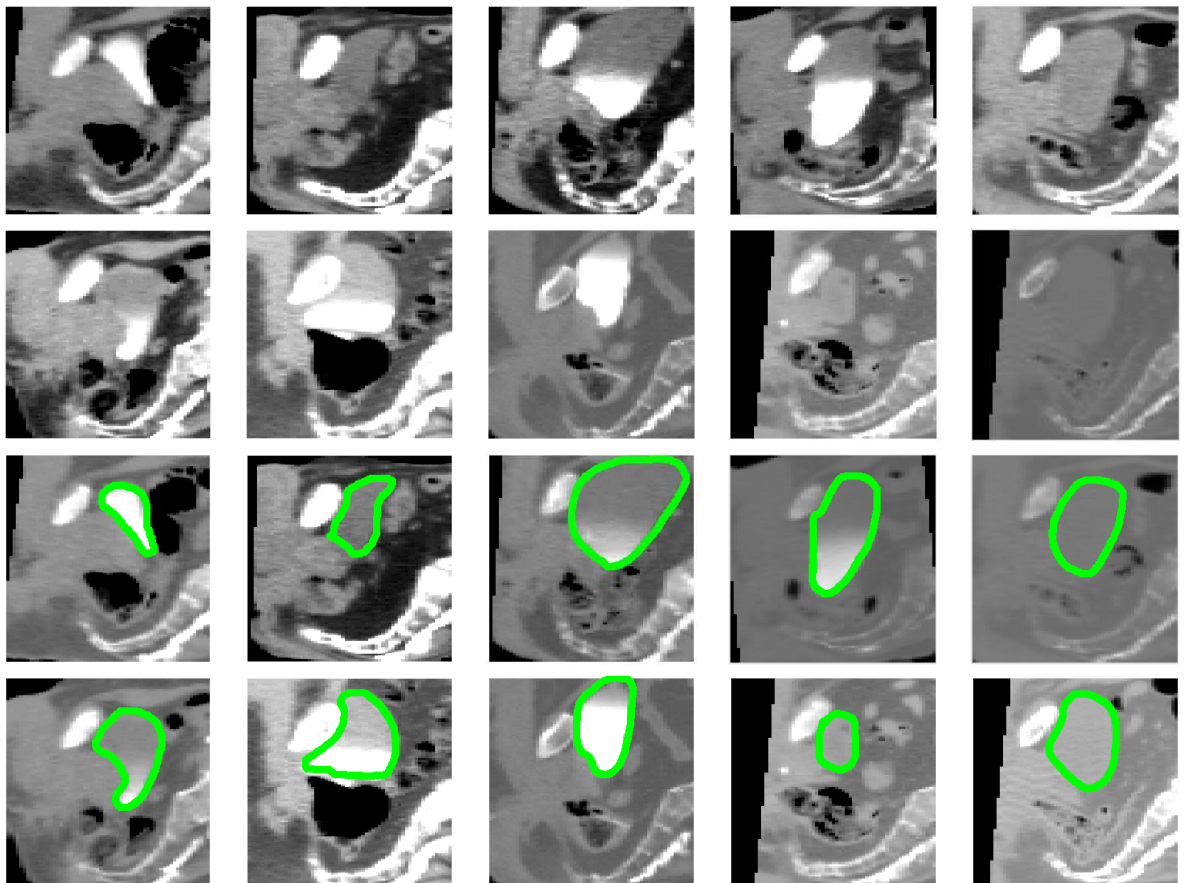
Figure 4.4: Different types of bladders make the segmentation task challenging (sagittal views). First two rows: original images. Third and fourth row: the same images, with the bladder outlined in green.
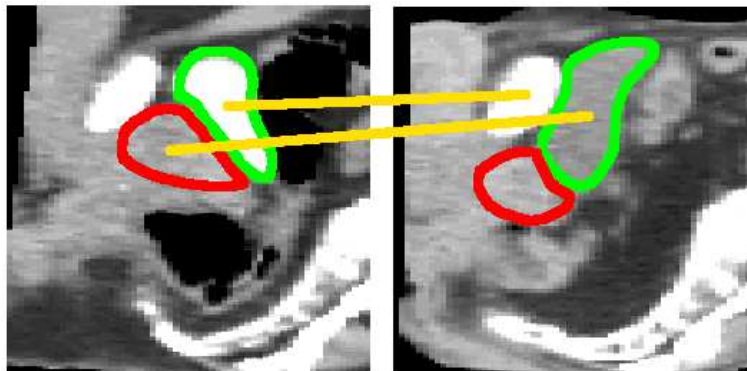
Figure 4.5: Examples of wrong pairings (orange lines) that may arise if no zones are defined for registration. The bladder's intensity variability from one image to another renders the resulting transformation unreliable.

4.3   Preliminary processing

4.3.1   Registration

For our application, the goal is to place all of the patients' data in a common space while deforming the soft tissues as little as possible. In fact, taking soft tissues as landmarks for the registration process can greatly mislead the process. For instance, in the case of non–homogenous bladders, the contrasted portion has similar intensity to that shown by the bones (and, therefore, by the neighboring femoral heads), while the non–contrasted part is similar in appearance to other nearby soft tissues. In the case of an homogenous bladder image being registered to a non–homogenous bladder image, for instance, it is likely that wrong pairings would result in unnatural distortions of the structures (see figure 4.5).

However, the images do contain more "stable" structures, i.e., structures that are not easily deformed and whose intensity is quite predictable from one image to another. These structures are the pelvic bones. If we are able to register the images based on these structures (by defining zones, for example) and then interpolating the resulting transformation to yield a dense deformation field, the resulting registration would be much more reliable.

We have used the locally affine registration framework proposed in [Commowick 2006], which allows us to register local areas in the images using affine transformations having few degrees of freedom. The novel polyaffine framework and Log–Euclidean regularization ensure a smooth, coherent and invertible transformation all over the image. Registration is achieved quite efficiently in 3D.

The fact that this algorithm performs the registration based on selected zones, as well as the results shown in the next section (and published in [Commowick 2006]), prove that it is well adapted to this type of application.
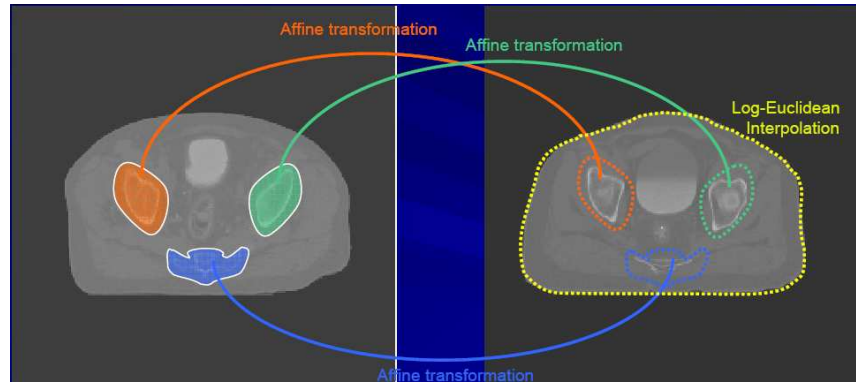
Figure 4.6: Locally afine transformations are computed for each zone, and they are then interpolated in the Log–Euclidean space to generate a dense, yet invertible, transformation.

4.3.1.1 Locally Affine Registration

Commowick *et al.* present an efficient and general framework for locally affine registration. The transformations are parametrized by local affine components, associated to predefined areas. The use of a Log–Euclidean polyaffine framework and a Log–Euclidean regularization among affine components guarantee an invertible and anatomically consistent transformation [Arsigny 2006]. Their method to combine local affine transformations to obtain a global transformation and their regularization scheme is detailed in appendix A. The principle of locally affine registration is illustrated in figure 4.6

Locally Affine Registration Applied to Bone Registration in Lower Abdomen Area We tested the performance of the locally affine registration algorithm in the frame of high–precision radiotherapy planning (see [Commowick 2006]). The aim was to develop an automatic method for soft–tissue localization in the lower abdomen area, based on CT images.

The position of the soft tissues was estimated with respect to a set of landmarks established in more stable surrounding structures showing a better contrast in CT images. All the patients' images were registered to a common space, and the quality of the results was measured by comparing the position of landmark points in the pelvic bones in the registered images. For our feasibility study, the landmarks have been the centers of mass of the femoral heads. Regions around these points (in our case, the femoral heads themselves) are used as affine component localizations in the registration algorithm.

All the patients' images are registered with respect to a reference image. The process consists of two stages: a global affine registration is performed using a block–matching algorithm (see [Commowick 2006]), and then the locally affine algorithm is applied.

Figure 4.7: Registration result on the pelvis. The femoral heads of the reference image (left) have been outlined in red, and this outline has been superimposed over the floating image after a global affine registration (center), and the floating image after using locally affine registration (right). The femoral heads contours in the reference image match the (locally affine) registered femoral heads best.

For a qualitative evaluation, the obtained results are compared with a plain affine transformation in figure 4.7. Besides the observable improvements with respect to the affine transformation, the locally–affine registered images remain consistent from an anatomical point of view, even outside the regions defined for the registration process.

For a quantitative assessment, a comparison has been carried out with the results of a dense, non–rigid registration algorithm [Cachier 2003]. Table 4.1 shows the norm of the Euclidean distance between the landmarks in the registered images and the corresponding landmarks in reference image.

Landmark Patient #	1	2	3	4
Left head (DT)	3.53	1.20	2.51	4.37
Left head (MAF)	3.44	1.00	2.11	3.30
Right head (DT)	1.11	1.55	1.03	3.78
Right head (MAF)	1.33	1.59	0.88	3.19

Table 4.1: Registration results on femoral head centers. Distances in millimeters between the expected femoral head centers and those obtained from the registration (locally affine: MAF ; dense transformation: DT).

The results of this method are at least as good as the results obtained through non–rigid registration. This fact becomes even more evident if computation time is taken into account (3 minutes as opposed to 10 minutes for a fully non–rigid approach). This method performs the registration based on specific zones and ensures consistent results all over the image.

Therefore, seeking a locally affine transformation using zones around bone struc-
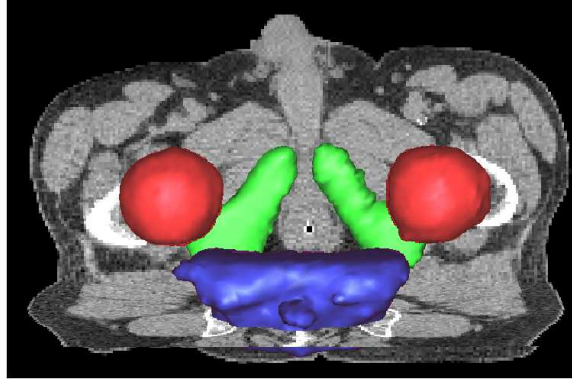
Figure 4.8: 3D view of the 5 different zones defined around bone structures that were used for the registration of the images in our database. Left and right femoral heads are shown in red, the sacrum bone is shown in blue, and the left and right ischiatic tuberosities are displayed in green. The background image is the reference CT image used for registration.

tures is better adapted to the registration of lower abdomen images with highly variable soft tissues than a dense transformation solution, which would try to match the entire floating image.

How We Apply Locally Affine Registration   In order to put our database images in a common frame of reference, the locally affine registration algorithm has been applied using zones defined around 5 pelvic bone structures: the femoral heads, the sacrum bone, and both ischiatic bones, as illustrated in figure 4.8. The chosen reference image is of size 256x256x80 (sagittal, coronal and axial planes, respectively). Its voxel size is 1.87 mm x 1.87 mm x 3 mm. This image was chosen as reference because of its good bone structure contrast and definition, and also because its relatively high voxel size helps to avoid the creation of partial volume effects due to interpolation when registering lower voxel size images. Sample results are shown in figure 4.9.

4.3.2   Image Cropping

4.3.3   Determination of the Presence of a Contrast Agent

When we determine whether the bladder shows the presence of a contrast agent or not, the bones are not taken into account in the registered image. We then establish a region of interest based on a probability map of the bladder's position in the registered images and, within this region, we seek for the highest intensity voxel located in a neighborhood with low intensity variability. This will be our **seed** voxel (see figure 4.11). The probability map is obtained by accumulating the intensities of the binary expert segmentations of the bladders in the registered images, as shown
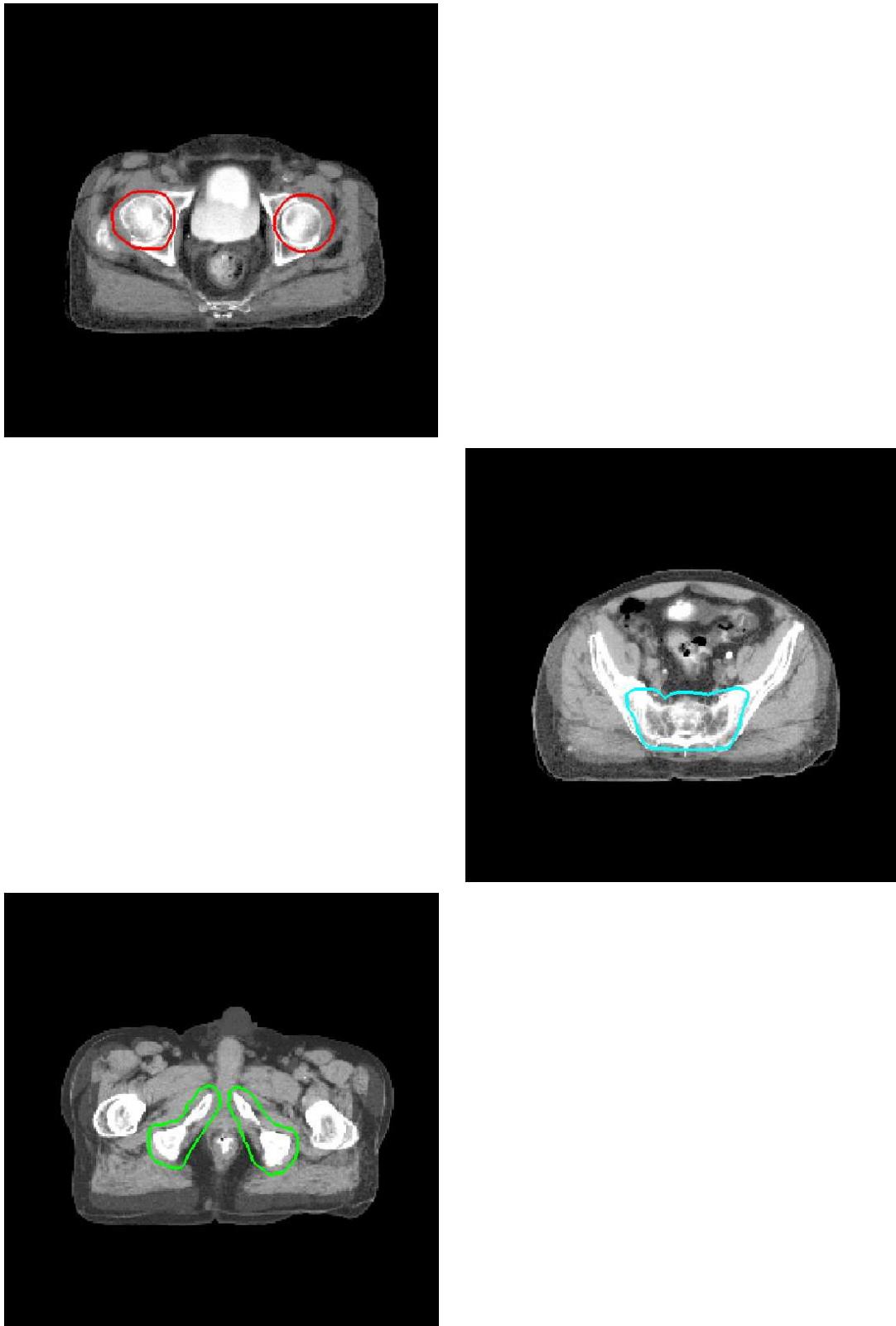
Figure 4.9: Axial views of the registered image, with the zones used during registration outlined. The anatomical coherency of the registered image has been preserved. From top to bottom, femoral heads' zones (red), sacrum zone (blue) and ischiatic tuberosities' zones (green).
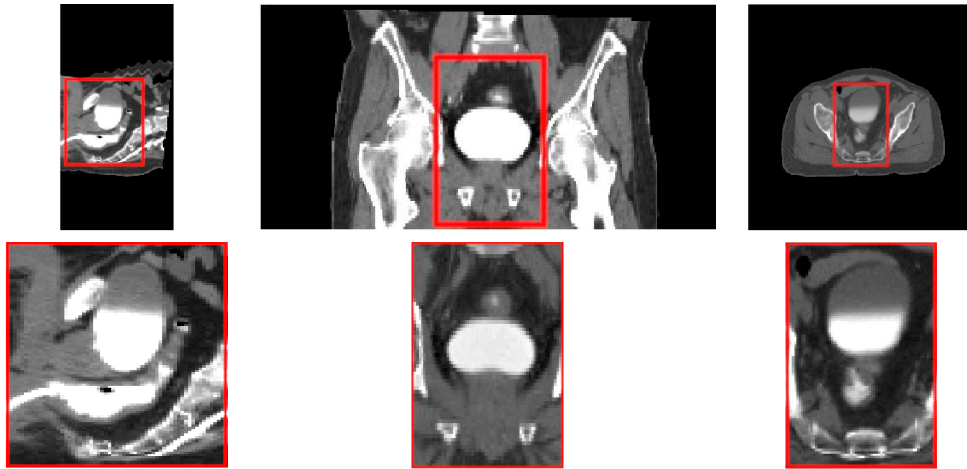
Figure 4.10: Registered image before (top) and after (bottom) cropping. From left to right, sagittal, coronal and axial views.

on the left hand side of figure 4.11. Since the images have been registered based on the pelvic bone structures, the positions of the latter have become known, and they can therefore be eliminated (or simply ignored) when determining the region of interest for the bladder.

The fact that CT image voxel intensities are defined in standard Hounsfield Units (H.U.) allows us to define a fixed threshold level for deciding whether the found (seed) voxel belongs to a contrasted soft tissue (intensities around +200 to +1000 H.U.) or to a non–contrasted soft tissue (intensities of about +40 H.U.). We have established the level from which tissues are considered as contrasted to be +200 H.U.

If the intensity of a small neighborhood around the chosen seed voxel corresponds to the intensity of non–contrasted soft tissues (based on the threshold defined above), the bladder is considered as non–contrasted. Otherwise, it is considered as showing a contrast agent, and we must determine whether it is homogenously contrasted (one zone of homogenous grey–level values) or no–homogenous. Since the location of the contrast agent is influenced by gravity, it tends to gather in the lower portion of the bladder, so in the non–homogenous case we can speak of a very contrasted "lower" zone and a less contrasted "upper" zone.

In all three cases, we proceed to approximate the structure, as described in the next section.

4.4 Initial structure approximation

Next, a binary approximation of the bladder is computed. In order to obtain this approximation, we have devised our own **Progressive Region Growing**, a modified version of seeded region–growing that incorporates mathematical morphology operations. The method is detailed in algorithm 1.
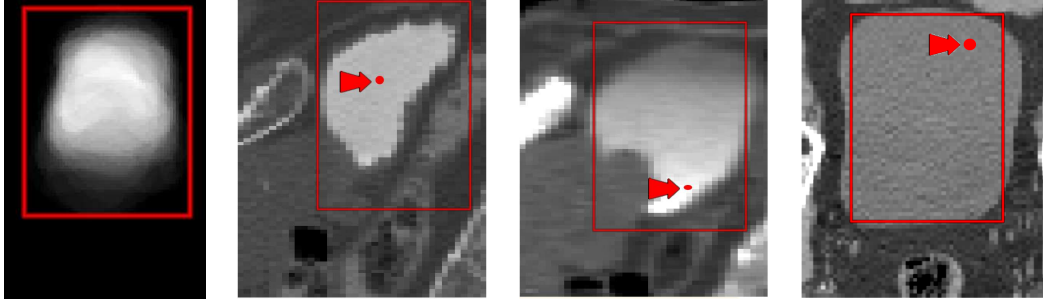
Figure 4.11: A starting point is sought within a region determined by the probability map of the bladder's position in registered images. The most contrasted voxel of each image within that region is chosen as seed. From left to right: region (red) determined by the probability map and the chosen seed (pointed by the red arrow) in homogenous contrasted, non–homogenous, and homogenous non–contrasted bladder images.

Algorithme 1 The Progressive Region Growing algorithm.

Input: Image (*image*) and seed point (*seed*)

Output: The resulting approximation RG

$RG = seed$

Compute intensity mean M and std. dev. SD around *seed*

Define *lowThreshold* and *highThreshold* based on M, SD and *seed*

while *(RG is smooth in 3D)* & *(lowThreshold not too low)* **do**

    Decrease *lowThreshold*

    $RG = $ RegionGrowing(*image*, *seed*, *lowThreshold*, *highThreshold*)

    MorphologicalClosing(RG, *StructuringElement*)

    Check3DSmoothness(RG)

end

Each step corresponds to a traditional region growing with a progressively softer inclusion criterion, followed by a mathematical closing using a spherical structuring element of a 5 voxel radius in all directions (given the image voxel size, it is equivalent to 9.3 x 9.3 x 15mm) . The *lowThreshold* and *highThreshold* values are initially defined as *M-2*SD* and *M+2*SD*, respectively, while the value of *lowThreshold* is always required to be greater than 0. The inter–slice thickness of our images, which is different depending on the direction (typically, 1.875 mm in X, 1.875 mm. in Y and 3 mm in Z), is taken into account for the definition of the radius of the structuring element in each direction. Every time an image voxel is examined for inclusion, the structuring element is used to check a neighborhood around the candidate. If a sufficient (user–determined) percentage of neighboring voxels also corresponds to the intensity criterion, the candidate voxel is included in the result (we used 80%). Otherwise, it is discarded.

The size of the structuring element has been chosen to be small enough to fit into the bladder, but large enough so that it does not fit into surrounding organs that are comparatively "thin" such as the seminal vesicles or the colon. The morphological step aids in the prevention of leakages into those organs, which must not be included in the computed approximation of the bladder.

We begin by applying a small number of progressive region growing steps that do not enforce the smoothness constraint, in order to overcome possible irregularities in the initial growth. The enclosed region then continues to be enlarged as long as the result remains "smooth" in 3D. The smoothness criterion that we use is the following: if the resulting approximation has leaked into thin neighboring structures, there will be a sudden, drastic change in the area of the segmentation in nearby (even successive) z slices. This sudden change can be detected by looking at the derivative of the area in successive slices.

An optimization of progressive region growing has been implemented in order to avoid computing the whole approximation at each iteration, but just including the newly accepted voxels each time.

4.4.1   Homogenous Non–Contrasted Bladders

In the case of homogenous, non–contrasted bladders, one progression of our modified region growing suffices to approximate the whole structure. An example is illustrated in figure 4.12.

4.4.2   Contrasted Bladders

In the case of bladders showing the presence of a **contrast agent**, the most contrasted zone is approximated first, since the characteristics of the chosen seed voxel (most contrasted point, within a low–variance neighbourhood, and with a high likelihood of belonging to the bladder) will place it in that region.

The modified, progressive region growing is applied, as shown in figure 4.14, with a lowest tolerable threshold of +200 H.U. (i.e., the region is grown while the
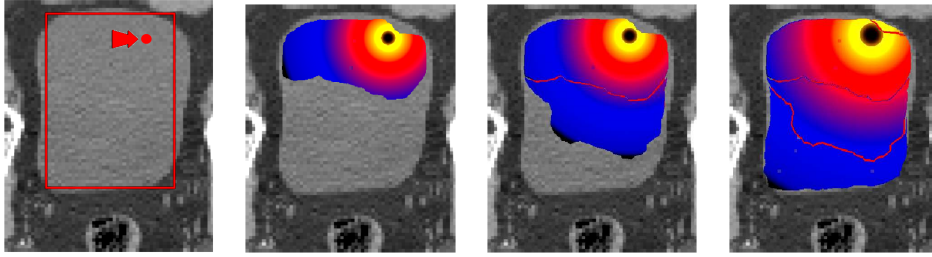
Figure 4.12: A sample progression of the modified region growing to generate an approximation of an homogenous, non–contrasted structure.
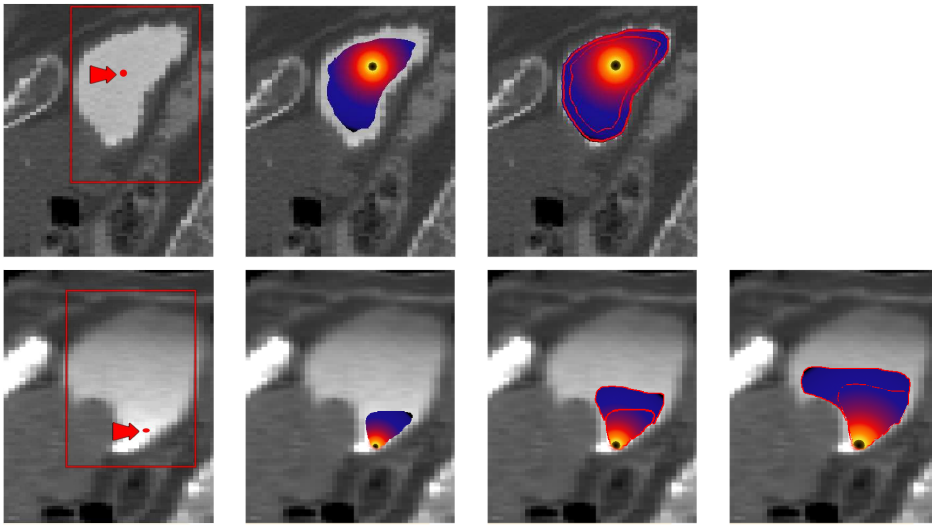
Figure 4.13: A sample progression of the modified region growing to generate an approximation of contrasted structures or zones.

intensities correspond to contrasted tissues).

Once this progression stops, we must still determine whether the bladder in the image is homogenous or not. In order to do this, we search for a second seed voxel that would correspond to a potential "upper" (in the Y sense), non–contrasted zone. To this end, a search region is determined above the contrasted zone that was just approximated, and a seed is sought within it. This seed must be located in this zone, and within a neighborhood of homogenous intensity corresponding to that of non–contrasted soft tissue.

- If such a voxel is found, we assume that the bladder is non–homogenous, and that a seed for its upper, non–contrasted region has been found. A second progression of region growings is then launched in order to approximate it.

- On the other hand, if no such voxel is found, the bladder is considered to be homogenously contrasted. In that case, the approximation of the contrasted zone is the approximation of the whole structure.
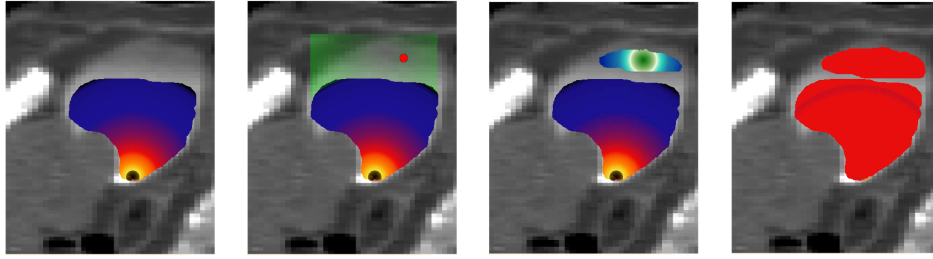
Figure 4.14: A second seed is sought for the upper, non–contrasted region. If one is found, a second progression of the modified region growing is launched to generate the approximation of non–contrasted zone.
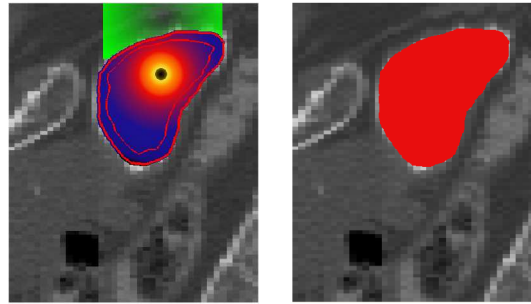
Figure 4.15: A second seed is sought for the upper, non–contrasted region. If none is found, the approximation of the structure is that of the contrasted zone.

The search for a second seed voxel for a non–homogenous bladder and the subsequent evolutions are depicted in figure 4.14. In the case of an homogenously contrasted bladder, a second seed with the desired characteristics is unlikely to be found; therefore, the approximation that was just computed is considered as having enclosed the whole bladder (figure 4.15).

In all cases, the process of progressive region growing provides us with a 3D binary image corresponding to the approximation of the bladder in the image, as well as its intensity characteristics, including the (in–)homogeneity of the structure, the mean and the variance of each zone. These parameters will be used to guide the deformation of a simplex mesh (section 4.6).

4.5   Mesh deformation: binary stage

The binary approximations computed in the previous section serves to guide the preliminary stages of deformation (both global and local) of an initial simplex mesh. Since the bladder is a structure homeomorphic to a sphere, the initial mesh is a sphere whose radius is the average (largest) diameter of the manually segmented bladders in our database.

In the case of non–homogenous bladders, the approximation consists of two con-

nected components (upper and lower zones). In order to generate only one binary component to guide the mesh, the two regions are joined using mathematical morphology tools (an opening operation). For homogenous bladders, the approximation does not need to be modified, and is thus used "as is".

4.5.1   Geometry of a 3D simplex mesh

A **Simplex Mesh**[Delingette 1994] is a representation of discrete surfaces that presents a regular structure in which each vertex is connected to exactly 3 neighbors. In surface meshes (2–simplex meshes), the 3 neighbors of vertex p_i (p_i^1, p_i^2 and p_i^3) form a plane that is normal to the vector n_i

$$n_i = \frac{p_i^1 \wedge p_i^2 + p_i^2 \wedge p_i^3 + p_i^3 \wedge p_i^1}{||p_i^1 \wedge p_i^2 + p_i^2 \wedge p_i^3 + p_i^3 \wedge p_i^1||} \tag{4.1}$$

Let C_i be a circle of radius r_i centered at c_i, circumscribed to the three vertices (p_i^1, p_i^2, p_i^3), and let S_i be the sphere of radius R_i centered at o_i, circumscribed to the tetrahedron (p_i^1, p_i^2, p_i^3).

The **metric parameters** ε_i^1, ε_i^2 and ε_i^3 ($\sum_j \varepsilon_i^j = 1$, $\forall j, 0 < \varepsilon_i^j < 1$) are the barycentric coefficients of projection $p_i^\perp$ of p_i on the plane of its 3 neighbors. They control the relative space between a vertex in the mesh and its neighbors.

The **simplex angle** constitutes a measure of the local curvature at vertex p_i and is defined as follows:

$$\begin{cases} \varphi_i \in [-\pi, \pi] \\ sin(\varphi_i) = \frac{r_i}{R_i} sign(p_i p_i^1 . n_i) \\ cos(\varphi_i) = \frac{||o_i c_i||}{R_i} sign(o_i c_i . n_i) \end{cases}$$

The simplex angle can be interpreted as a geometrical angle in the plane (p_i, c_i, o_i). The set of parameters ε_i^1, ε_i^2, φ_i suffices to define the shape of a 2–simplex mesh, apart from a simple scaling.

The geometry of 2–simplex meshes is illustrated in figure 4.16.

4.5.2   Mesh Evolution

For the deformation step, a hierarchical approach is used: the initial mesh undergoes rigid and affine transformations that globally place the mesh as accurately as possible over the binary approximation of the bladder. After this step, the mesh begins to progressively undergo globally-constrained deformations [Montagnat 1998], which allow it to adapt itself to smaller variations in the data.

The position of vertex i of the mesh at time $t + 1$ (V_i^{t+1}) is computed following equation 4.2.

$$V_i^{t+1} = V_i^t + (1 - \delta)(V_i^t - V_i^{t-1}) + \lambda(\alpha f_i^{int}(V_i^t) + \beta f_i^{ext}(V_i^t)) + (1 - \lambda)f_i^{global} \tag{4.2}$$
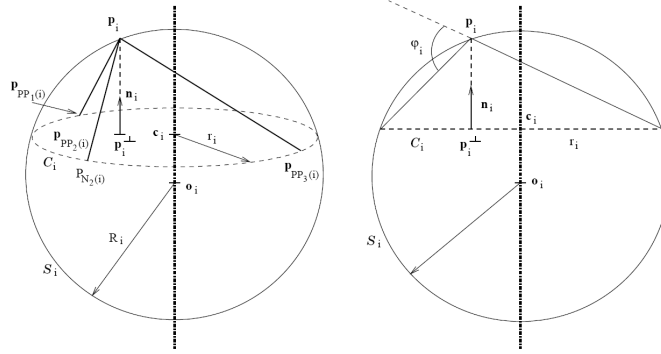
Figure 4.16: Geometry of 2–simplex meshes (credit to [Montagnat 1999a]).

where λ is the *locality* parameter, δ is a damping coefficient, α controls the influence of internal (i.e. regularization) forces for that vertex, and β weights the external (i.e. image) forces acting on the vertex. We start with $\lambda = 0$, a purely global (rigid + affine) deformation, and move progressively towards a more local deformation ($0 < \lambda < 1$).

The idea behind each of these forces in the context of simplex meshes is the following: from the current mesh, a second, *target* mesh (considered "ideal") is computed, and the first one is pulled towards it, with the aim of improving the segmentation.

Global force (f^{global}) serves to align a simplex mesh as well as possible with the data found in the image. In other words, the global force considers the target mesh as an affine deformation of the mesh at the previous iteration. When parameter λ in equation 4.2 is equal to 0, global forces dominate the deformation process.

The global force is computed through an *iterative closest point* algorithm[Besl 1992, Zhang 1994], which consists of the iteration of 3 main stages:

1. *Pairing* Each model's vertex is aligned with a data (image) point.

2. *Estimation* A transformation is computed in order to minimize the distance between the transformed model and the data points.

3. *Update* The transformation is applied to the model.

First, each vertex is put in correspondence with a "salient" data point (for example, a point of strong intensity gradient). Let $cp(V_i^t)$ be the data point associated to vertex V_i^t. Given n pairings, at time t the transformation T^t is sought in the space of affine transformations such that the sum of the squared distances between the vertices of the deformed model and the corresponding data points is minimized, as shown in equation 4.3.

$$T^t = argmin_{T^t \in T_{affine}} \sum_{i=0}^{d-1} ||T^t(V_i^t) - cp(V_i^t)||^2 \qquad (4.3)$$

T^t is estimated within the space of affine transformations. Registration is achieved through the application of a global force field defined by $f_{global}(V_i^t) = T^t(V_i^t) - V_i^t$.

An **affine** transformation can be seen as the combination of a rigid transformation and a translation, without angle preservation. This transformation has 12 degrees of freedom and can be expressed as a base changement matrix A (3x3) and a translation t:

$$\forall T = (A, t) \in T_{affine}, T(p_i) = Ap_i + t \qquad (4.4)$$

The optimal translation is obtained by the displacement of the barycenter, and the criterion to be optimized in the barycentric space is:

$$\forall C(A) = \sum_{i=1}^{n} ||Ap_i - cp(p_i)||^2 \qquad (4.5)$$

The optimum that minimizes the norm of the data's noise is obtained when $\frac{\partial C(A)}{\partial A} = 0$, meaning that $A = \sum_{yx}(\sum_{xx})^{-1}$, where $\sum_{xx} = \sum_{i=1}^{n} p_i p_i^T$, and $\sum_{yx} = \sum_{i=1}^{n} PPP(p_i)p_i^T$ is the cross–covariance matrix.

Internal forces f^{int} involve a regularization of the mesh. One of the advantages of simplex meshes is that this regularization is easy to implement by using the concept of **simplex angle**.

The internal force can be seen as an attraction of model vertex p_i towards the point $\tilde{p}_i$ which is defined by its 3 neighbors and by the parameters $\tilde{\varepsilon}_i^1, \tilde{\varepsilon}_i^2, \tilde{\varphi}_i$. Metric parameters $\tilde{\varepsilon}_i^1$ and $\tilde{\varepsilon}_i^2$ are defined according to the desired distribution of the vertices on the model's surface, while $\tilde{\varphi}_i$ allows the determination of the type of continuity expected of the surface. This curvature constraint imposes a certain regularity of the simplex angle, and therefore of the discrete curvature of a surface:

$$\tilde{\varphi}_i = \sum_{p_j \in V_\eta(i)} \frac{\varphi_j}{|V_\eta(i)|} \qquad (4.6)$$

The value of the simplex angle at each vertex tends to equal that of its neighbors. The resulting internal forces make the model converge towards a shape of constant curvature which, in the case of 3D simplex meshes of genus 0, is a sphere: this is the *C1* constraint. The *C0* constraint would consist in minimizing the simplex angle. In the rest of this manuscript, the internal constraint used will be the *C1* one.

The neighborhood of a vertex i is defined as the set $B_r(i)$ of vertices located within a sphere of radius r. The parameter of the topological size of the neighborhood η corresponds to the **rigidity** of the surface. The mesh deformations are more localized if the rigidity parameter is small, and affect the surface on a larger

zone when the rigidity parameter increases. The rigidity parameter allows for the smoothing of the curvature on a neighborhood of variable size.

External force f^{ext} is a data–driven force that tries to align the current mesh with salient points in the image.

In order to guide the deformation of the simplex mesh, we determine at each model vertex an external forces directed along the direction of the normal to the model's surface. Following [Delingette 1999], the data point to serve as attractor will be sought within a certain distance along this normal. This approach has 2 advantages: on one hand, a limitation on the maximum search distance for a data attractor reduces the potential influence of outlier points, and on the other hand, it speeds up the process of finding such a point by restricting the search space.

In our case case, since the image is binary, the structures's borders are well defined, the chosen attractor is the point along the surface normal that shows the highest intensity gradient norm value.

Parameters: λ is a *globality* coefficient: if it equals 1, only a global (affine) deformation is possible. As λ decreases, more local deformations (i.e., guided by internal and external forces) are authorized to the mesh. At the beginning of the deformation process, only global deformations are allowed ($\lambda = 1$) in order to initially position the model over the image data. Throughout the deformation process, the value of λ is progressively lowered, to allow for more "local" deformations so that the model can adjust to smaller details in the target image.

β is the *image data* coefficient. With $\beta = 0$, the mesh undergoes only a regularization process.

The δ parameter weights the importance of inertia on the deformation process: the previous iteration is considered to have an influence on the following one.

The initial mesh deformation over a binary approximation of the target structure makes the whole procedure more robust in the presence of noisy data and outlier points in the original image. Some initial deformation stages are shown in figure 4.17.

4.5.3 Automatic division of the mesh into zones

In order to refine the result of the initial mesh deformation, we use the image itself, as opposed to the computed approximation. However, the intensity characteristics of the underlying bladder in the image must be taken into account. We adjust the deformable model to the type of bladder present in the image as follows:

For **non–homogenous bladders**: A Chamfer distance map is computed with respect to the upper and lower zones in the bladder, whose approximations were obtained through progressive region growing (see algorithm 1). These distance maps are used to label each vertex of the simplex mesh as belonging to the "upper" (non–contrasted), "middle" (interface, intensity gradient zone between upper and lower) or "lower" (contrasted) zone. Each portion of the model will evolve under different
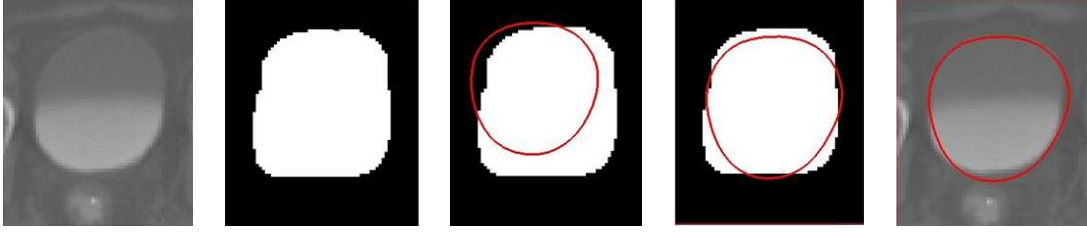
Figure 4.17: From left to right, the target non–homogenous bladder in an image, the generated binary approximation, an initial mesh before and after progressive deformations to fit the approximation, and the result superimposed over the original target bladder. This resulting segmentation, seen in red over the original image, cannot be further refined without taking into account the intensity (in–)homogeneities within the structure.
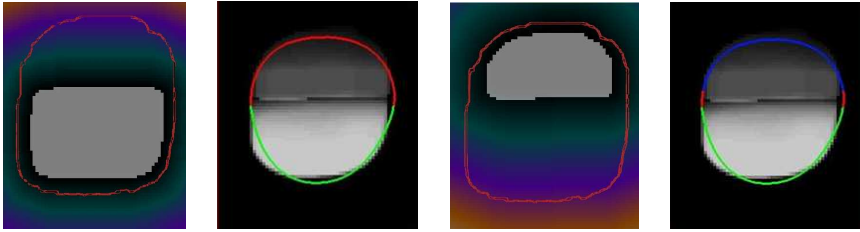
Figure 4.18: In order to divide the mesh into zones that correspond to the intensity ranges in the underlying bladder, Chamfer distance maps to the upper and lower zone approximations are computed. The model's vertices are assigned to one or the other according to their distance values to each of the zones. An intermediate zone, corresponding to an intensity gradient between the upper and lower, is also defined.

forces, according to the characteristics of the target structure in the nearby region. This is illustrated in figure 4.18. The resulting divided mesh is shown in figure 4.19.

The middle zone is established in order to avoid the "wasp–waisted" results that occur with only two regions. Especially for very contrasted bladders, and because of partial volume effect, the intermediate zone will contain an intensity range that matches neither the "pure" upper nor lower portion of the bladder.

For **homogenous bladders**: since the whole bladder has similar intensity properties, the mesh will deform itself globally under the same rules. Therefore, no zone division is needed.

4.6   Mesh deformation: gray–scale stage

Once the mesh properly delineates the binary approximation of the bladder, the segmentation is refined, each mesh zone will evolve guided by the registered image itself and by a new histogram based force that we have devised to this end.

We propose an extended framework of deformable-model based image segmenta-
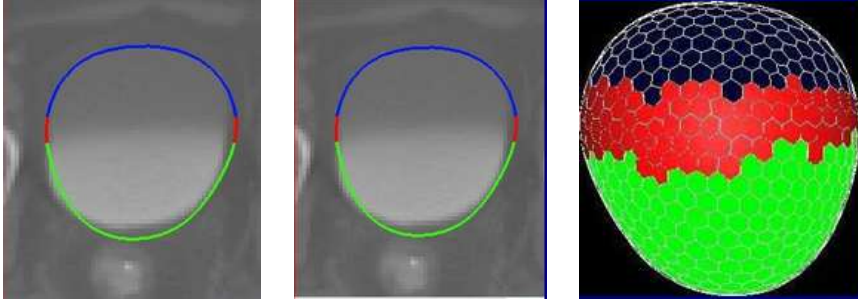
Figure 4.19: Divided mesh, showing the upper, middle and lower zones. If the mesh is deformed to fit an homogenous bladder, no zone division is performed (i.e., it has only one region).

tion where the sought active contour or surface $S(\mu)$) results from the minimization of an energy. The surface S is pulled both towards S_s, a "smooth" surface that lies in the vicinity of $S(\mu)$ (for regularization purposes) and S_i, an estimated target surface corresponding to the boundaries of an anatomical structure in an image.

We propose a new **histogram–based** approach for estimating $S_i(\mu)$ given $S(\mu)$ and I. In this method, the boundary points are assumed to be the ones for which the *inside voxels* have a high probability of belonging to the inside region while the *outside voxels* have a low probability of belonging to the inside region

Rather than basing the segmentation on an intensity range, we rely on the histogram of the interior of the current target structure, making no assumption on the intensities found in surrounding organs or on previous cases (training data).

If we assume that the normal $N(\mu)$ at $S(\mu)$ is oriented outwards, the boundary surface $S_i(\mu)$ can be computed at each iteration as $S(\mu) + s_\star$, with:

$$s_\star = \arg \min_{s \in [-L;L]} E_s \qquad (4.7)$$

where

$$E_s = \sum_{v=-L}^{v=L} G_\sigma(|v - s|) * f(I(S(\mu) + v\,N), \mu, \sigma, sgn(v - s)) \qquad (4.8)$$

where s is the position of each vertex of the final mesh we want to evaluate, v is the position of the voxels along the normal of the mesh at vertex s, and $f(i, \mu, \sigma, sgn)$ is a confidence estimation.

This confidence function is a piecewise constant function designed so that it will heavily penalize the energy term if a voxel is mistakenly placed inside or outside the mesh, and reward (i.e., lower the energy) if a voxel belonging to the inside of the structure is correctly placed inside the mesh. It depends on two terms: $|\frac{I(S(\mu)-\mu)}{\sigma}| \leq 2$ and $sgn(v - s)$. For instance, if the first term is false (i.e., the voxel's intensity is not compatible with the intensities found inside the structure) and the second term is true (i.e. the voxel is located inside the mesh), a positive penalization value is added

to the energy term. Function G_σ defines a weight for the voxels that are taken into account at each iteration step; it may be a Gaussian p.d.f., a generalized rectangle function, or a combination of the two. The parameters are fully adjustable, to penalize more (or less) a non–homogeneity inside the structure or zone. This force is illustrated in Figure 4.20.

$$f(I(S(\mu)+v\ N), \mu, \sigma, sgn(v-s)) = \begin{cases} +10, & \text{if } |\frac{I(S(\mu)-\mu}{\sigma}| > 2 \quad and \quad sgn(v-s) \le 0 \\ -1, & \text{if } |\frac{I(S(\mu)-\mu}{\sigma}| \le 2 \quad and \quad sgn(v-s) \le 0 \\ -1, & \text{if } |\frac{I(S(\mu)-\mu}{\sigma}| > 2 \quad and \quad sgn(v-s) > 0 \\ +1, & \text{if } |\frac{I(S(\mu)-\mu}{\sigma}| \le 2 \quad and \quad sgn(v-s) > 0 \end{cases}$$
$$(4.9)$$

As can be noticed from equation 4.9, an inside voxel that does not belong is much more heavily penalized in terms of energy value than an outside voxel that belongs inside the model.
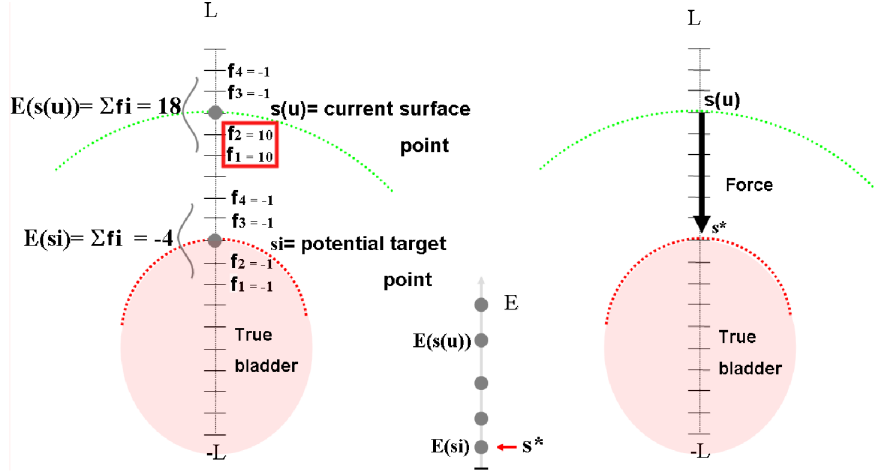
Figure 4.20: Image voxels that are mistakenly included in, or excluded from the segmentation are penalized with locally greater values of f (exemplified in the red box in the picture), and a subsequent increase in the total energy E. Voxels that are correctly included or excluded in the segmentation lower the total energy. The mesh will be pulled towards the potential surface that has minimal energy (s_*).

4.7   Results and Analysis

The accuracy of an individual experimental (in our case, automatic) segmentation is usually given through some measure of a region's overlap and its distance from the ground truth, such as the Hausdorff distance ([Huttenlocher 1993]). Let $A = a1, ..., am$ and $B = b1, ..., bn$ denote two finite point sets. Then the **Hausdorff distance** is defined as

$$H(A, B) = max(h(A, B), h(B, A)) \qquad (4.10)$$

I	H	Sensit.	PPV	RHD	I	H	Sensit.	PPV	RHD
1	NH	0.94	0.73	2.7	11	H	0.75	0.98	5.7
2	H	0.96	0.80	3.0	12	H	0.93	0.86	3.3
3	H	0.87	0.81	3.7	13	H	0.91	0.95	5.3
4	NH	0.94	0.81	4.0	14	H	0.92	0.92	2.0
5	H	0.97	0.78	3.0	15	H	0.88	0.97	2.7
6	NH	0.93	0.81	3.0	16	H	0.91	0.95	2.0
7	NH	0.94	0.89	2.0	17	NH	0.84	0.93	3.7
8	H	0.92	0.79	4.0	18	NH	0.91	0.90	2.0
9	H	0.97	0.88	2.3	19	NH	0.83	0.86	4.0
10	H	0.80	0.94	4.7	20	H	0.76	0.83	3.7

Figure 4.21: Sensitivity, Positive Predictive Value and robust Hausdorff distance (95% quantile, all values in mm.) of the automatic segmentation with respect to the ground truth in homogenous (H) and non–homogenous (NH) bladder images. The average sensitivity and positive predictive value are of 0.89 and 0.87 respectively, with standard deviations of 0.066 and 0.072. The mean robust Hausdorff distance (i.e., 95% quantile) is 3.34 mm with a standard deviation of 1.086 mm. (Maximum, minimum) value pairs are of (0.97, 0.75), (0.98, 0.73) and (2.0, 5.7) for sensitivity, positive predictive value and robust Hausdorff distance, respectively.

where

$$h(A, B) = max_{a \in A} min_{b \in B}(||a - b||) \tag{4.11}$$

Another strategy for evaluating a single–object segmentation is to view each voxel as an instance of a detection task, which gives rise to metrics for sensitivity and Positive Predictive Value, among others. **Sensitivity** is the true positive fraction of the segmentation, the percentage of voxels in an image correctly classified as lying inside the object boundary. Sensitivity is defined as follows:

$$Sensitivity = \frac{TP}{TP + FN} \tag{4.12}$$

where TP is the number of true positives, and FN is the number of false negatives. A sensitivity of 1 in our case means that the automatic segmentation includes the manual (expert) segmentation. **Positive Predictive Value** (PPV), the ratio of true positives to the sum of true positives and false positives, is another possible detection–based accuracy metric. PPV indicates the percentage of positive classifications that are correct. It can be defined as

$$PPV = \frac{TP}{TP + FP} \tag{4.13}$$

where TP is the number of true positives, and FP is the number of false positives. A PPV of 1 means that the manual (expert) segmentation includes the automatic segmentation. Therefore, a sensitivity and a PPV of 1 indicate that the automatic and manual segmentations match exactly. The above measures are illustrated in Figure 4.22.
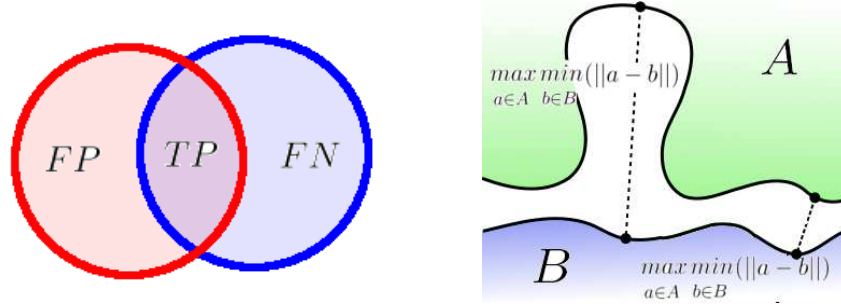
Figure 4.22: The image on the left shows hypothetical automatic (red) and ground truth (blue) segmentations. The sensitivity of the automatic segmentation is the ratio $\frac{TP}{TP+FN}$, while the positive predictive value is defined as $\frac{TP}{TP+FP}$. On the right, the image illustrates the computation of the Hausdorff distance between surfaces A and B.

Our method has been tested in a database of CT images showing both homogenous and non–homogenous bladders (see also [Costa 2007b]). Figure 4.21 shows some quantitative measures of the results. The sensitivity and the positive predictive value of the automatic segmentation with respect to the expert delineation have an average of 0.89 and 0.87 respectively, with standard deviations of 0.066 and 0.072. The mean robust Hausdorff distance [Huttenlocher 1993] (i.e., 95% quantile) is 3.34 mm with a standard deviation of 1.086 mm. The segmentation process on a registered image takes less than a minute on a standard laptop computer. Some example results can be seen in Figure 4.23.

The results are quite good, despite the variable quality of both the images and the expert segmentations. The modified region growing algorithm provides a good initialisation for both homogenous and non-homogenous bladders, while the mesh deformation steps improve or correct the final segmentation and apply a shape regularization as well.

The automatic segmentation is sometimes misled by a fuzzy bladder–prostate interface, which causes a "leakage" of the model into the prostate and, consequently, an increased distance with respect to the expert delineation. We are able to partially avoid this by imposing strong regularization constraints on the model, but, as a side effect, the mesh is prevented from attaining high–curvature zones within the bladder. To address both problems and further improve the results, we propose a framework for the simultaneous segmentation of the prostate and bladder with non–overlapping constraints on the models in the next chapter.

Figure 4.24 illustrate the main difficulties encountered, mostly due to fuzzy borders with neighboring organs. The resulting segmentations for entries 3 and 20 in table 4.21 show a slight under segmentation (seen in the axial slice). A portion of the prostate or of the sigmoid may be sometimes included by the mesh (seen in the sagittal slice), due mainly to a fuzzy interface, i.e., a lack of border definition.
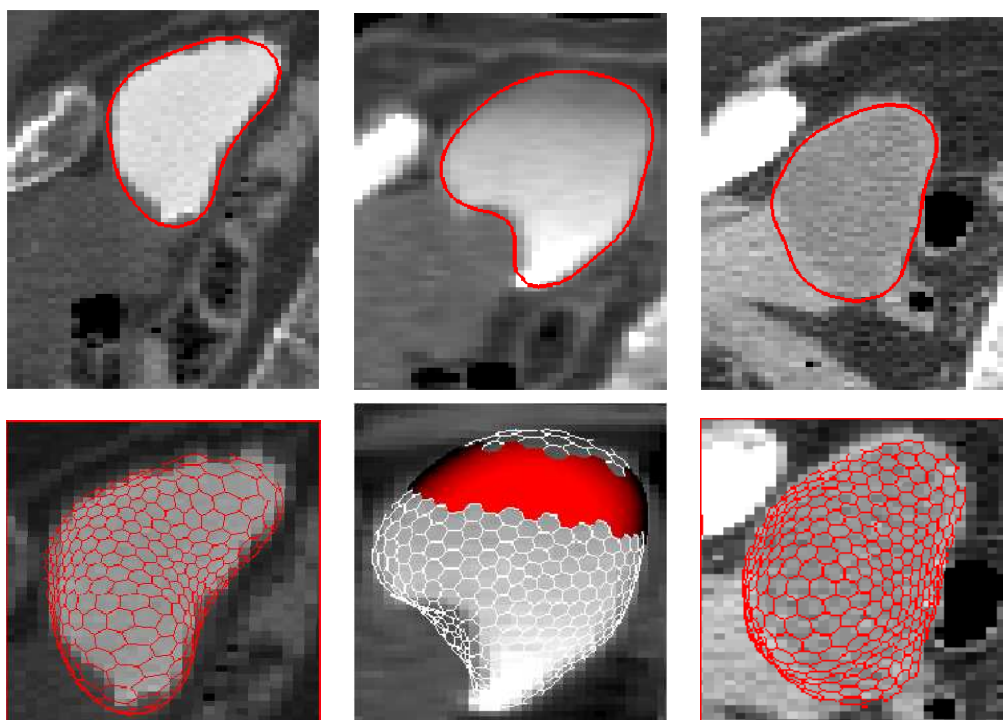
Figure 4.23: Some segmentation results (sagittal and 3D views), with an homogenous contrasted bladder (left, entry 13 in table 4.21), a non–homogenous bladder (center, entry 7 in table 4.21) and an homogenous, non–contrasted bladder (right, entry 16 in table 4.21). In the non–homogenous case, the 3 zones of the resulting mesh (upper, middle and lower) can be seen.
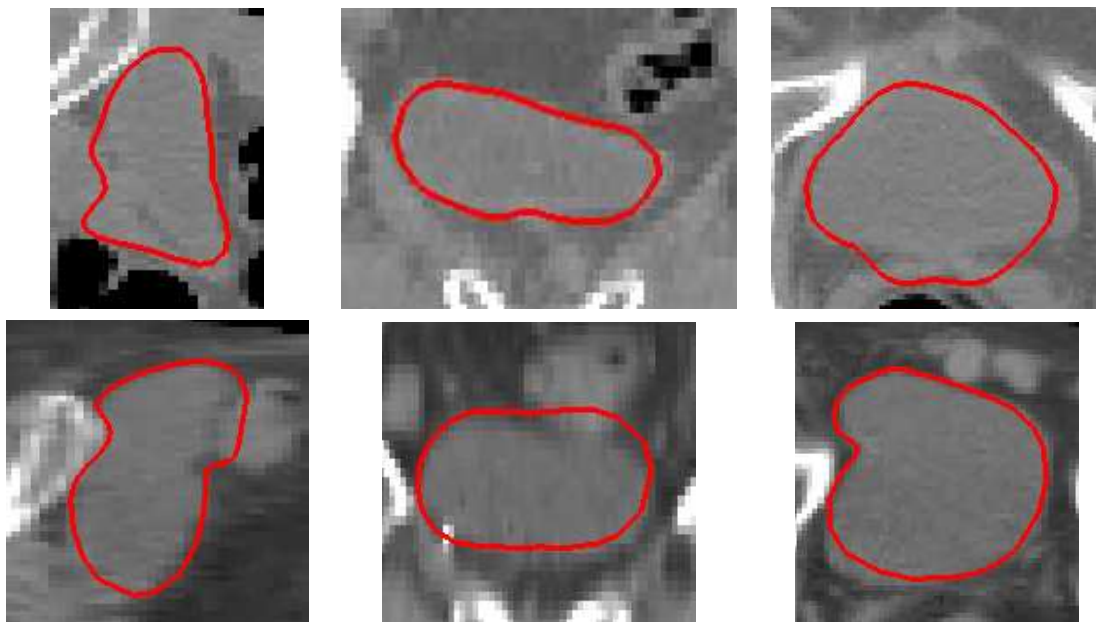
Figure 4.24: "Leakages" that may occur due to a fuzzy bladder border. From left to right, sagittal, coronal and axial views of the automatic segmentation results for the images corresponding to entries 3 (top row) and 20 (bottom row) in table 4.21 (worst cases encountered).

Coupled Segmentation of Bladder and Prostate

5.1 Challenges in Prostate Segmentation

Just like its surrounding structures (bladder and rectum), the prostate (figure 5.1) is a soft tissue, and thus in the absence of a contrast agent its density in Hounsfield Units is undistinguishable from that of its neighbors. One can appreciate the difficulty of the segmentation problem in this context: the prostate organ presents no distinct "edge" in the CT scan itself (e.g., see image 5.2), so a purely edge–based segmentation method would not be reliable.

This task is also difficult for radiation oncologists who perform the segmentation manually. Even determining "ground truth" in such cases is subjective, and often times different experts' segmentations based on the same image show important differences (see and example in Figure 5.2). However, the experts make use of their knowledge in pelvic anatomy and take the intensity similarities into account while contouring. In our case, and since the prostate shape shows a certain shape coherency among patients, the results of a shape study prove to be useful for its delineation.

In the case where a contrast agent has been given to the patient, the bladder becomes more visible in the image, and so does its common interface with the prostate. However, different contrast levels within the bladder increase or decrease the definition of its border, making it well defined and visible in some zones while still blurry in others. We show examples of this phenomenon in figure 5.3.
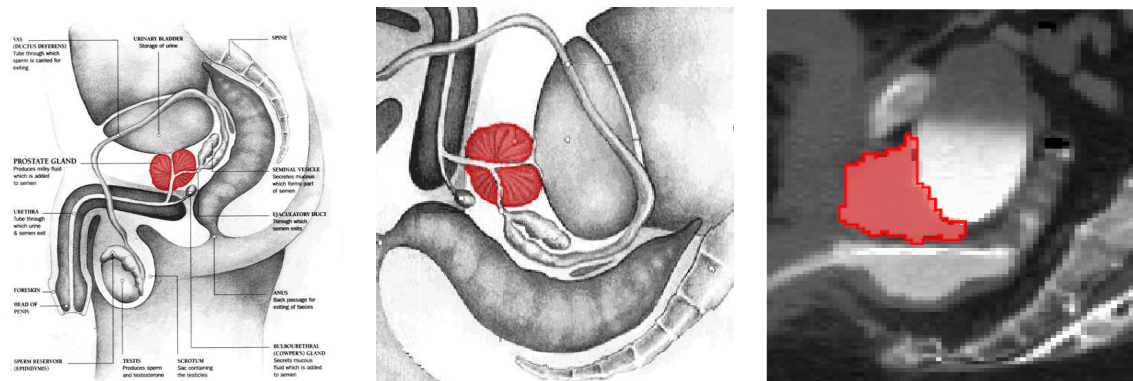
Figure 5.1: The prostate on a standing patient (left), and how it is seen when the patient is lying down (center and right), all shown in red, sagittal views.
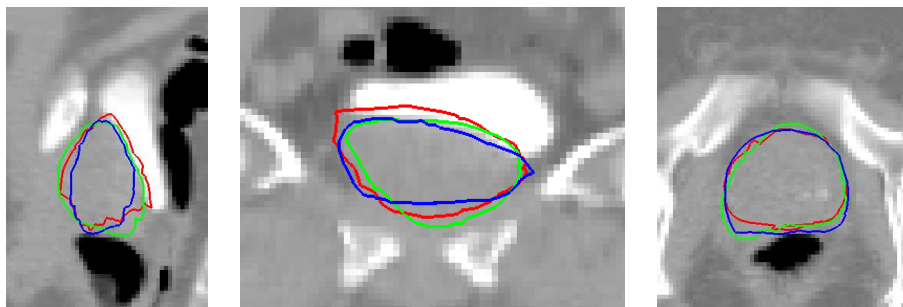
Figure 5.2: Inter expert variability in the delineation of one prostate. From left to right, sagittal, coronal and axial views.
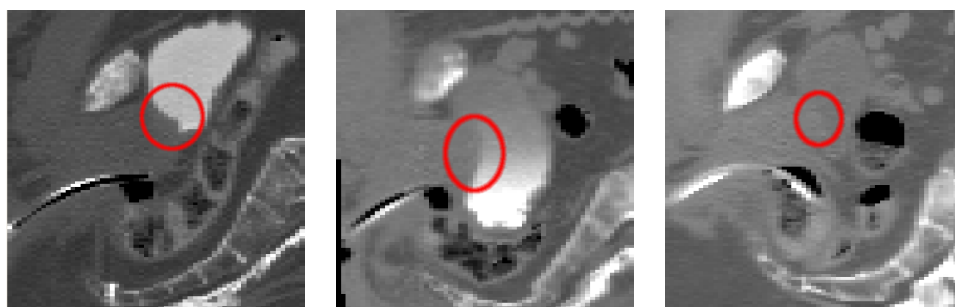
Figure 5.3: The bladder–prostate interface (encircled in red) may be clearly visible (left), visible only in certain regions (center) or fuzzy (right).

Once again, and just like in the case of the bladder, our challenge is **adaptability** to shape and intensity variabilities.

5.2 Contribution

We propose a fully automatic method for the coupled 3D localization and segmentation of the prostate and bladder in CT scans of the lower abdomen of male patients. A flexible approach on the bladder allows the process to easily adapt to high shape variation and to intensity inhomogeneities that would be hard to characterize (due, for example, to the level of contrast agent that is present). On the other hand, a statistical shape prior is enforced on the prostate.

We also propose an adaptive non–overlapping constraint that arbitrates the evolution of both structures based on the availability of strong image data at their common boundary. In the regions where the prostate–bladder interface is visible, we weight in favor of a more intensity–based model deformation. However, when the border is not clear, a shape prior introduced on the prostate helps define the "reasonable" frontier that we look for. In the case of non–homogenous bladders where the borders are visible only in certain regions, a "negotiation" of the intensity–based and the shape–based approaches takes place, arriving at a point of equilibrium that best balances both informations.

5.3 Outline

As with the bladder, our approach incorporates *non–rigid registration* based on surrounding bone structures to provide a reliable spatial initialization as well as a cropping step to reduce computation time.

The overall framework for the joint segmentation of the bladder and the prostate that we propose is as follows:

1. We assume that the images are already in a common frame of reference and cropped, following section 4.3. We also assume that the segmentation of the bladder has already been perfomed, following the steps described in chapter 4 up to the grayscale deformation stage, and that the resulting bladder model is therefore available.

2. As described in section 5.4, a starting point is found inside the prostate, and a 3D prostate model (simplex mesh) is initialized. The initial deformation of the prostate model is performed independently of the bladder model. The external force used to deform the mesh is the same as it is for homogenous bladders, using intensity information from the starting point inside the prostate. A shape prior is imposed during this deformation stage.

3. The simplex meshes corresponding to the bladder and the prostate are then simultaneously deformed using a context–dependent non–overlapping constraint, as described in section 5.5.

5.4   Prostate segmentation

In order to segment the prostate in CT scans, we rely on prior information (section 5.4.1) concerning its position (section 5.4.1.1), its shape (section 5.4.1.2), and its intensity (section 5.4.1.3). Once this information has been computed, it will serve to guide the deformation of an individual simplex mesh (section 5.4.2) to generate a first approximation of the organ. This approximation will then be refined and boundary conflicts with the bladder will be resolved through the joint deformation of the bladder and prostate models. A specially adapted assymmetric non–overlapping constraint has been desinged for this purpose and is described in section 5.5.

5.4.1   Prior Information

5.4.1.1   Prostate localization

We use prior information on prostate localization, which has been computed based on the expert's segmentations of the structure in our database images. These segmentations (as binary images) had previously been placed in a common frame of reference for bladder segmentation purposes using a non–rigid registration approach (see section 4.3.1).

5.4.1.2   Shape statistics

The shape of the prostate across large patient population shows statistical coherency [Rousson 2005a], and since the image data is often not sufficient to establish the outline of this structure, it is helpful to incorporate shape prior knowledge. We built a shape model of the prostate from a database of (registered) training samples (CT images and their corresponding segmentations of the prostate performed by an expert). An initial deformable model was used to fit (in a coarse to fine manner) the manual segmentations of the prostates in the database, thus assuring a reasonable point correspondence between the models. Its deformation is similar to that of the binary stage described in section 4.5.

We have modeled prostate shape variability in terms of *eigenmodes*. The method is based on a principal component analysis (PCA) of organ shapes and allows for the reduction of the large dimensionality of geometry information from multiple CT studies to a few–parametric statistical model of organ deformation.

Eigenmodes are 3D vector fields of correlated displacements of the organ surface points and can be seen as fundamental "modes" of the patients' prostate geometric variability. The amount of variability represented by the eigenmodes is quantified in terms of corresponding eigenvalues. Weighted sums of eigenmodes describe organ displacements/deformations and can be used to generate new organ geometries.

Parametrization of organ geometries   The prostate shape has been parametrized by the set of positions of M surface points: if $\vec{x}_j(i)$ denotes the position of the jth point in the ith prostate CT, then the surface shape vector
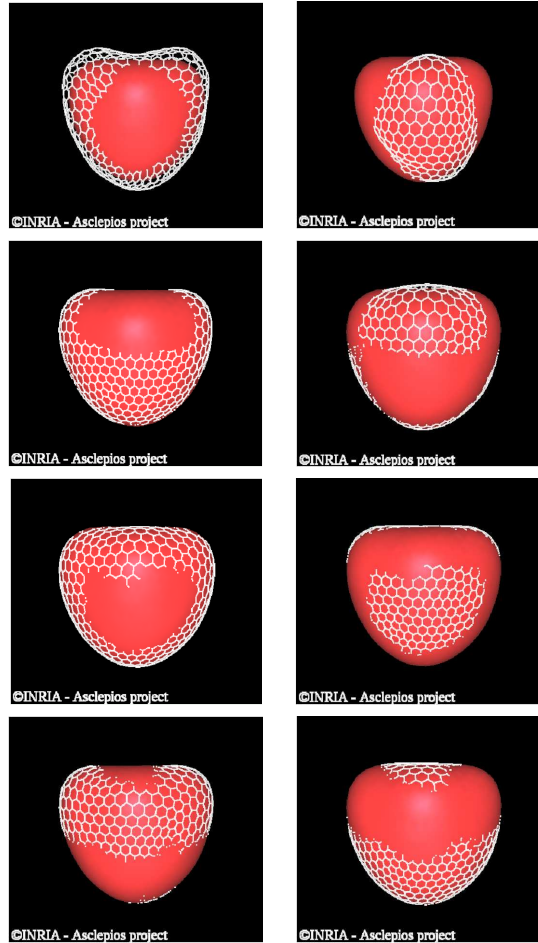
Figure 5.4: Influence of the first four computed eigenvalues (white wireframe) for the prostate mean model in the registered image space (shown in red). The left column shows the mean model minus 1 eigenvalue for each eigenvector, while the right column shows the mean plus 1 eigenvalue for each eigenvector.

$$b_i = (\vec{x}_1(i), ..., \vec{x}_M(i)) \in \mathrm{I\!R}^{3M} \tag{5.1}$$

represents the geometry of the organ in the ith CT ($i = 1, ..., N$).

It is important that each $\vec{x}_j$ in equation 5.1 corresponds to the same anatomical position in each of the N prostates, i.e., the series of **corresponding positions** $\vec{x}_j(1), \ . \ . \ . \ , \vec{x}_j(N)$ provides anatomical point–tracking information.

To this end, we have first put all the expert segmentations of the prostate in the registered–image space by applying to each segmentation (in the form of a binary image) the same registration transformation as the one applied to the original image. Once in the registered space, we have deformed the *same* initial mesh (a 3D sphere) to match each of the (registered) expert's segmentations of the prostate images, in order to assure a point correspondence. Their mean model μ_1 was subsequently computed and deformed to match once again the expert's segmentations of the prostates, to reduce eventual bias.

The fact that the registration transformation (computed using the locally–affine registration method described in section A) is **invertible** allows us to move from the non–registered image space to the registered space and back, with complete liberty.

Statistical Model of Organ Geometric Change Based on PCA   It is assumed that the set of surface shape vectors $\{b_i\}_{i=1,...,N}$ can be seen as samples from a random process. Obviously, for anatomical reasons, displacements of the M surface points due to organ motion and deformation are highly correlated, which implies that the underlying dimensionality of this multivariate statistical problem is actually much smaller than $3M$.

We are thus interested in correlated displacements of the surface points. For this $3M$-dimensional problem with N samples we use a method from multivariate statistics, **Principal Component Analysis** (e.g. [Manly 2004, Jolliffe 2002]). This type of approach is known as a **Point–Distribution Model** (PDM) in the literature[Cootes 1995a] and has been applied to problems like population modelling of anatomical shape variability[Lorenz 2000] or semi–automatic 3D organ segmentation[Pekar 2004].

Decomposition of organ geometry samples into eigenmodes Applied to the problem of organ geometric change, PCA works as follows. The first two moments of the probability distribution, i.e. the **mean shape vector** $\bar{b} \in \mathrm{I\!R}^{3M}$ and the centered **covariance matrix** $C \in \mathrm{I\!R}^{3M} \times \mathrm{I\!R}^{3M}$, are calculated according to equations 5.2 and 5.3.

$$\bar{b} \;=\; \frac{1}{N} \sum_{i=1}^{N} b_i \tag{5.2}$$

$$
\begin{aligned}
C &= \frac{1}{N-1} \sum_{i=1}^{N} (b_i - \bar{b}).(b_i - \bar{b})^T \\
&= \frac{1}{N-1} BB^T
\end{aligned}
\tag{5.3}
$$

Here the column vector $(b_i - \bar{b})$ describes the displacements of the geometry at time t_i relative to the the mean shape, and $().()^T$ denotes the outer product of these two $3M$–dimensional vectors. Forming a matrix $B \in \mathbb{R}^{3MN}$ from the N centered shape vectors, the covariance matrix can be rewritten to the compact form on the second line of equation 5.3.

In case the probability distribution which governs the assumed random process is a multivariate normal distribution, it is already uniquely characterized by these first two moments. For the problem of internal organ motion/deformation considered here, the exact type of probability distribution is unknown a priori. However, considering only the first two moments can still serve as an approximation, where the covariance matrix represents the organ geometric variability.

Correlations of the $3M$ variables are reflected by the existence of nonzero off–diagonal elements of the covariance matrix, implying that the probability distributions of the variables are not independent. Diagonalization of the covariance matrix results in **eigenvectors** $q_l \in \mathbb{R}^{3M}$, which represent statistically independent modes of deformation, the so–called **eigenmodes**. Under the assumption of a multivariate Gaussian distribution these eigenmodes approximately describe the deformation characteristics. Each eigenmode defines a 3D vectorfield of correlated displacements $\delta \vec{x}_j \in \mathbb{R}^3$ for the M surface points: $q_l = (\delta \vec{x}_{1,l}, ..., \delta \vec{x}_{M,l})$.

$$
\sigma_l^2 = \lambda_l
\tag{5.4}
$$

The eigenvectors give a new basis of the $3M$–dimensional parameter space, in which the assumed multivariate normal distribution decomposes into 1D Gaussian distributions along the directions of the eigenvectors. Quantitatively each eigenvalue λ_l is the statistical variance of the N measured geometry samples projected on the lth eigenvector as new basis vector 5.4.

Implementation issues The size of the resulting covariance matrix can be a prohibitive issue in terms of computation time when it comes to its diagonalization. An interesting solution to this problem has been proposed in [Cootes 1995b], in which the a smaller matrix is diagonalized instead, and a relationship is found between the eigenvalues and eigenvectors of the smaller matrix to those of the initial covariance matrix.

Construction of organ geometries using eigenmodes The eigenvalues impose an importance ranking on the eigenmodes with respect to the representation of geometric variability. The dominant eigenmodes, i.e., the eigenmodes with largest eigenvalues, are the "principal" deformation modes, which span the space in which

Mode	Eigenvalue
1	693.10
2	524.17
3	382.36
4	275.63
5	201.73
6	171.68
7	134.15
8	123.74
9	113.01
10	94.14
11	84.07
12	73.33
13	67.70
14	50.49
15	47.87

Figure 5.5: Eigenvalues corresponding to the first 15 computed eigenvectors for prostate shape variations (based on 24 expert segmentations). For our purposes, only the first 8 eigenvectors were taken into account, wich represent 82.3 % of the total sum of the eigenvalues.

the majority of deformations occur. New geometry samples can be generated by deforming the mean shape by a weighted sum of L dominating eigenmodes.

$$\bar{b} = \bar{b} + \sum_{l=1}^{L} c_l q_l \qquad ||q_l|| = 1 \tag{5.5}$$

According to the theory of PCA, the coefficients $c_l \in \mathbb{R}$ obey Gaussian distributions with the corresponding eigenvalues as variances (equation 5.5). Thus the dominating eigenmodes can serve as statistical model of individual organ motion/deformation with only a small number of parameters.

We applied the method to our patient dataset of prostate segmentations to assess the shape variation. The spectrum of eigenvalues was found to be dominated by only few values (8), indicating that the geometric variability of the prostate is governed by only few patient specific eigenmodes. Some of them are illustrated in figure 5.5. However, prostate shapes in new images may not be included in the space spanned by the chosen eigenvectors, so additional criteria has been added in the deformation process to add expressiveness to the deformable model.

5.4.1.3   Intensity information

We obtain initial information about the intensity of the prostate in each registered image from a small region inside the target structure. We define this region around a starting point located inside the mean shape model. We choose, among all the potential starting points, one located in a neighbourhood showing little intensity variance (i.e., lower than a certain threshold) within a previously computed interval.

5.4.2 Initial prostate model deformation

Since the deformation field for the prostate has been studied and a mean model has been computed (section 5.4.1.2), it is natural to use that mean shape model as the initial mesh for the segmentation process.

At each time step t, the position of vertex V_i in the prostate model is computed according to equation 5.6.

$$V_i^{t+1} = V_i^t + \lambda(\alpha(f_i^{PCA}) + \delta(f_i^{int}) + \beta(f_i^{ext})) + (1 - \lambda)(f_i^{global}) \qquad (5.6)$$

This evolution formula is similar to the one for the bladder, except for the added influence of f^{PCA}, the PCA–based regularization force. The value of its weight, α, has been empirically set to 0.4.

5.4.2.1 Shape prior force f_{PCA}

The force f^{PCA} pulls the current model $\mathcal{S}$ towards $\mathcal{S}_\mathrm{S}$, a "smooth" surface that belongs to the space spanned by the computed PCA modes of variation (for regularization purposes) and f^{ext} pulls it towards $\mathcal{S}_\mathrm{I}$, an estimated target surface corresponding to the boundaries of the anatomical structure in the image.

This force is applied every 5 model evolution steps, as follows:

1. The current mesh S_i^t is registered (similarity), by distance minimization vertex by vertex, with respect to the mean PCA model S_μ.

2. The displacement with respect to S_μ in the registered space is computed and projected onto the PCA space. This projection is then added to the mean model, resulting in $P_{PCA}(S_i^t)$, the projected current model.

3. $P_{PCA}(S_i^t)$ is registered with respect to S_i^t, yielding S_i^{PCA} (as opposed to applying the inverse registration transformation on the projected model, which would yield unstable results).

These steps are illustrated in figure 5.6.

Why not apply, at the third point, the inverse registration transformation that was computed in point 1? The main concern with a PCA–driven force is that given a shape, there is no guarantee that either the center of mass of the mesh (i.e. the average of all mesh points) or the global mesh size will be preserved after the PCA projection. If there exists a bias on position or size and this bias remains the same throughout the iterations, it could have an important influence on the resulting mesh: it may grow too much, or simply move, which would make the segmentation process unstable.

That is the reason behind our choice, at point 3, of re–registering the projected result on the mesh before projection instead of applying the inverse of the first registration transformation to it.

This deformation process is iterated until the model stabilizes (i.e., the deformation at each iteration becomes small enough to be neglectable). It is then time
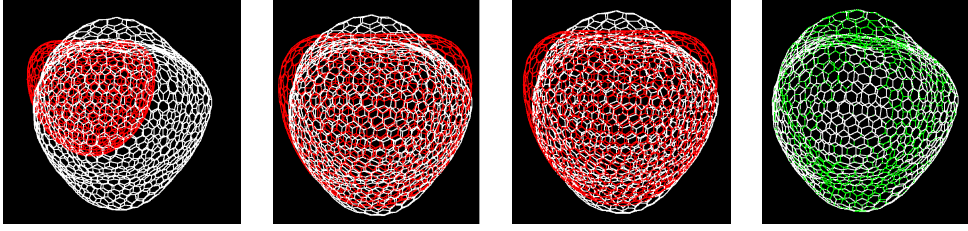
Figure 5.6: Application of the shape constraint to the model at time t (white) (the mean PCA shape is shown in red, left). The model is first registered (similarity) to the mean PCA model (center–left). Then, their difference is computed, projected onto the PCA space, and added to the mean model (center–right). The result is affinely registered with respect to the model at time t (shown now in green, right).

to bring the prostate–bladder model interaction to resolve eventual common border conflicts or overlaps.

5.5   Context–Dependent Coupled Deformation

We present a coupled segmentation framework in which an asymmetric, non–overlapping constraint is enforced. The non–overlapping of the structure models is achieved through the use of a specifically designed force to each mesh in the coupled deformation process. At each deformation step, the areas enclosed by both the prostate and bladder models are checked for intersection. If such an intersection exists, a new elastic force, proportional to the distance maps to the meshes, is added to both models in order to drive them appart (see figure 5.7).

If the prostate–bladder interface is sufficiently defined (as in the case of contrasted bladders), we apply a symmetric non–overlapping force to both models. If, on the other hand, the interface is blurry, a higher priority is given to the model that contains the most information (such as a shape prior), which is, in our case, the prostate mesh.

Our proposed asymmetric, context dependent non–overlapping constraint comprises interaction forces between the prostate and bladder meshes (F_{PoB}, or the force of the prostate on the bladder, and F_{BoP}). To this end, the prostate shape model P, the bladder model B and the strength of the border between the two in the image ($f(||\bigtriangledown I||)$) are taken into account, as shown by equations 5.7 and 5.8.

$$F_{BoP} = -\eta_P * ((\bigtriangledown Dmap_B)/|| \bigtriangledown Dmap_B||) * (Dmap_B - \tau_B) * f(||\bigtriangledown I||) \quad (5.7)$$

$$F_{PoB} = -\eta_B * ((\bigtriangledown Dmap_P)/|| \bigtriangledown Dmap_P||) * (Dmap_P - \tau_P) * (1 - f(||\bigtriangledown I||)) \quad (5.8)$$

where
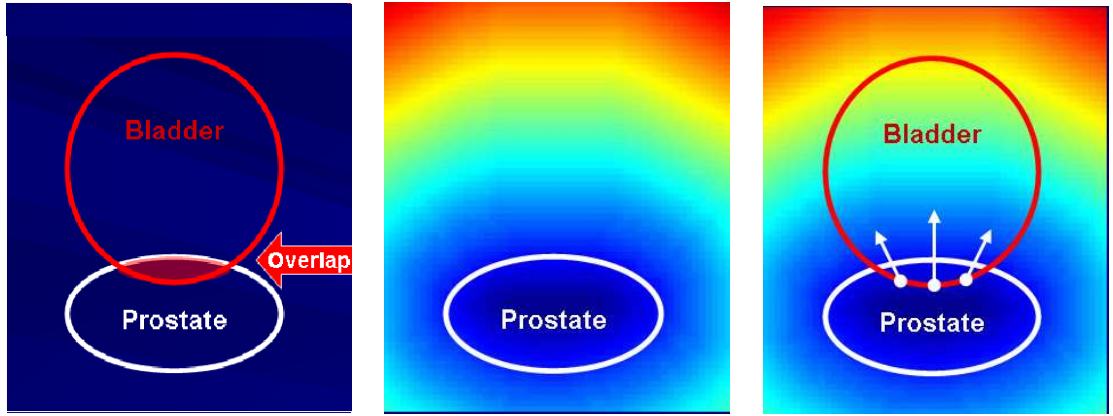
Figure 5.7: Computation of the non–overlapping force for the bladder. If an overlap exists, forces are applied on the bladder and prostate meshes to separate them. In the case of the bladder, the force is applied in the direction of the gradient of the distance map to the prostate. Similarly, in the case of the prostate, the force is based on a distance map to the bladder.
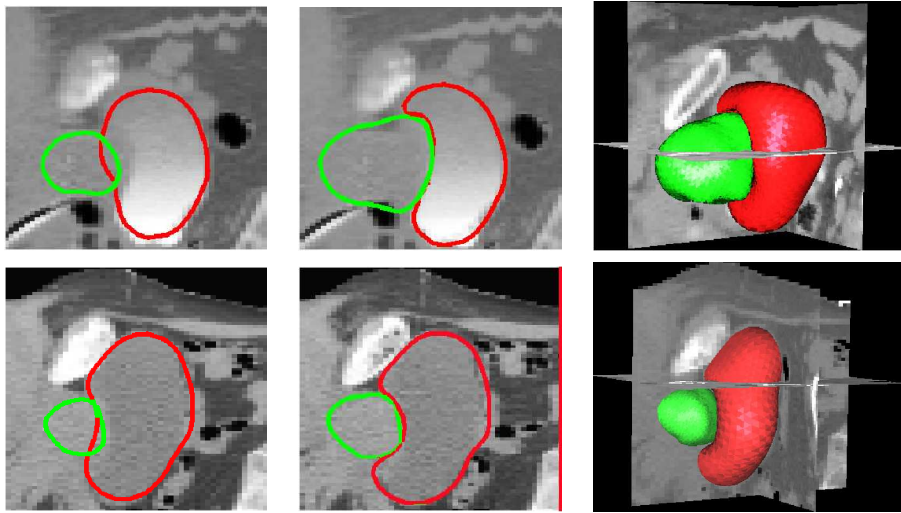
Figure 5.8: Examples of the effect of the non–overlapping constraint in both partially clear (first row) and fuzzy (second row) prostate–bladder interfaces. From left to right, the independent evolution of prostate and bladder models, their coupled evolution with our non–overlapping constraint, and a 3D view of the result.

$$f(|| \nabla I||) = \begin{cases} \frac{||\nabla I||}{\vartheta}, & if || \nabla I|| \le \vartheta \text{ (i.e., zone with low contrast)} \\ 1, & if || \nabla I|| > \vartheta \text{ (i.e., zone with high contrast)} \end{cases}$$

Parameters η_P and η_B weight the strength of the repulsion force, $Dmap_B$ and $Dmap_P$ are the distance maps to the bladder and prostate models, respectively, τ_B and τ_P are thresholds chosen on the distance maps (to establish a minimum distance between the models, if desired), $|| \nabla I||$ is the norm of the image gradient, and ϑ is a threshold on the image gradient value to distinguish contrasted from non–contrasted prostate–bladder interfaces.

In case of model overlap on a contrasted zone, priority is given to the bladder (since the prostate, not showing any contrast agent, must have "invaded" the bladder in the image). It is then the bladder model that pushes the prostate model, and the force F_{PoB} is eliminated by setting the value of $f(|| \nabla I||)$ to 1.

However, when an overlap occurs in a non–contrasted zone, there is no intensity information to privilege one model over the other. Therefore, both models push each other away.

5.6   Results and Analysis

The automatic segmentation algorithm was applied to a database of 16 CT images of the lower abdomen of male patients (see also [Costa 2007a]). The results were compared to experts' segmentations of bladder and prostate (the manual segmentation sets used for training and validation are disjoint). Figure 5.9 shows the obtained sensitivities and positive predictive values: the average sensitivity / positive predictive value is 0.81 / 0.85 for the bladder, and 0.75 / 0.80 for the prostate.

For the validation of the prostate segmentations, we were able to assess the inter–expert variability thanks to a database of 5 CT images in which the prostates had been segmented by 3 different experts. We used the STAPLE [Warfield 2004] algorithm to compute a mean expert segmentation, and compared both the manual (expert) and automatic segmentations with respect to this mean. Further details about this algorithm can be found in B. The results (Figure 5.10) show that the automatic segmentations are not far from the ones performed by the experts. The sensitivity values are somewhat higher than the positive predictive values in the automatic case, indicating a slight over–segmentation of the structure.

The first case in table 5.10 is illustrated in figure 5.11. The automatic prostate segmentation is shown in red, and the manual segmentations performed by the first, second and third experts are shown in magenta, green and blue, respectively. The figure shows the slight over–segmentation of the automatic method detected in figure 5.10, mostly towards the feet of the patient.

Some resulting segmentations for the bladder and prostate are illustrated in figure 5.12. The results are promising, in spite of the low saliency (sometimes even indistinguishability) of the prostate in the images. The bladder–prostate interface

Image	Bladder Sensit.	Bladder PPV	Prostate Sensit.	Prostate PPV
1	0.82	0.94	0.73	0.99
2	0.87	0.95	0.86	0.92
3	0.88	0.94	0.75	0.91
4	0.86	0.89	0.95	0.72
5	0.89	0.97	0.72	0.81
6	0.86	0.86	0.79	0.81
7	0.91	0.96	0.86	0.87
8	0.87	0.85	0.82	0.94
9	0.87	0.93	0.76	0.84
10	0.88	0.84	0.85	0.84
11	0.91	0.93	0.80	0.89
12	0.82	0.77	0.72	0.89
13	0.69	0.92	0.79	0.64
14	0.82	0.79	0.89	0.82
15	0.94	0.97	0.79	0.90
16	0.85	0.97	0.74	0.77
Mean	0.86	0.90	0.80	0.85
Std. Dev	0.05	0.06	0.06	0.08
Min	0.69	0.77	0.72	0.72
Max	0.94	0.97	0.95	0.99

Figure 5.9: Sensitivity and Positive Predictive Value results of the automatic segmentation of the bladder (left) and prostate (right) with respect to the one performed by an expert. The respective mean, standard deviation, minimum and maximum values are also indicated.

Image	Expert 1 Sensit.	Expert 1 PPV	Expert 2 Sensit.	Expert 2 PPV	Expert 3 Sensit.	Expert 3 PPV	Automatic Sensit.	Automatic PPV
1	0.82	0.87	0.98	0.80	0.94	0.91	0.98	0.71
5	0.80	0.99	0.99	0.64	0.90	0.96	0.85	0.72
6	0.82	0.89	0.96	0.75	0.99	0.97	0.81	0.81
9	0.92	0.95	0.98	0.69	0.77	0.98	0.92	0.66
10	0.91	0.91	0.96	0.96	0.97	0.84	0.79	0.89
Mean	0.85	0.92	0.97	0.77	0.91	0.93	0.87	0.76
Std. Dev.	0.05	0.04	0.01	0.12	0.08	0.05	0.07	0.09
Min	0.80	0.87	0.96	0.64	0.77	0.84	0.79	0.66
Max	0.92	0.99	0.99	0.96	0.99	0.98	0.98	0.89

Figure 5.10: Sensitivity and Positive Predictive Value of both the expert and automatic segmentations of the prostate, with respect to the computed mean expert segmentation using the STAPLE [Warfield 2004] algorithm. Mean, standard deviation, minimum and maximum values are also indicated.
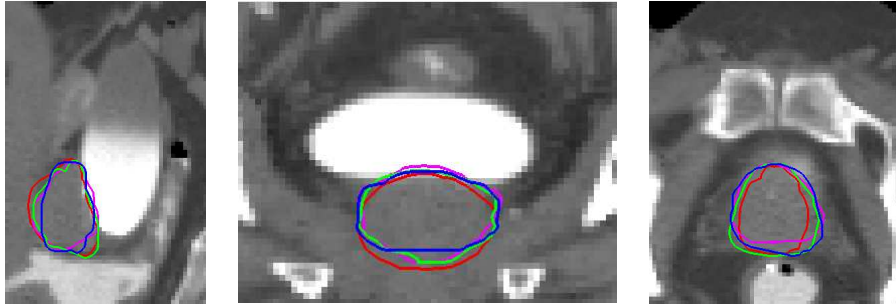
Figure 5.11: Automatic and manual segmentations of the prostate, corresponding to the first case in image 5.10. The automatic delineation is shown in red, while that of the 3 experts are shown in magenta, green and blue. From left to right, sagittal, coronal and axial views.

is correctly found. As the experts have confirmed, the prostate border that is not shared with the bladder is difficult to delineate, since there is little or no image information in this zone. This introduces some variability in the figures.

Figure 5.13 shows the resulting segmentations for entry 13 in table 5.9. A fuzzy prostate–bladder interface and the absence of clear delimitations towards the lower border of the prostate (left hand side in the sagittal slice) are at the source of the differences with the manual expert segmentation.

In the next chapter, we include the rectum in the joint segmentation process, since it is also an organ at risk during prostate cancer radiotherapy.
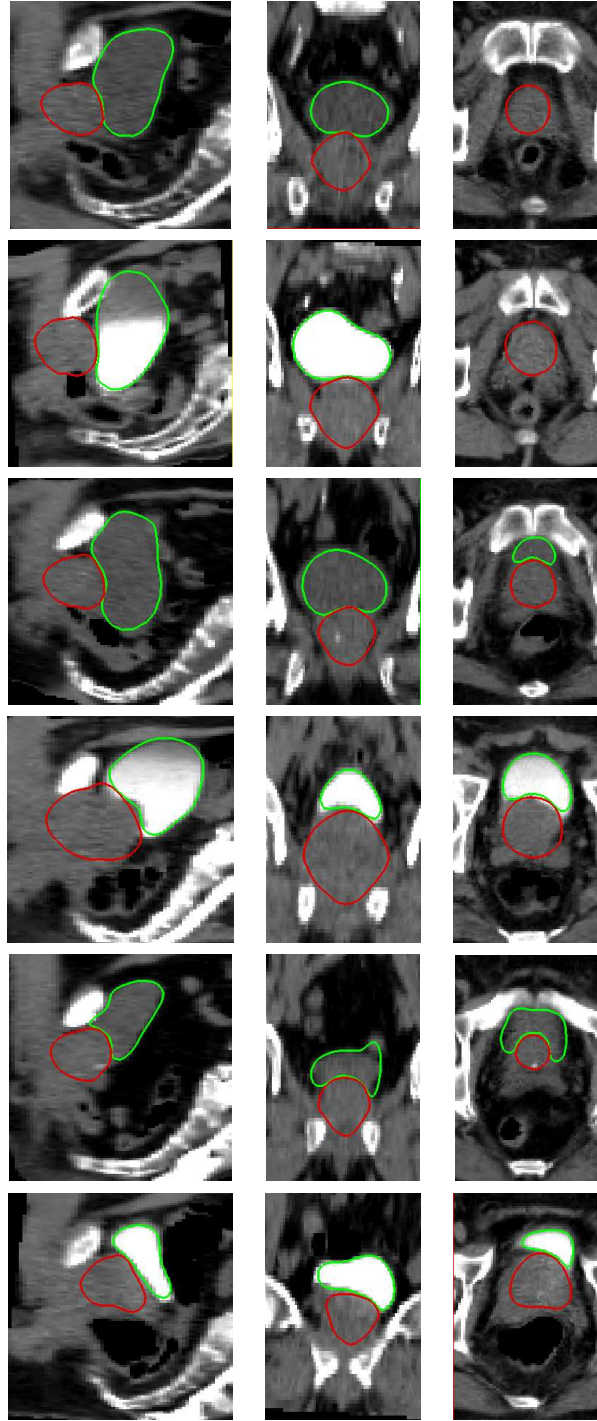
Figure 5.12: Automatic segmentation results for bladder (green contour) and prostate (red contour) for entries 4, 7, 11, 12, 14 and 15 in table 5.9. From left to right, sagittal, coronal and axial views.
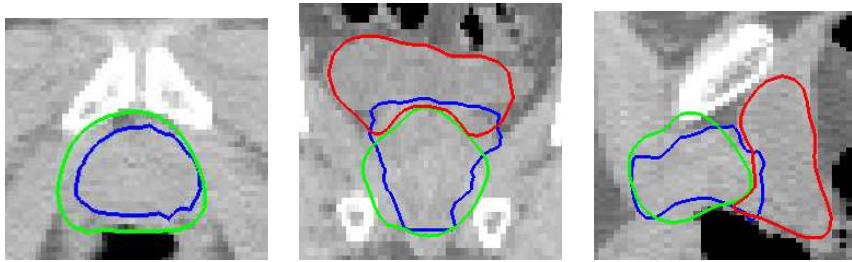
Figure 5.13: Automatic segmentation results for bladder (red contour) and prostate (green contour) for the worst case encoutered (entry 13 in table 5.9). From left to right, sagittal, coronal and axial views. The blue contour shows the segmentation performed by an expert.

CHAPTER 6

Rectum Segmentation and Integration

Contents

6.1 Challenges in rectum segmentation

With the advent of conformal radiotherapy for prostate cancer it is possible to deliver higher doses than in the past while maintaining an acceptably low rate of moderate/severe late side effects. However, when trying to escalate the tumour dose, an increased risk of treatment–related toxicity can be expected, rectal bleeding being one of the major limiting factors.

When applying dose restrictions to the rectum, contouring becomes a significant factor that determines the risk of rectal toxicity. The results of recent studies [Fiorino 2002, Boehmer 2006, Guckenberger 2006] show that different ways of rectal contouring significantly influence doses to the rectum. Therefore, an accurate
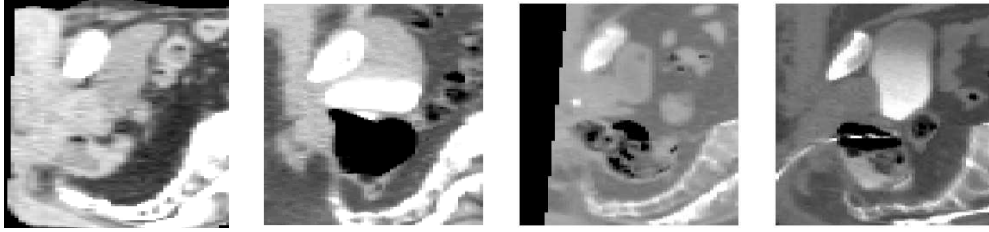
Figure 6.1: Different rectum fillings. From left to right, empty, non–contrasted rectum, air insufflated rectum, mixed fillings rectum and presence of a probe.

segmentation of the rectum's outer wall is key to an adapted radiotherapy dose planning for the prostate with as little rectal toxicity as possible.

As has been pointed out in the cited work (chapter 3), most approaches to rectum segmentation rely on a certain number of assumptions concerning shape and intensity within the structure in the images. Such hypotheses are usually plausible in CT scan databases in which the prior patient preparation (air insufflation, contrast agent, etc.) is the same.

However, in our case, our database is composed of CT images that come from various centers, and whose acquisition has been made under significantly different protocols. The variability in the fillings of the rectum images in our database can be appreciated in figure 6.1. They include completely empty, non–contrasted structures (left), air–insufflated cases (center–left), mixed fillings (center–right) and mixed fillings with a probe (right). The changes in structure shape, size and intensity values are difficult to characterize, and make the task of automatic rectum segmentation <u>very</u> challenging. These challenges are, once more, centered around *adaptability* to shape and intensity variabilities of the structures.

6.2   Rectum Delineation Endpoints

Several definitions for the start and end points for rectum delineation have been proposed. We choose the one adopted in recent literature [Akimoto 2004, Peeters 2006], in which the rectum is delineated from the end of the anal canal to the point at which it turns into the sigmoid colon (figure 6.2).

A rule of thumb would be that the rectum ends when there is a strong change in direction (i.e., when there is a point of high curvature, where it becomes either the anal canal or the sigmoid). Some manual expert segmentations are shown for illustrative purposes in figure 6.3.

6.3   Contribution

We propose a fully automatic method for the 3D localization and segmentation of the rectum in CT scans of the lower abdomen of male patients. Our approach performs an initial isolation of the rectum structure, based on prior information concerning its
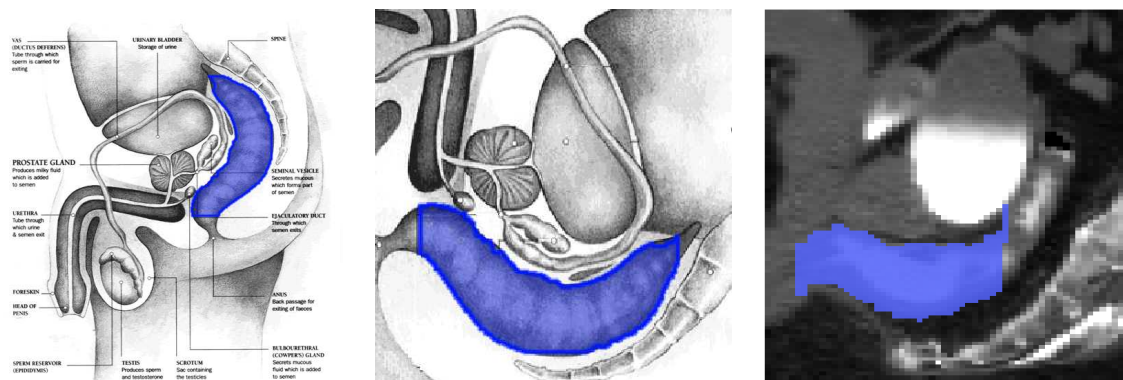
Figure 6.2: Anatomy of the rectum. From left to right, the rectum of a standing patient, the same shown in the lying position, and a real CT example of an expert's rectum delineation, all in blue (sagittal views).
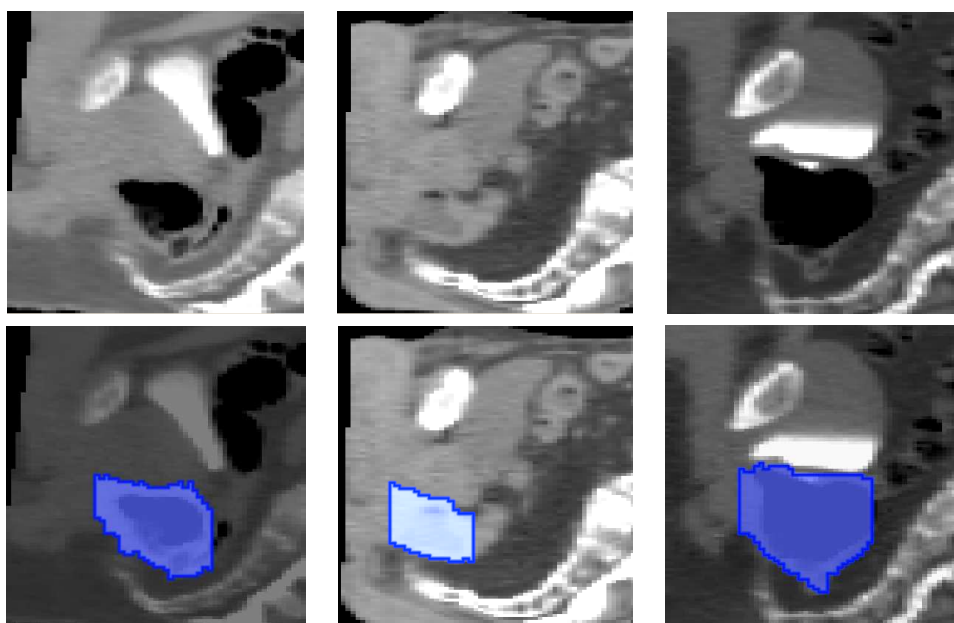
Figure 6.3: Expert segmentations of different rectums. Top row: original (registered and cropped) images. Bottom row: the same images, with the manual rectum segmentations outlined in blue (sagittal views).

surrounding organs (bladder, prostate, bone structures). Then, a deformable skeleton is applied, based on a distance map computed from the resulting image, in order to have a better initialization of the rectum's global position. Around this skeleton, a 3D simplex mesh is constructed and then deformed in such a way that not only segmentation is achieved, but the remaining neighboring organs (seminal vesicles) are also avoided. A novel tubular constraint is applied on the mesh throughout the deformation process.

Since no assumptions about the rectum's fillings are made, the method easily adapts to shape variations and intensity inhomogeneities that would be hardly characterizable, such as those introduced by air, residues, contrast agent, probes, etc. This process is detailed in the following sections.

6.4   Outline

As can be seen in figure 6.2, the structures that are potentially connected to the rectum in the images and/or have similar intensities, therefore most likely to mislead the deformable model of the rectum are:

- Pubic bone structures.

- Bladder.

- Prostate.

- Surrounding fat tissue.

- Seminal vesicles.

These structures are either **progressively eliminated** (section 6.5), or carefully avoided. An image of the rectum (as isolated as possible) is generated, and a **centerline** for the structure is then computed and deformed on this image, as explained in section 6.6. This deformed centerline is later used within the deformation of a 3D model (simplex mesh) whose goal is to contour the rectum. Surrounding, potentially misleading organs that may have been left in the image, such as the seminal vesicles, are avoided by imposing a **tubular constraint** on the simplex mesh (section 6.7).

6.5   Substraction stage

6.5.1   Pubic bone structures

In order to eliminate the pubic bone structures, we rely on the same multi–affine registration that has already been performed on the images (see Section 4.3). This registration process is based on regions defined around the pelvic bone structures;
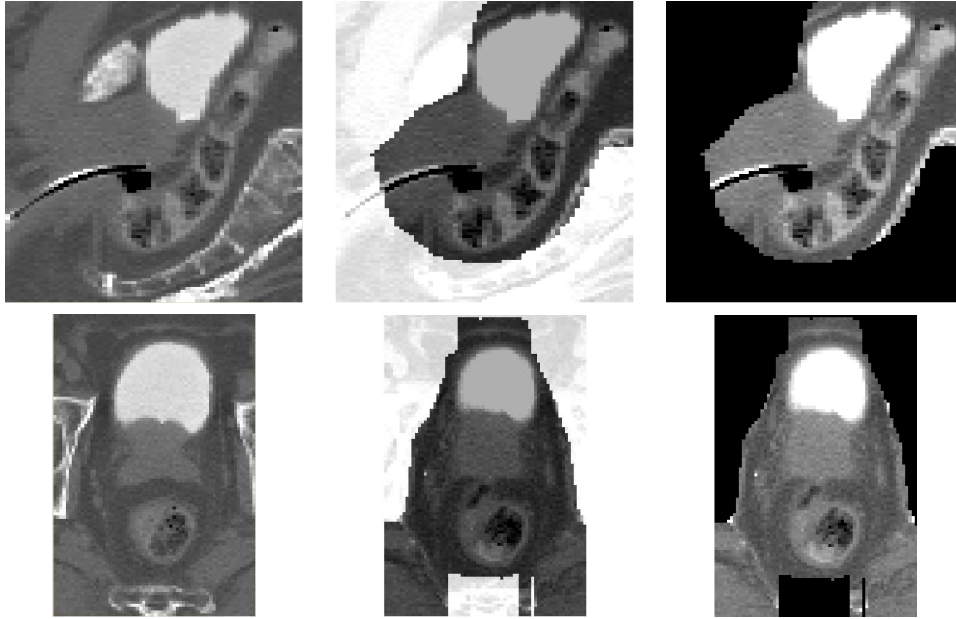
Figure 6.4: An example image to which a mask is applied to eliminate the surrounding bone structures. From left to right, original image, mask, fusion of the image and the mask, and the resulting image once the masked bones have been eliminated. First row, sagittal views, and second row, axial views.

the registered images have, thus, a consistent bone position. A binary mask corresponding to these bones suffices to eliminate them from the images (set them to intensity value 0).

An example of an original image, the binary mask and the resulting image can be seen in figure 6.4.

6.5.2 Bladder and Prostate

The automatic segmentations of the bladder and the prostate performed as described in chapters 4 and 5 serve to create binary masks that correspond to those structures. These masks are used to "erase" these structures from the image (i.e., set their intensities to 0) .

To continue with the example in figure 6.4, the segmented bladder and prostate are shown, as well as the resulting image once these structures have been eliminated, in figure 6.5.

6.5.3 Surrounding fat tissue

Surrounding fat tissue is effectively eliminated by means of mathematical morphology operations (threshold with a fixed threshold interval of (-200, -10) H.U.).

Resulting images are exemplified in figure 6.6.
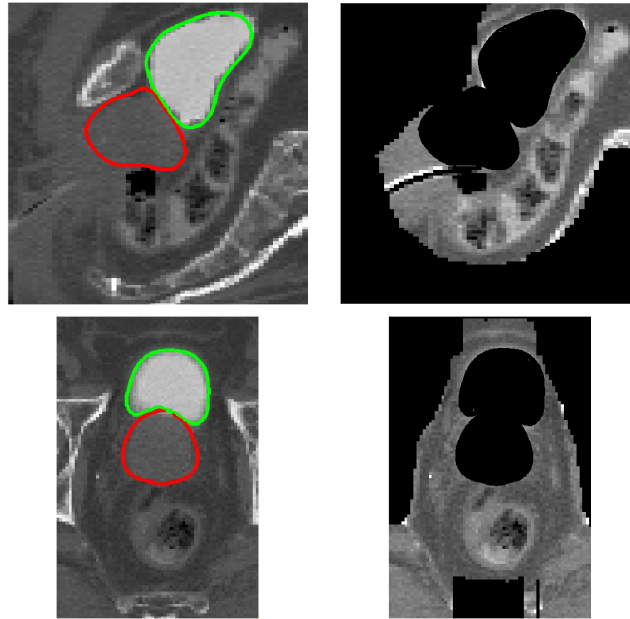
Figure 6.5: Example image and the corresponding segmentations of the bladder (green) and prostate (red) shown in the left column. To the right, the same image from which the bladder and prostate have been eliminated. In the first row, sagittal views, and in second row, axial views.
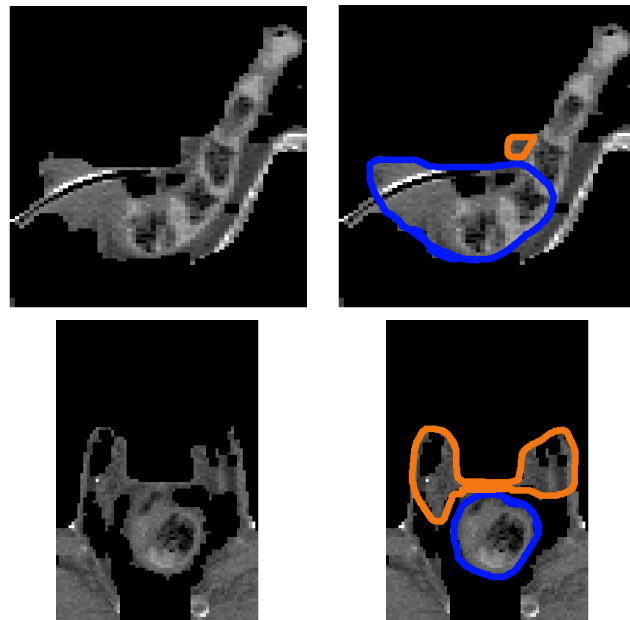
Figure 6.6: The resulting image once the fat tissues surrounding the structures have been eliminated. The rectum can be seen outlined in blue, and the seminal vesicles in orange. Top row, sagittal views, and bottom row, axial views.

6.5.4   Seminal Vesicles

As can be seen in figure 6.6, the seminal vesicles are still left in the image, and must be avoided from the rectum segmentation. To this end, we rely on a tubular constraint imposed on a deformable model, as described in the Section 6.7.3.

6.6   Centerline alignment

At this stage of the process, we have a certain knowledge about where the rectum is **not**, but we still don't know how to precisely contour its boundaries.

6.6.1   Building an initial rectum mesh

All the expert segmentations of the rectums (in the form of binary images) that we have in our database are based on images that are already in a common frame on reference as mentioned in section 6.5.1. These binary images are accummulated into one, in order to build an a–priori probability map for each voxel of belonging to the rectum. The result of this process can be seen in figure 6.7.

We create a template mesh to serve as initialization for the model deformation stage by thresholding this probability map by 80%, and then deforming a spherical simplex mesh to fit this binary image (figures 6.7 and 6.8).

However, this initial mesh would be unable to accommodate the large variability of the rectum's shape (global positionning, size and shape due to different fillings) on its own. We rely on the computation of the rectum's centerline in order to better position this mesh before beginning its deformation, as detailed in the next subsection.

6.6.2   Deforming a template skeleton

The deformable skeleton, which corresponds to the computed centerline of the initial rectum's mesh, is a line of vertices, one per Z slice, whose positions lie in the (x,y) plane. Since the z coordinate of each vertex remains fixed, the likelihood of having a stable structure is greater. This structure will evolve much like a traditional model, driven by both data–driven and regularization forces, to better fit the centerline of the real rectum in the underlying image. Once its evolution is finished, the centerline of the initial rectum model will be adjusted to this skeleton, resulting in an improved position initialization.

Data driven forces   The input data is a binary image whose background (i.e. voxels with value 0) corresponds to the structures that are considered as not belonging to the rectum (as described in section 6.5). A Chamfer distance map to this background region is computed. The image voxel in each z slice whose distance value to this background is greatest (i.e., the points most likely to belong to the "skeleton" of the rectum in the image) will attract the corresponding deformable template skeleton vertex. Hence, at each iteration, the deformable skeleton will be
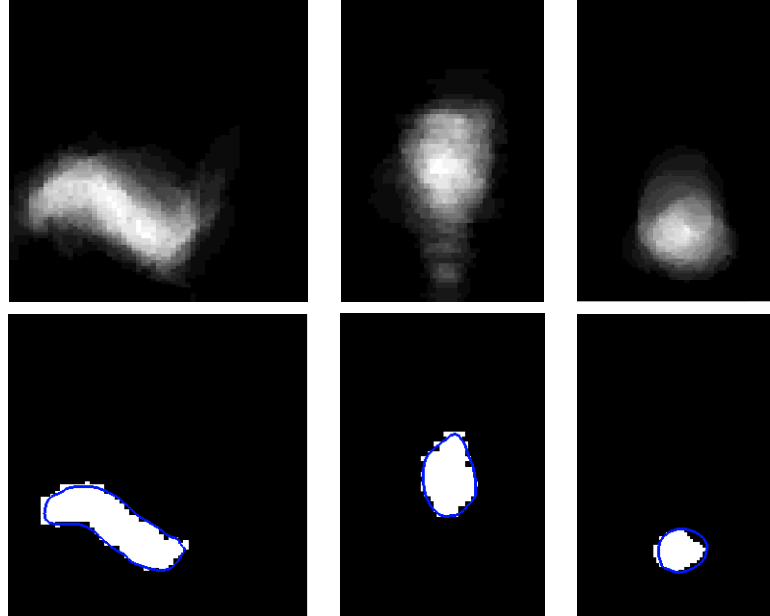
Figure 6.7: An image of all the registered expert rectum segmentations superimposed, which originate a probability map for the rectum's position (top row). A binary image of the initial rectum model is then obtained by thresholding this map (bottom row, with the resulting mesh superimposed). From left to right, sagittal, coronal and axial views.
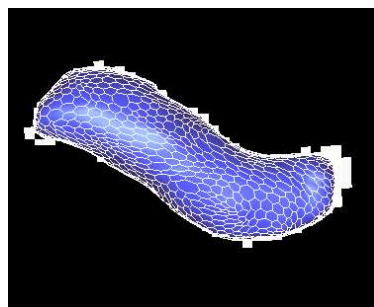
Figure 6.8: 3D view of the initial rectum simplex mesh.
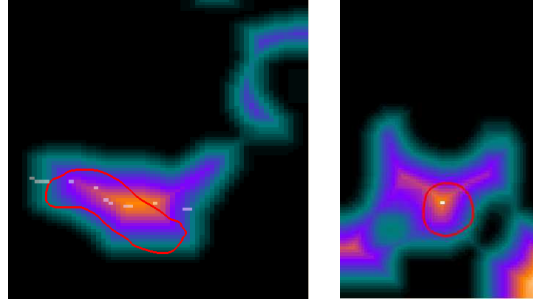
Figure 6.9: Chamfer distance to the outside, i.e., non–rectum portion of the image. The centerline of the initial rectum mesh (shown in red) will constitute a skeleton that will be attracted to the points with highest distance value (shown in white). From left to right, sagittal and axial views.
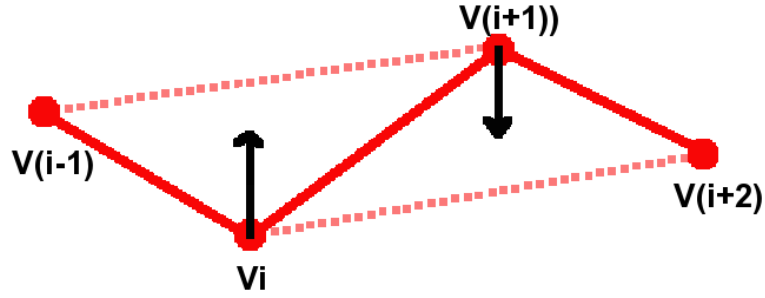
Figure 6.10: Internal (regularization) forces for the deformable skeleton. Each vertex is moved so as to minimize the first derivative of the position of its two neighbors.

pulled towards the potential center of the image's rectum in each z slice. This is illustrated in figure 6.9.

Regularization forces   The regularization force C0 seeks to minimize the first square derivative of the skeleton; that is, it will pull each mesh vertex half way towards the middle of its two neighbours (see figure 6.10). At the first and last vertices, a similar force is computed using the previous two points. Notice that this can be done multiple times, increasing the regularization process.

A few iterations of the whole process (data–driven forces + regularization forces) are sufficient since, due to the very limited number of skeleton vertices, the skeleton's deformation process is very fast, and the result constitutes a good initialization.

In order to adapt the initial rectum model so that it fits around this skeleton, the center of each axial slice in the initial mesh is computed. To this end, the model is rasterized into a binary image, a Chamfer distance map is computed to the "outside" (i.e., the background) of the resulting structure, and the center points are chosen as the points of greatest distance value for each z slice. The initial model is
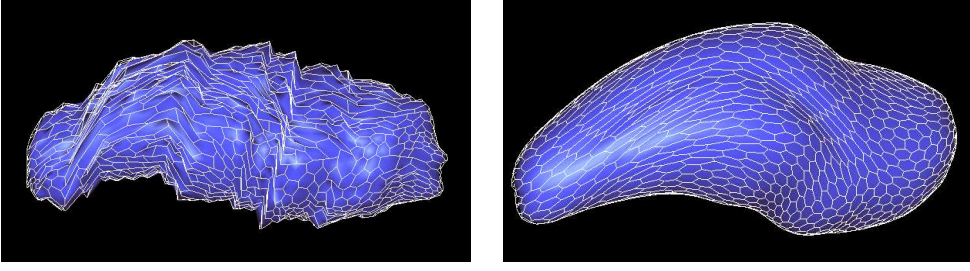
Figure 6.11: Regularization applied to the initial translated mesh, based on the deformable skeleton.

then translated so that each of the computed center points fits the corresponding vertex of the target skeleton. Since this translation may yield irregular results, a few regularization steps are run on the translated mesh to ensure a smooth initialization.

For this regularization, parameters α and λ are set to 1, a C1 regularization is applied, and the others terms are eliminated by setting the other parameters to 0 in the evolution equation 4.2. A sample result may be seen in figure 6.11.

6.7   Mesh deformation stage

The model obtained in the previous section undergoes a similar deformation process to that of the prostate mesh. However, in this case, the shape constraint is replaced by a new **tubular constraint**. At time step t, the position of vertex V_i in the rectum model is computed according to Equation 6.1.

$$V_i^{t+1} = V_i^t + \lambda(\alpha(f_i^{tube}) + \beta(f_i^{ext}) + \delta(f_i^{int})) + (1 - \lambda)(f_i^{global}) \qquad (6.1)$$

where V_i^t and V_i^{t+1} are the positions of vertex i at time t and $t+1$, respectively. As with the prostate, parameter λ is a **locality** parameter that varies throughout the deformation from $\lambda = 0$ (a purely global deformation) to $0 < \lambda < 1$, more localized deformations. The influences of f^{tube} (the tube constraint force), f^{ext} (an image force that pulls towards high gradient value points) and f^{int} (internal regularization force) are weighted by parameters α, β and δ, respectively.

Further details are given in the following sections.

6.7.1   Internal Forces

The chosen regularization force, C1, seeks to regularize the curvature at each vertex with respect to its neighbours, using the simplex angle, as described in 4.5.2.

6.7.2   External Forces

The image on which the external forces for the rectum model are based is the result of the elimination of the rectum's surrounding organs from the original image (i.e.,

their intensities set to 0), as has been described in section 6.5. An external force that follows the gradient of this image is applied during the model deformation stage in this case.

At each time step t, the current model $\mathcal{S}(\mathbf{u})$ (which is already well positioned, following section 6.6.2) is pulled towards a nearby surface $S_{ext}(\mathbf{u})$ that best interpolates points in the image that are close and whose gradient value is high, as can be seen in equations 6.2 and 6.3.

$$S_{ext}(\mathbf{u}) = \mathcal{S}(\mathbf{u}) + s * \vec{n} \tag{6.2}$$

where

$$s = \arg\max_{v} || \bigtriangledown \mathcal{I}(\mathcal{S}(\mathbf{u}) + v * \vec{n})|| \tag{6.3}$$

6.7.3 Tubular constraint

The rectum being a tube–like structure, we constrain its evolution by pulling the 3D model, with more or less strength, towards a nearby tubular shape. This is achieved by computing, at each iteration, tubular surface S_{tube} and by pulling the mesh towards it with a strength given by a **tube constraint weight**.

A simple, tempting way to compute S_{tube} would be in a 2D fashion, as follows: the current model's center at each z slice is computed as the average position of the vertices whose z coordinates are closest to the given z value. The biggest possible ellipse is then fit inside the model for that slice, and the current mesh is then pulled towards this ellipse.

However, although simple to implement, continuity cannot be assured between contiguous slices with this constraint, as far as the sizes of the 2D ellipses are concerned. Indeed, since the constraint is two–dimensional, irregularities often arise in the computed tubular surface.

Instead, in order to implement a 3D tubular constraint, we generate a nearby tubular structure to attract the current model as follows:

- Generate a binary image corresponding to the volume enclosed by the current mesh at time t.

- The 3D Chamfer distance map to the outside (background) of this volume is then computed, in a similar way to the one presented in 6.6.2. The centerline of this binary image is composed of, for each slice z, the voxel containing the maximum value of the distance map (in that slice).

- A binary image of the target tubular structure is then constructed with successive 3D spheres, each centered at a different centerline point, whose radii equal the Chamfer distance value to the outside at that point (see figure 6.12).

The Chamfer distance map to the outside of this new tubular structure is computed. The current model will be attracted towards the tubular structure, in the direction of the gradient of the Chamfer distance map.
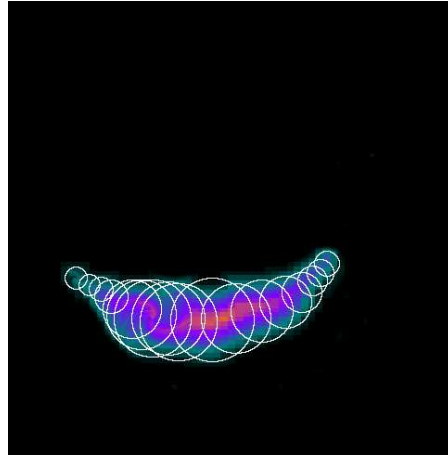
Figure 6.12: Tubular approximation of the rectum based on the Chamfer distance map to the outside of the current mesh (sagittal view).
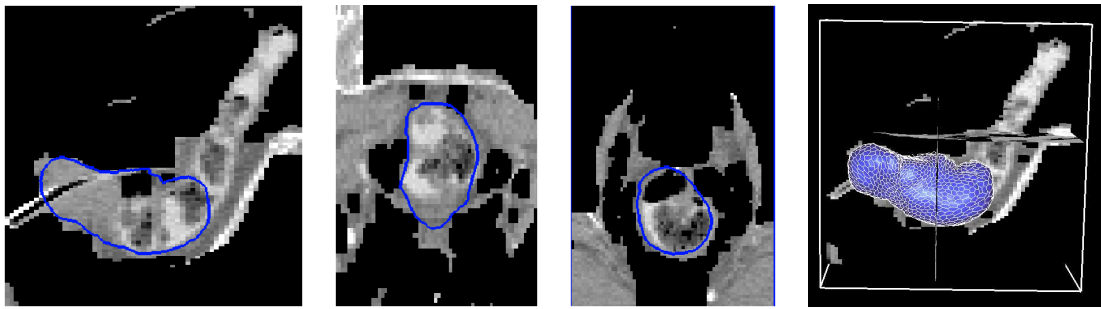
Figure 6.13: The resulting segmentation for the example rectum image. From left to right, sagittal, coronal and axial views, as well as the 3D model superimposed over the image.

This constraint is applied every 5 mesh deformation iterations. This constraint can be classified as internal force, since the distance map we use to build it is computed from the mesh itself, and not from the image.

The obtained segmentation for the example image is shown in figure 6.13.

6.8   Results and analysis

The validation of the automatic segmentations of the rectum were performed for the slices where a manual segmentation is available. The deformable model sometimes continues to segment the rectum in slices that are beyond the point where the expert has decided to stop his or her own delineation, but this does not necessarily mean that the automatic model is "wrong".

The proposed segmentation method for the rectum has been applied to a database

of 20 registered CT images of the lower abdomen of male patients. The results were compared to the (also registered) manual delineations performed by an expert. The expert segmentations used to build the initial models and the ones used for validation purposes are disjoint.

This comparison, in terms of sensitivity, positive predictive value and robust Hausdorff distance (95% quantile, in mm.), can be seen in figure 6.14. From these results, we have obtained a mean sensitivity and mean positive predictive value for the bladder of 0.87 and 0.92, respectively, with standard deviations of 0.12 and 0.08. The mean sensitivity and mean positive predictive value for the prostate are 0.88 and 0.81, with standard deviations of 0.11 and 0.13. For the rectum, the mean sensitivity and mean positive predictive value are 0.83 and 0.76, with standard deviations of 0.13 and 0.08.

One interesting point on this topic is that, while the bladder and the prostate were jointly segmented, the rectum is segmented using the prostate and bladder segmentations as input. This can seem as a drawback since, sometimes, fuzzy prostate borders may cause the prostate model to grow and overlap the rectum, and perhaps a non–overlapping constraint between prostate and rectum in a joint segmentation framework could be useful.

It would indeed be interesting to perform a joint segmentation of the three organs: bladder, prostate and rectum. However, a big advantage of our algorithm is its ability to accommodate the large variability of protocols and prior patient preparation for the rectums in our image database. Assumptions about its interior are carefully avoided, and the rectum is segmented by isolation, based on exterior (neighboring organ) information. In order to be able to introduce, for instance, a non–overlapping constraint on the rectum and prostate models, assumptions should be made about the interior of both structures so that a criterion could be established to decide which model pushes which and under what conditions. We have made the choice to privilege a broad applicability over minor prostate–rectum model overlaps that may sometimes occur, since the latter can be easily corrected by an expert if considered necessary.

Several automatic rectum segmentations are illustrated in figure 6.15. Final segmentations for prostate, bladder and rectum are shown in figure 6.17.

Figure 6.16 shows the automatic segmentation result for the rectum (blue contour) as well as the manual delineation (red contour) for entry 3 in table 6.16. The automatic segmentation has been mislead by the lack of definition of the rectum's boundaries. The tubular constraint also proves to limit the expressiveness of the deformable model, since it becomes more difficult for the mesh to adapt to highly irregular borders.

A quantitative analysis of the bladder segmentation results, grouped by target appearance (homogenous, non–homogenous) and according to the obtained over or under segmentations, is shown in Figure 6.18. The table shows that similar results in terms of sensitivity and positive predictive value are obtained for homogenous and non–homogenous bladders indistinctively, whith perhaps a tendency to slight under–segmentation in the non–homogenous cases. On the other hand,

Image	Bladder			Prostate			Rectum		
	Sensit.	PPV	H.D.	Sensit.	PPV	H.D.	Sensit.	PPV	H.D.
1	0.94	0.92	2.0	0.76	0.81	3.3	0.78	0.79	6.0
2	0.68	0.81	4.5	0.70	0.63	4.3	0.87	0.77	5.7
3	0.95	0.72	2.5	0.98	0.85	3.3	0.54	0.62	5.2
4	0.91	0.88	3.0	0.77	0.73	2.7	0.66	0.62	5.0
5	0.90	0.91	5.3	0.73	0.65	3.3	0.86	0.78	4.3
6	0.72	0.97	3.7	0.73	0.79	4.7	0.60	0.75	3.7
7	0.93	0.95	2.0	0.84	0.83	2.7	0.72	0.80	3.7
8	0.64	0.99	3.7	0.77	0.97	4.7	0.91	0.89	5.7
9	0.83	0.91	4.0	0.78	0.99	2.7	0.93	0.83	6.0
10	0.90	0.94	3.3	0.99	0.91	3.3	0.61	0.80	3.3
11	0.95	0.93	4.7	0.94	0.99	2.3	0.90	0.70	6.0
12	0.93	0.94	4.3	0.95	0.61	4.0	0.90	0.79	6.3
13	0.94	0.99	2.0	0.81	0.79	3.0	0.93	0.84	7.0
14	0.99	0.98	2.0	0.99	0.93	3.0	0.96	0.81	5.3
15	0.72	0.99	3.7	0.97	0.77	3.0	0.94	0.72	5.7
16	0.90	0.90	3.7	0.99	0.61	3.7	0.92	0.63	6.7
17	0.94	0.99	3.0	0.98	0.72	3.3	0.88	0.93	3.3
18	0.65	0.97	4.0	0.99	0.72	4.7	0.87	0.68	3.7
19	0.96	0.94	3.7	0.99	0.95	2.3	0.93	0.81	3.0
20	0.99	0.72	3.3	0.99	0.95	2.3	0.87	0.72	4.3
Mean	0.87	0.92	3.42	0.88	0.81	3.33	0.83	0.76	4.99
Std. Dev.	0.12	0.08	0.96	0.11	0.13	0.79	0.13	0.08	1.24
Min	0.64	0.72	2.00	0.70	0.61	2.30	0.54	0.62	3.00
Max	0.99	0.99	5.30	0.99	0.99	4.70	0.96	0.93	7.00

Figure 6.14: Sensitivity, Positive Predictive Value and robust Hausdorff Distance (95% quantile, in mm.) results of the automatic segmentations of the bladder, prostate and rectum with respect to the ones performed by an expert. Mean, standard deviation, minimum and maximum values are also indicated.
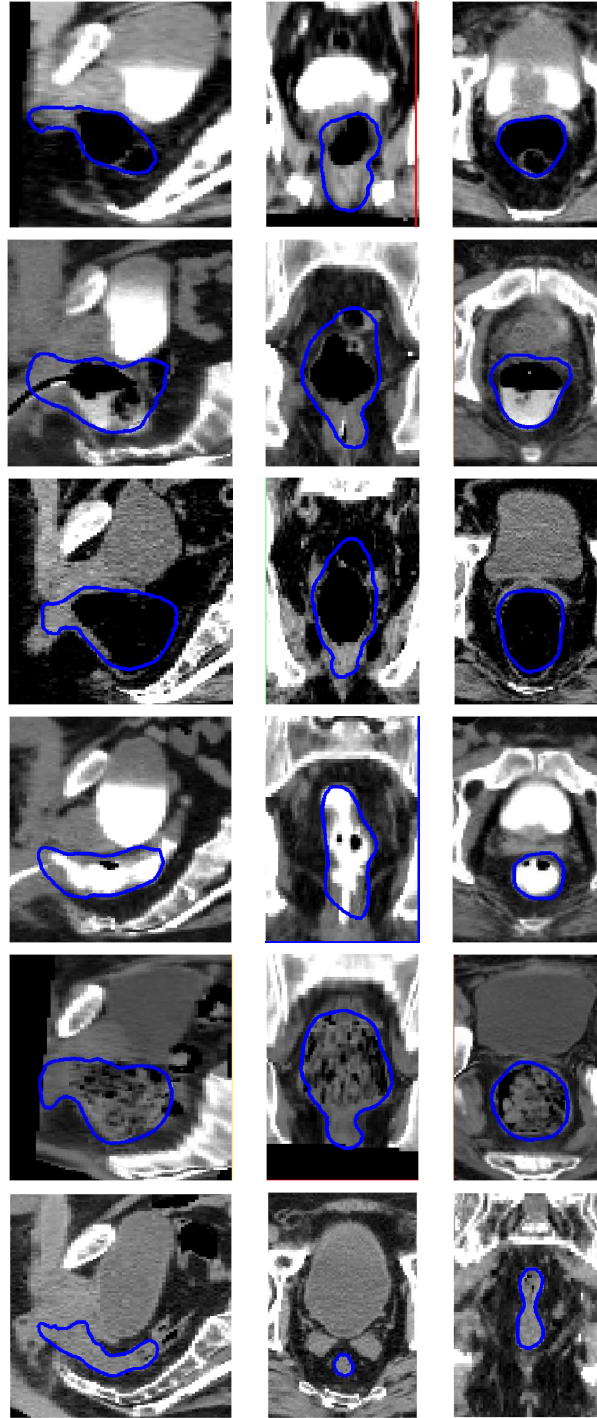
Figure 6.15: The resulting segmentation for the example rectum image. From left to right, sagittal, coronal and axial views superimposed over the original (registered and cropped) image. The results correspond to entries 2, 5, 11, 14, 17 and 19 in table 6.14.
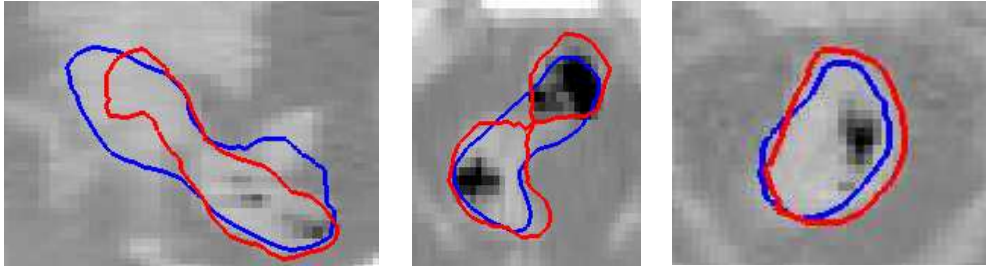
Figure 6.16: Automatic (blue) and manual (red) rectum segmentations for the worst–case encountered (the image that corresponds to entry 3 in table 6.14). From left to right, sagittal, coronal and axial views. This image illustrates the limitations induced by the imposition of a tubular constraint (it is more difficult for the model to attach to highly irregular structure contours) as well as those caused by the lack of definition of the structure's borders (i.e., the over segmentation seen in the sagittal slice).

under–segmentation is comparatively more frequent than over–segmentation, although both occur in relatively few cases. This occurs when there is a sufficiently large difference between the intensities of the interior of the bladder and that of the bladder wall, and is independent of the presence of contrast agent in the structure. However, contrast agent may cause a partial volume effect in the image, which could also influence the final result. An illustration of these phenomenons is shown in Figure 6.19.

Figure 6.20 shows that the method has a tendency to over–segment the prostate, rather than under–segment it. This is independent of the presence or absence of a contrast agent in the bladder, since the over–segmentation occurs towards the feet of the patient, and more rarely towards the rectum, when the latter is empty (and thus, of similar intensity value). The reason behind this tendency is the fact that there is no intensity information to guide the deformable model (or even the medical experts in their manual delineations). This causes the model to expand, as long as there is no shape or intensity information to avoid it. The posterior evaluation of the automatic segmentation results has, however, been approved and accepted as viable by the same medical experts who performed the original manual delineations of the structure. These findings are shown in Figure 6.21.

Results for the rectum are shown in Figure 6.22. More often than not, the structure is over–segmented, and this occurs almost systematically towards the endpoints of the rectum. This is due to the fact that the start and endpoint of the rectum are difficult to define precisely, and therefore medical experts may begin and end the manual segmentations at different points. This entails differences with the automatic segmentation, which does not incorporate hard–coded information about this. The definition and incorporation of such data would be an interesting perspective. The threshold that serves to eliminate fat tissue may sometimes cause small "holes" inside the rectum which don't connect to the surrounding fat, since they
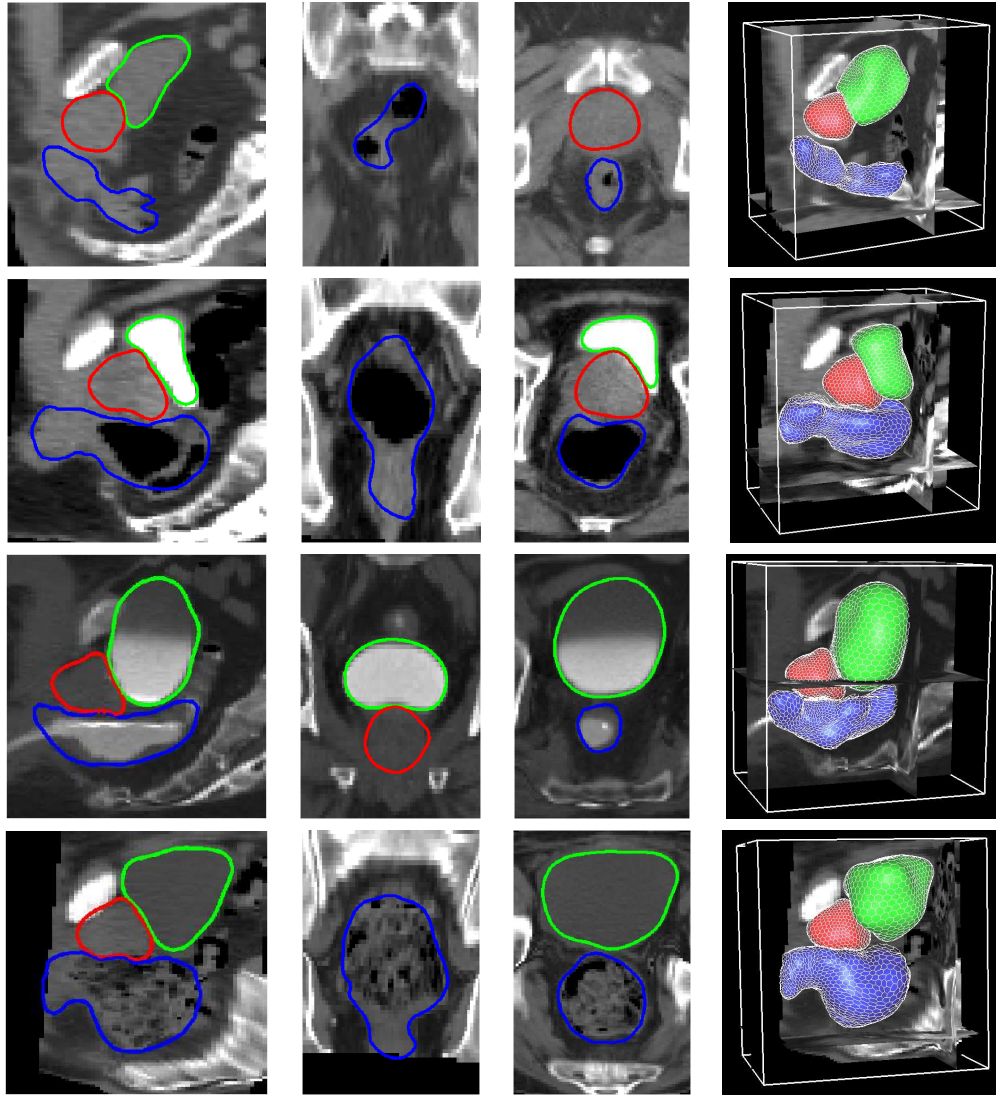
Figure 6.17: Automatic segmentations of the bladder, prostate and rectum, over the original (registered and cropped) image. From left to right, sagittal, coronal and axial views, as well as the 3D models of the results corresponding to entries 7, 8, 14 and 17 in table 6.14.

Group and nb. of imgs.	Sensitivity		PPV	
	Mean	Std. Dev.	Mean	Std. Dev.
Homogenous (12)	0.87	0.11	0.91	0.08
Non–homogenous(8)	0.84	0.17	0.95	0.03
Under–segmented(5)	0.68	0.03	0.94	0.07
Over–segmented(2)	0.97	0.02	0.72	0.01

Figure 6.18: Statistics for bladder segmentation, grouped by (non–)homogeneity, over or under segmentation. The number of cases in each group is specified in parentheses.
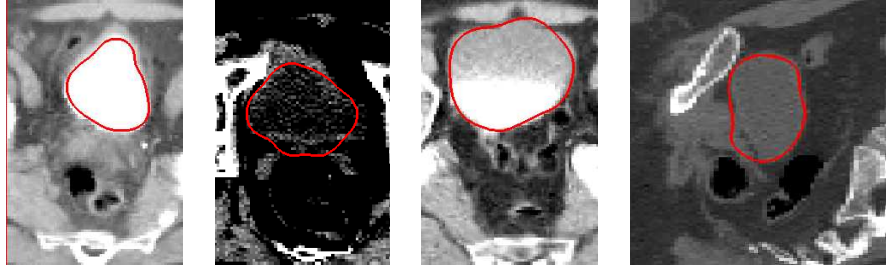
Figure 6.19: Automatic segmentations of the bladder, following figure 6.18. An intensity difference between the bladder and bladder wall is often at the origin of the under–segmentations. However, it is not systematic, as shown by the center–right image. An example of a (rare) over–segmentation is shown in the rightmost image, towards the seminal vesicles, where there is no difference in intensity with the seminal vesicles.

Case and nb. of imgs.	Sensitivity		PPV	
	Mean	Std. Dev.	Mean	Std. Dev.
Over–segmented (7)	0.90	0.12	0.67	0.06

Figure 6.20: Statistics for prostate segmentation, showing a general slight over–segmentation. Number of cases is indicated in parentheses.
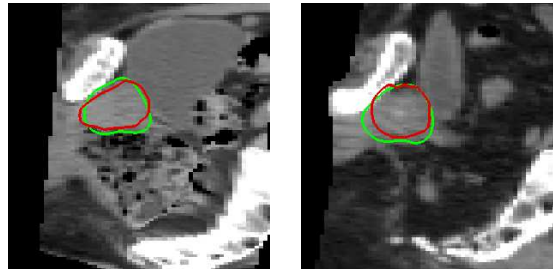
Figure 6.21: Automatic segmentations of the prostate are shown in green. Over–segmentation may occur (compared to manual segmentations, in red), mostly where there is no intensity information to limit the evolution of the model.

Case and nb. of imgs.	Sensitivity		PPV	
	Mean	Std. Dev.	Mean	Std. Dev.
Under–segmented (3)	0.64	0.06	0.78	0.02
Over–segmented (10)	0.90	0.03	0.75	0.06

Figure 6.22: Statistics for rectum segmentation, showing greater tendency to over–segmentation. Number of occurrences is indicated in parentheses. Sensitivity and positive predictive values clearly characterize the over–segmentation.
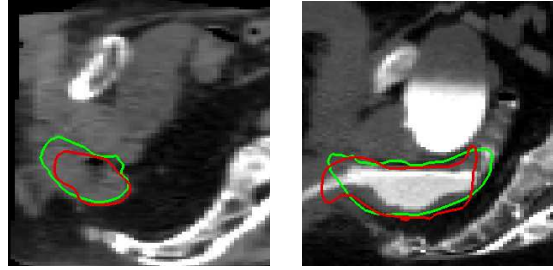
Figure 6.23: Automatic segmentations of the rectum, following figure 6.22. Over–segmentation may occur, mostly towards the start and endpoints of the rectum, which are also variable among medical expert segmentations. Automatic (green) and manual (red) segmentations are shown.

Case and nb. of imgs.		Mean			Std. Deviation		
		Sensit.	PPV	R.H.D.	Sensit.	PPV	R.H.D.
1.875x1.875x3 (7)	Bladder	0.86	0.88	3.28	0.11	0.08	1.27
	Prostate	0.79	0.78	3.4	0.09	0.08	0.76
	Rectum	0.72	0.73	4.8	0.13	0.07	0.92
0.97x0.97x3 (7)	Bladder	0.88	0.95	3.4	0.11	0.03	1.07
	Prostate	0.89	0.88	3.3	0.09	0.13	0.81
	Rectum	0.88	0.81	5.65	0.11	0.05	1.16
1.67x1.67x4 (6)	Bladder	0.86	0.92	3.56	0.14	0.10	0.35
	Prostate	0.98	0.79	3.21	0.01	0.13	0.91
	Rectum	0.90	0.75	4.45	0.03	0.10	1.45

Figure 6.24: Statistics for segmentation results, according to the voxel size of the original image. Table shows sensitivity, positive predictive values and robust Hausdorff distance measures.

are protected by the rectum wall. This thin wall might not be enough to prevent the deformable model from passing through it, and eventually under segmenting the structure. An illustration can be found in Figure 6.23.

The results of a quantitative analysis of the results according to image resolution is shown in figure 6.24. More accurate results are obtained, as may be expected, when the quality of the original image is better.

Conclusion and Perspectives

Contents

7.1 Synthesis of Contributions

In this manuscript we have proposed a novel, incremental method for the automatic segmentation of the prostate, as well as that of its organs at risk (bladder and rectum), in the frame of radiotherapy dose planning.

The heterogenous nature of the structures in the CT scans of our database, we have been confronted with many specific challenges, all of which are centered around two axes:

- **Adaptability to shape variability**: The target structures being soft tissues their shapes are prone to changes due to patient motion and positioning. Furthermore, the bladder and rectum are hollow organs whose fillings may change throughout the day and, therefore, differ among patients and image acquisitions.

- **Adaptability to intensity variability**: The preparation of the patient before image acquisition, the soft nature of the tissues and the variability of their fillings strongly influence the appearance of the target organs.

These research axes have given rise to several contributions in both national and international conferences, which we will detail in the next subsections.

7.1.1   Registration

We have contributed to the assessment and validation of the locally affine registration framework that was used to put the database images in a common space. This registration method seems truly appropriate for the problem, as the differences in intensity would mislead standard non–rigid registration methods. Using affine transformations to register the bone structures and a log–euclidean interpolation allows us to choose simple similarity measures and avoid registration errors induced by intensity dissimilarities in organs that must be aligned (such as with the registration of homogenous and non–homogenous bladders).

7.1.2   Bladder segmentation

The challenge of automatic segmentation of heterogenous bladder images (contrasted, non–contrasted, homogenous intensity, non–homogenous intensity) is rarely addressed in the literature. We have proposed a fully automatic method for the detection and initial approximation of the bladder, as well as the determination of the presence or absence of a contrast agent (progressive region growing). This method relies neither on strong shape assumptions nor on appearance a–priori. Following this computed approximation, a method for the automatic division of a 3D deformable model to adjust to the structure's (in–)homogeneities in each image was proposed and assessed. A new force designed to guide the deformation of each zone so that intensity homogeneity is enforced within each zone has also been presented and thoroughly tested, with positive results.

7.1.3   Bladder–prostate segmentation

Since the prostate shown a certain shape coherency among patients, and the intensity information that could guide the segmentation process is insufficient, we have presented a method for the automatic segmentation of the prostate by imposing a shape constraint based on Principal Component Analysis of the structure's shape. We have proposed an asymmetric non–overlapping constraint that is able to adjut to different frontier intensities.

7.1.4   Rectum segmentation

The segmentation of the rectum is particularly challenging due to the highly variable nature of its fillings, which dictate its shape and appearance. Documented approaches to automatically adjust to this variability are rare, and strong assumptions

are made concerning mostly the patient preparation before the image acquisition. This leads to rigid constraints on the applicability of the method. We have devised a completely novel approach that makes little or no assumptions about the structure's appearance. The idea of segmentation by isolation of the structure, as opposed to a delineation based on strong prior assumptions, is unprecedented. The adaptive tubular constraint that we propose provides a suitable initialization to all kinds of rectums that are present in our database.

The heterogeneity of the structures and the automatic results obtained shows a large adaptive capability of the method, which was our goal in the first place.

7.1.5 Evaluation

We have assessed the results of our segmentation approach on an heterogenous database of CT scans of the lower abdomen of male patients that had undergone different preparations prior to image acquisition. We have also evaluated inter–expert variability for prostate segmentation and had good results overall, despite the complexity of the segmentation task.

7.2 Perspectives

Many perspectives are open to pursue this work, ranging from technical improvements to more theoretical aspects of the problems at stake.

We describe these perspectives in the following subsections.

7.2.1 Bladder segmentation

Although highly adaptive, the absence of a well–defined bladder–prostate interface may cause the bladder model to partly invade the prostate. This issue is resolved by introducing a coupled deformation of the bladder and prostate models, as we have done, but it may still be interesting to search for possible improvements in the independent deformation stage.

7.2.2 Bladder–prostate segmentation

The inter– and intra– expert variability in the delineation of the prostate makes the validation of an automatic method difficult. Although we have been able to compare the automatic results with that of 5 different experts for some images, further assessment of this variability could be performed. In particular, more manual segmentations by more different experts may provide further insight into the problem, and it may result in more clinical experience being incorporated into the models.

7.2.3 Rectum segmentation

The results obtained from the application of our method to a database of CT images has shown that the method is flexible enough to accommodate marked differences

from one rectum to another. It would be interesting to incorporate a joint deformation of the rectum, the bladder and the prostate models, with specifically designed constraints to avoid overlap. However, our segmentation of the rectum is dependent on that of the bladder and the prostate. Without further information about the rectum's interior, how could a priority be established (i.e., which model pushes which) in the case of an overlap?

Another challenge would be to devise a method that automatically eliminates the seminal vesicles from the image. The seminal vesicles are currently avoided during rectum segmentation using a tubular constraint. However, on the images of the database, these structures are hardly visible. Another set of more precise images, or MRI images, would be needed to get a proper segmentation. The comparison of the results of both methods would be an interesting addition.

Although promising results have been obtained for the rectum itself, the model sometimes goes beyond the defined start and end points of the structure, entering part of the anal canal and/or the sigmoid. These "leakages" do not affect the result for the rectum nor its usefulness for radiotherapy planning, but they could definitely be improved if segmentations of the anal canal and of the sigmoid are desired. As the constrast in the anal canal area is far from suffisient, another shape information is needed to have a correct segmentation: from expert segmentation or from another type of image. This might inspire a useful extension to our work.

7.2.4   Validation

The availability of more expert segmentations of the structures would broaden the spectrum of possible validations, and would give more insight into the problem and other possible improvements or solutions. Statistics on intra– and inter–expert variability allowed us to position the automatic segmentations with respect to the results of manual delineation, but a greater number of experts and their manual segmentations would enlarge the possibilities of evaluation.

The locally–affine non–rigid registration method has been validated on the femoral heads. However, it we apply it to other pelvic bone structures as well, in a step that is essential to the success of our segmentation method. Further tests and validation concerning the registration of the other bone structures would be useful for a quantitative assessment of the registration process.

7.3   General perspectives

7.3.1   Multi–sequence segmentation: inclusion of MRI

One of the main reasons to include a statistical shape study in the prostate segmentation process is the difficulty to determine the structure's boundaries, which are often hardly visible in CT images. In MRI images, on the contrary, the structure's visibility is better, which would weigh in favor of a multi–sequence segmentation approach. However, there are some limitations to this approach.

First, there are some known difficulties associated with multi–spectral analysis, such as bias correction and reconstruction artifacts for MRI images. The fact that MRI sequences are expensive for the patient is also a limiting factor, and paired sequences (CT and MRI) are rare in the frame of radiotherapy planning and treatment.

Another practical problem is the fact that the target tissues are soft (and therefore subject to changes due to patient positioning, movement, and type and level of fillings in the case if the bladder and rectum). The waiting time and the patient's movements between the CT scan and the MRI acquisition could cause a change in position, size, appearance (due to a change of fillings) or shape of the target structures, and a simple affine registration would not suffice to align the organs in both images. It would be interesting to study this problem and device a method that could align the soft structures properly between the CT and the MRI images, so that full advantage can be taken of both the density information present in CT and the better definition of the structures in MRI.

7.3.2 Base structure for shape modeling

The force designed in section 4.6 requires a clear knowledge of the positions of the "interior" and the "exterior" of each model. Although rare in our experiments, a folding of the mesh would cause a confusion at the time of application of the forces, mistaking the interior for the exterior and viceversa, with obvious consequences for the segmentation results. The detection of these foldings is not an easy task.

The use of level sets (i.e., implicit deformable models) would be of help, since the model in that case is the zero–level–set of a function, and the "interior" and "exterior" can always be found. In fact, an intersting perspective would be to adapt the current process from simplex meshes to level sets.

- The force would be implemented the same way it is with simplex meshes, apart from the fact that the interior would be determined by the value of the level set function.

- The shape statistics used during prostate deformation could also be enforced. However, the process would be more costly in terms of computation time, since the model registrations that take place at each shape constraint application would be image based, instead of discrete mesh registrations.

- However, splitting the mesh into zones (as is required for bladder segmentation), would be more difficult. Using a discrete mesh, an injective function can be defined from its vertex set to a set of zones. In the case of level sets, the division of the structure would have to be computed at each iteration.

- Since our tube constraint is computed based on a binary image, it would be easy to adapt to a level set framework.

To conclude, although level sets would solve the problem of folding, they would also create some new difficulties, including an increase on the computation time.

7.3.3 Outlook

The segmentation framework proposed in this thesis will be integrated and used in real clinical environments thanks to the collaboration with DOSISOFT (www.dosisoft.com), within the european project MAESTRO (Methods and Advanced Equipment for Simulation and Treatment in Radio–Oncology). Snapshots of some segmentation results in this system that will be made available to hospitals and clinics can be found in appendix C.

7.4 Published contributions

- **J. Costa**, H. Delingette, J.-C. Diaz *et al. Towards an automatic delineation of lower abdomen structures for conformational radiotherapy based on CT images.* In Proceedings of the 44èmes journées scientifiques de la Société Française de Physique Médicale (SFPM 2005), June 2005.

- O. Commowick, V. Arsigny, **J. Costa**, N. Ayache et G. Malandain. *An Efficient Locally Affine Framework for the Registration of Anatomical Structures.* In *Proceedings of the Third IEEE International Symposium on Biomedical Imaging (ISBI 2006)*, pages 478-481, April 2006.

- **J. Costa**, H. Delingette et N. Ayache. *Automatic Segmentation of the Bladder Using Deformable Models.* In ISBI 2007, Crystal Gateway Marriott, Arlington, Virginia, USA, April 2007.

- **J. Costa**, H. Delingette, S. Novellas and N. Ayache. *Automatic Segmentation of Bladder and Prostate Using Coupled 3D Deformable Models.* In Proceedings of MICCAI, Brisbane, Australia, November 2007.

- O. Commowick, V. Arsigny, A. Isambert, **J. Costa**, F. Dhermain, F. Bidault, P–Y Bondiau, N. Ayache, and G. Malandain. *An Efficient Locally Affine Framework for the Smooth Registration of Anatomical Structures.* In *Medical Image Analysis*, 2008.

Locally Affine Registration

Contents

A.1 Locally Affine Registration

A.1.1 Locally Affine Transformations

Locally affine transformations are parameterized by a finite number N of affine components. Precisely, each component consists of an affine transformation A_i and of a non–negative weight function $w_i(x)$ which models its spatial extension: the influence of the ith component at point x is proportional to $w_i(x)$. Furthermore, they assume that for all x, $\sum_{i=1}^{N} w_i(x) = 1$, i.e. the weights are normalized.

In order to obtain a global transformation from several weighted components and obtain an *invertible* transformation, the authors use a *Log–Euclidean polyaffine framework*, which basically consists in averaging *infinitesimal* displacements associated to each affine component. The resulting global transformation is obtained by integrating an Ordinary Differential Equation (ODE), which can be done in a very efficient way. Log-Euclidean polyaffine transformations are always invertible, and their inverse can also be very efficiently computed.

A.1.2 Log–Euclidean Regularization

The authors use the 4x4 matrix representation of 3D affine transformation given by *homogeneous coordinates*. Whenever the amount of rotation present in an affine transformation A is less than π radians, one can define the *logarithm* of A, simply via the principal logarithm of the matrix representing A. This matrix logarithm is of the form: $\begin{pmatrix} M & v \\ 0 & 0 \end{pmatrix}$, where M is a 3x3 matrix (not necessarily invertible) and v a 3D vector. Conversely, a unique affine transformation is associated to any 4x4 matrix B of the latter form via its *matrix exponential*.

Taking the logarithm of affine transformations corresponds to linearizing the (curved) affine group around the identity, while conserving excellent theoretical properties (invariance with respect to inversion in particular). This allows to perform *Euclidean* (i.e. vectorial) operations on affine transformations via their logarithms.

This representation of affine transformations by vectors allows the direct generalization of classical vectorial regularization techniques.

For example, one can define a *Log-Euclidean* elastic energy between affine components:

$$Reg(A_i, w_i) = \sum_{i=1}^{N} \sum_{j \neq i} p_{i,j} \| \log(A_i) - \log(A_j) \|^2, \qquad (A.1)$$

where $p_{i,j} = \int_\Omega w_i(x).w_j(x)dx / \int_\Omega w_i(x)dx$, which take into account the spatial extensions of the components. Furthermore, one can define a *fluid* energy by regularizing the transformation corrections ΔA_i instead of the affine transformations A_i in (A.1). In the sequel, $\|.\|$ is set to $\|M\|^2 = \text{Trace}(M.M^T)$ (Frobenius norm).

A.1.3   Registration Algorithm

In the locally affine registration implementation, we chose to define entire areas which would adopt an affine behavior. Since convoluting areas with a gaussian kernel would penalize small areas neighboring large areas, the authors have implemented the weighting function for each area as a function of the minimal distance to the area: $w_i(x) = 1/(1 + \alpha.\text{dist}(x, \text{area}_i)^2)$. These weights are normalized.

The framework described so far is also independent of how each affine component of the transformation is evaluated. For our application, we have chosen to optimize all the affine components at the same time using a multi–resolution scheme. At each resolution, an alternate optimization is performed between the estimation of the affine components and the regularization of the transformation. The estimation of affine transformation corrections is done using a block-matching algorithm, which uses a correlation coefficient as a similarity measure. The transformation corrections ΔA_i of A_i^{M-1} are estimated at iteration M from the pairings $(x_v, x_v + d_v)$ using a least trimmed squares weighted procedure, which minimizes the following energy:

$$
\begin{aligned}
E(\Delta A_i) \quad = \quad & \sum_v \| \sum_{i=1}^{N} w_i(x_v + d_v) A_i^{M-1}.(x_v + d_v) \\
& - \sum_{i=1}^{N} w_i(x_v) \Delta A_i.A_i^{M-1}.x_v \|^2. \qquad (A.2)
\end{aligned}
$$

The balance between the regularization and the affine corrections is done by a parameter $\lambda \in [0, 1]$, which acts as a percentage of the mean Frobenius norm of the affine transformation corrections ($\frac{1}{N} \sum_{i=1}^{N} \|log(\Delta A_i)\|$).

All the computations are done using the simple displacement averaging method (**??**). One can indeed assume that the corrections are sufficiently small for the

transformation to remain invertible. The Log–Euclidean polyaffine framework is used only at the end of the registration to ensure the invertibility of the final transformation and to compute its inverse.

The STAPLE algorithm

The STAPLE algorithm, presented in [Warfield 2004], is used in this manuscript to test inter–expert variability for the delineation of the prostate, and to position the automatic results obtained with our proposed method with respect to this variability (chapter 5.

We describe this algorithm based on the Expectation–Maximization (EM) method, and we then move on to explain how this framework can be used to estimate the "most likely" segmentation, as well as the expert parameters, based on the available segmentations.

B.1   The Expectation–Maximization (EM) algorithm

The EM algorithm was introduced in [Dempster 1977] and later revised by [Van Leemput 1999]. We propose here the demonstration shown in [Flandin 2004], in which the EM is presented as an alternating minimization of similarity by means of the introduction of a hidden variable $\mathbf{T}$.

We call d_i the observed data of a problem, realizations of a random vectorial variable $\mathbf{D}$. We also consider a set of hidden variables $\mathbf{T}$ associated to $\mathbf{D}$. Finally, $\boldsymbol{\theta}$ is the set of model parameters used to estimate the probability distribution of $\mathbf{D}$. We will describe these parameters for our specific application in the next section.

The parameters can be estimated by maximizing their resemblance to a certain dataset. The log–resemblance is then written as follows:

$$L(\boldsymbol{\theta}) = \log p(\mathbf{D}|\boldsymbol{\theta}). \tag{B.1}$$

The estimation of $\boldsymbol{\theta}$ is therefore the following:

$$\hat{\boldsymbol{\theta}} = \arg\max_{\boldsymbol{\theta}} L(\boldsymbol{\theta}). \tag{B.2}$$

However, this formulation is usually difficult to maximize. The EM algorithm allows the resolution of this problem by introducing hidden variable $\mathbf{T}$ to the resemblance, and then maximizing this formulation in an alternating procedure. We therefore introduce $\mathbf{T}$ into equation B.1 by using the law of computation of conditional probabilities:

$$p(\mathbf{D}|\boldsymbol{\theta}) = \frac{p(\mathbf{D}, \mathbf{T}|\boldsymbol{\theta})}{p(\mathbf{T}|\mathbf{D}, \boldsymbol{\theta})}. \tag{B.3}$$

By introducing the probability distribution $\tilde{p}(\mathbf{T})$, we obtain the following formulation for the log–resemblance:

$$
\begin{aligned}
L(\boldsymbol{\theta}) &= \log\left(\frac{p(\mathbf{D},\mathbf{T}|\boldsymbol{\theta})}{p(\mathbf{T}|\mathbf{D},\boldsymbol{\theta})}\frac{\tilde{p}(\mathbf{T})}{\tilde{p}(\mathbf{T})}\right) \\
&= \log\left(\frac{p(\mathbf{D},\mathbf{T}|\boldsymbol{\theta})}{\tilde{p}(\mathbf{T})}\right) + \log\left(\frac{\tilde{p}(\mathbf{T})}{p(\mathbf{T}|\mathbf{D},\boldsymbol{\theta})}\right).
\end{aligned}
\tag{B.4}
$$

Since this equation is true for any $\mathbf{T}$, we compute the expectation over variable $\mathbf{T}$:

$$
L(\boldsymbol{\theta}) = \underbrace{\sum_{\mathbf{T}} \tilde{p}(\mathbf{T})\log\left(\frac{p(\mathbf{D},\mathbf{T}|\boldsymbol{\theta})}{\tilde{p}(\mathbf{T})}\right)}_{\mathcal{L}(\tilde{p},\boldsymbol{\theta})} + \underbrace{\sum_{\mathbf{T}} \tilde{p}(\mathbf{T})\log\left(\frac{\tilde{p}(\mathbf{T})}{p(\mathbf{T}|\mathbf{D},\boldsymbol{\theta})}\right)}_{KLD(\tilde{p}(\mathbf{T})\|p(\mathbf{T}|\mathbf{D},\boldsymbol{\theta}))}.
\tag{B.5}
$$

The second term of this equation is the Kullback–Leibler divergence between $\tilde{p}(\mathbf{T})$ and $p(\mathbf{T}|\mathbf{D},\boldsymbol{\theta})$, which has the property of being always positive, and zero only when both distributions are equal. $\mathcal{L}(\tilde{p},\boldsymbol{\theta})$ is therefore a lower bound for the log–resemblance for any distribution $\mathbf{T}$. Therefore, maximizing $L(\boldsymbol{\theta})$ is equivalent to maximizing $\mathcal{L}(\tilde{p},\boldsymbol{\theta})$ if $\tilde{p}(\mathbf{T}) = p(\mathbf{T}|\mathbf{D},\boldsymbol{\theta})$. The EM algorithm is based on this principle, and applies an alternate maximization as shown in algorithm 2.

Algorithme 2 General EM Algorithm

1: Initialization of parameters $\boldsymbol{\theta}^0$ at iteration 0
2: **répéter**
3:     Expectation step: computation of $\tilde{p}^{t+1}(\mathbf{T}) = p(\mathbf{T}|\mathbf{D},\boldsymbol{\theta}^t)$
4:     Maximization step: computation of $\boldsymbol{\theta}^{t+1} = \arg\max_{\boldsymbol{\theta}} \mathcal{L}(\tilde{p}^{t+1},\boldsymbol{\theta})$.
5: **jusqu'à** the log–resemblance stops evolving.

Function $\mathcal{L}(\tilde{p}^{t+1},\boldsymbol{\theta})$ depends on the particular problem at stake. Finally, it can be shown (see [Flandin 2004] for more details) that maximizing $\mathcal{L}(\tilde{p}^{t+1},\boldsymbol{\theta})$ for $\boldsymbol{\theta}$ is equivalent to maximizing the following function $Q(\boldsymbol{\theta})$:

$$
Q(\boldsymbol{\theta}) = \sum_{\mathbf{T}} \tilde{p}^{t+1}(\mathbf{T})\log p(\mathbf{D},\mathbf{T}|\boldsymbol{\theta}).
\tag{B.6}
$$

B.2   Application to multi–label segmentations

B.2.1   Problem formalization

In the multi–label case, $L-1$ structures are manually segmented by K experts. The background of the image is also considered as a structure (with label 0). Therefore, the observed data $\mathbf{D}$ are these manual segmentations, d_{ij} corresponds to the label assigned to voxel i by expert j. For simplicity, we will call d_i the vector of observed

data, such that $d_i = d_{i0}, ..., d_{iK-1}$. $\mathbf{T}$ corresponds to the true segmentation, which takes its values from the set $\{0, ..., L-1\}$, in which label 0 corresponds to the background class.

Parameters $\theta_{js's}$ correspond, for each expert j, to the probability $p(D_{ij} = s'|T_i = s)$ that he will label voxel i as belonging to class s' even though it really belongs to class s. Finally, $\pi_l \triangleq g(T_i = l)$ is the *a priori* probability of finding a voxel whose label is l, independently of its spatial position. It is estimated as the mean of the percentage of voxels labeled as l in the images.

$$\pi_l = \frac{1}{KN} \sum_{i=1}^{N} \sum_{j=0}^{K-1} \delta(d_{ij}, l) \tag{B.7}$$

o $\delta(d_{ij}, l)$ corresponds to the Kronecker delta function, whose value is 1 when d_{ij} is l, and 0 otherwise. The model parameters $\boldsymbol{\theta}$ will therefore be:

$$\boldsymbol{\theta} = \{\theta_0, ..., \theta_{K-1}\} \tag{B.8}$$

B.2.2   Expectation Step

In this stage, we compute the *a posteriori* probability $p(\mathbf{T}|\mathbf{D}, \boldsymbol{\theta}^t)$. Since we assume a spatial independence, the probability W_{si}^{t+1} at each voxel i can be computed as follows:

$$W_{si}^{t+1} \triangleq \tilde{p}^{t+1}(T_i = s) = p(T_i = s|\mathbf{D} = d_i, \boldsymbol{\theta}^t). \tag{B.9}$$

This equation corresponds to the probability of obtaining label $T_i = s$, knowing the observed data d_i and the expert parameters $\boldsymbol{\theta}^t$ obtained in the previous iteration. By using Bayes' law, we obtain:

$$W_{si}^{t+1} \triangleq \frac{\pi_s p(\mathbf{D} = d_i|T_i = s, \boldsymbol{\theta}^t)}{p(\mathbf{D} = d_i|\boldsymbol{\theta}^t)}. \tag{B.10}$$

where π_s is the *a priori* probability of obtaining label s in segmentation $\mathbf{T}$. We note that, following Bayes' law, $p(\mathbf{D} = d_i|\boldsymbol{\theta}^t) = \sum_l \pi_l p(\mathbf{D} = d_i|T_i = l, \boldsymbol{\theta}^t)$, which allows us to write W_{si}^{t+1} as follows:

$$W_{si}^{t+1} \triangleq \frac{\pi_s p(\mathbf{D} = d_i|T_i = s, \boldsymbol{\theta}^t)}{\sum_{l=0}^{L-1} \pi_l p(\mathbf{D} = d_i|T_i = l, \boldsymbol{\theta}^t)}. \tag{B.11}$$

We also assume that the experts are independent, which leads to the following relation:

$$p(\mathbf{D} = d_i|T_i = s, \boldsymbol{\theta}^t) = \prod_{j=1}^{K} p(D_j = d_{ij}|T_i = s, \theta_j^t). \tag{B.12}$$

We notice that $p(D_j = d_{ij}|T_i = s, \theta_j^t) = \theta_{jd_{ij}s}^t$. This allows us to simplify W_{si}^{t+1} as follows:

$$W_{si}^{t+1} = \frac{\pi_s \left(\prod_{j=0}^{K-1} \theta_{jd_{ij}s}^t \right)}{\sum_{l=0}^{L-1} \pi_l \left(\prod_{j=0}^{K-1} \theta_{jd_{ij}l}^t \right)}. \tag{B.13}$$

B.2.3 Maximization Step

From this evaluation of $\tilde{p}^{t+1}(\mathbf{T})$, we wish to find the maximum of $Q(\boldsymbol{\theta})$, defined in equation B.6. To that end, we write that function using the problem data:

$$Q(\boldsymbol{\theta}) = \sum_i \sum_{l=0}^{L-1} W_{li}^{t+1} \log p(\mathbf{D} = d_i, T_i = l|\boldsymbol{\theta}). \tag{B.14}$$

We use, once more, Bayes' law:

$$p(\mathbf{D} = d_i, T_i = l|\boldsymbol{\theta}) = p(\mathbf{D} = d_i|T_i = l, \boldsymbol{\theta})p(T_i = l|\boldsymbol{\theta}). \tag{B.15}$$

We can then rewrite $Q(\boldsymbol{\theta})$ as follows:

$$
\begin{aligned}
Q(\boldsymbol{\theta}) &= \sum_i \sum_{l=0}^{L-1} W_{li}^{t+1} \log \left(p(\mathbf{D} = d_i|T_i = l, \boldsymbol{\theta})p(T_i = l|\boldsymbol{\theta}) \right) \tag{B.16} \\
&= \sum_i \sum_{l=0}^{L-1} \left(W_{li}^{t+1} \log \pi_l \right) + \sum_i \sum_{l=0}^{L-1} \sum_{j=0}^{K-1} \left(W_{li}^{t+1} \log p(D_j = d_{ij}|T_i = l, \theta_j) \right).
\end{aligned}
$$

The following constraint on θ_j is added: $\sum_{s'} \theta_{js's} = 1$. Since the first term of the equation does not depend on θ_j, we obtain, for each θ_j, the following set of equations:

$$
\begin{cases}
\frac{\partial \left(Q(\boldsymbol{\theta}) + \lambda_1 \sum_{s'} \theta_{js's} \right)}{\partial \theta_{js's}} = \lambda_1 + \frac{\sum_{i:d_{ij}=s'} W_{si}^{t+1}}{\theta_{js's}} = 0, \\
\\
\sum_{s'} \theta_{js's} = 1
\end{cases}
\tag{B.17}
$$

This is a linear system, and its solution can be written as:

$$\theta_{js's}^{t+1} = \frac{\sum_{i:d_{ij}=s'} W_{si}^{t+1}}{\sum_i W_{si}^{t+1}} \tag{B.18}$$

B.3 Application to mono–label segmentations

B.3.1 Problem formalization

We are interested in the case where only one structure has been segmented by each expert. The choices of experts d_{ij} take their values from the set $\{0, 1\}$, the value 1 meaning that the voxel belongs to the sought structure. The background is also considered as a structure in itself.

The parameters for each expert are, in this case, $p_j \triangleq \theta_{j11} = p(D_{ij} = 1|T_i = 1)$ and $q_j \triangleq \theta_{j00} = p(D_{ij} = 0|T_i = 0)$, since the other parameters can be derived by substraction: $\theta_{j01} = 1 - p_j$ and $\theta_{j10} = 1 - q_j$. Only one π is enough, as well. We have $\pi \triangleq \pi_1 = g(T_i = 1)$, π_0 also being obtained by substraction: $\pi_0 = 1 - \pi$. Finally, in this case, only W_{1i}^{t+1} (called W_i^{t+1} in this case) is computed, since W_{0i}^{t+1} can be obtained as $1 - W_i^{t+1}$.

B.3.2 Expectation Step

The W_i^{t+1} are obtained by using equation B.13, which can be simplified by using the properties of θ_j. Warfield et al. simplify W_i^{t+1} by defining α_i and β_i as follows:

$$\alpha_i = \prod_{j:d_{ij}=1} \theta_{j11}^t \prod_{j:d_{ij}=0} \theta_{j01}^t = \prod_{j:d_{ij}=1} p_j^t \prod_{j:d_{ij}=0} (1 - p_j^t) \qquad \text{(B.19)}$$

$$\beta_i = \prod_{j:d_{ij}=0} \theta_{j00}^t \prod_{j:d_{ij}=1} \theta_{j10}^t = \prod_{j:d_{ij}=0} q_j^t \prod_{j:d_{ij}=1} (1 - q_j^t) \qquad \text{(B.20)}$$

W_i^{t+1} are therefore computed as follows:

$$W_i^{t+1} = \frac{\pi\alpha_i}{\pi\alpha_i + (1 - \pi)\beta_i} \qquad \text{(B.21)}$$

B.3.3 Maximization Step

The maximization step uses the same equations as for the multi–label segmentations case. These equations are only used to compute parameters p_j^{t+1} and q_j^{t+1}, and their formulation is simplified as follows:

$$\begin{cases} p_j^{t+1} = \frac{\sum_{i:d_{ij}=1} W_i^{t+1}}{\sum_i W_i^{t+1}} \\ \\ q_j^{t+1} = \frac{\sum_{i:d_{ij}=0}(1 - W_i^{t+1})}{\sum_i (1 - W_i^{t+1})} \end{cases} \qquad \text{(B.22)}$$

Snapshots of IsoGray

Figures C.1 and C.2 show some shapshots of the IsoGray system, which incorporates the segmentation methods proposed in this thesis, and will be made available to hospitals and clinics through the DOSISOFT company (www.dosisoft.com).
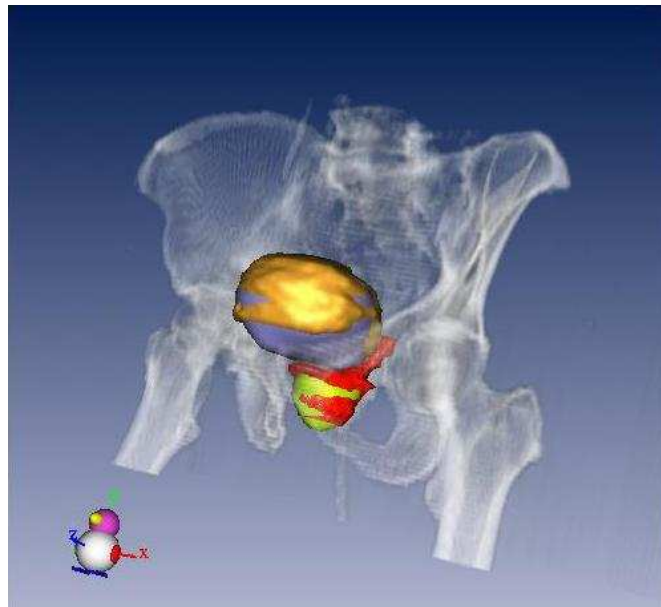
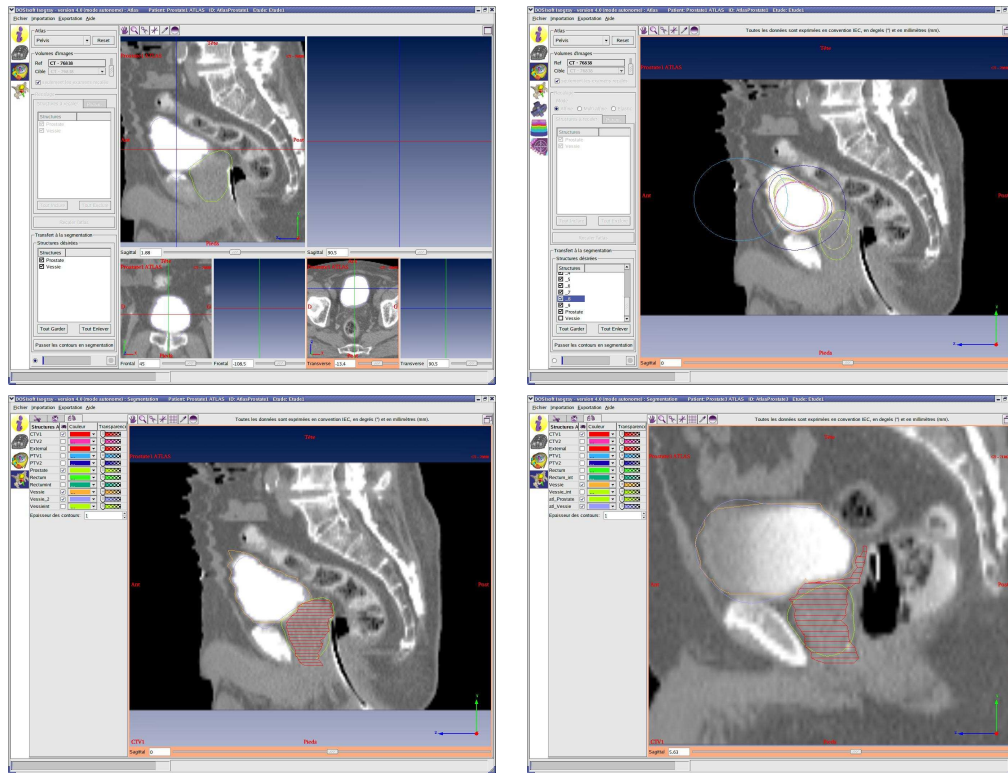Figure C.1: 3D view of the automatic segmentations of the bladder and prostate, IsoGray software.

Figure C.2: Automatic segmentations of the bladder and prostate, performed through the methods described in this thesis, and integrated into the IsoGray software.

Bibliography

[Akimoto 2004] T. Akimoto, H. Muramatsu et M. Takahashi . *Rectal bleeding after hypofractionated radiotherapy for prostate cancer: correlation between clinical and dosimetric parameters and the incidence of grade 2 or worse rectal bleeding.* Int J Radiat Oncol Biol Phys., vol. 4, pages 1033–9, 2004. 102

[Altwein 1997] J Altwein, P Ekman et M Barry. *How is quality of life in prostate cancer patients influenced by modern treatment? the Wallenberg Symposium.* Urology, vol. 49, no. 4A, suppl, pages 66–76, 1997. 32

[Androutsos 1997] Dimitrios Androutsos, Panos E. Trahanias et Anastasios N. Venetsanopoulos. *Application of Active Contours for Photochromic Tracer Flow Extraction.* IEEE Trans. Med. Imaging, vol. 16, no. 3, pages 284–293, 1997. 42

[Arsigny 2006] Vincent Arsigny, Olivier Commowick, Xavier Pennec et Nicholas Ayache. *A Fast and Log-Euclidean Polyaffine Framework for Locally Affine Registration.* Research report RR-5865, INRIA Sophia-Antipolis, March 2006. 65

[Aylward 2002] Stephen R. Aylward et Elizabeth Bullitt. *Initialization, Noise, Singularities and Scale in Height Ridge Traversal for Tubular Object Centerline Extraction.* IEEE Trans. Med. Imaging, vol. 21, no. 2, pages 61–75, 2002. 54

[Baxt 1995] W.G. Baxt. *Application of artificial neural networks to clinical medicine.* Lancet, no. 346, pages 1135–1138, 1995. 43

[Beasley 2005] M. Beasley, D. Driver et H.J. Dobbs. *Complications of radiotherapy: improving the therapeutic index.* Cancer Imaging, vol. 1, no. 5, pages 78–84, 2005. 26

[Bemmel 2003] C.M. Van Bemmel, L.J. Spreeuwers, M.A. Viergever et W.J. Niessen. *Level–set–based artery–vein separation in blood pool agent CE–MR angiograms.* IEEE Transactions on Medical Imaging, vol. 22, no. 10, pages 1224–1234, 2003. 55

[Besag 1986] J. Besag. *On the statistical analysis of dirty pictures.* Journal of Royal Stat. Soc. Ser. B (Methodological), vol. 48, no. 3, pages 259–302, 1986. 43

[Besl 1992] P.J. Besl et N.D. McKay. *A Method for Registration of 3D Shapes.* IEEE Transactions on Pattern Analysis and Machine Intelligence, vol. 14, no. 2, pages 239–256, 1992. 75

[Bezdek 1993] J. C. Bezdek, L. O. Hall et L. P. Clarke. *Review of MR image segmentation techniques using pattern recognition.* Medical Physics, vol. 20, pages 1033–1048, 1993. 42

[Bitter 2001] A.E. Bitter, Kaufman et M. Sato. *Penalized–distance volumetric skeleton algorithm.* IEEE Transactions on Visualization and Computer Graphics, vol. 3, pages 195–206, 2001. 54

[Boehmer 2006] D. Boehmer et D. Kuczer . *Influence of Organ at Risk Definition on Rectal Dose-Volume Histograms in Patients with Prostate Cancer Undergoing External-Beam Radiotherapy.* Strahlentherapie und Onkologie, vol. 182, no. 5, pages 277–282, 2006. 101

[Bondiau 2004] Pierre-Yves Bondiau. *Mise en oeuvre et évaluation d'outils de fusion d'image en radiothérapie.* Thèse de sciences, Université de Nice-Sophia Antipolis, November 2004. 11, 46

[Broadhurst 2005] R.E. Broadhurst, J. Stough, S.M. Pizer et E.L. Chaney. *Histogram Statistics of Local Model-Relative Image Regions.* In Ole Fogh Olsen, Luc Florack et Arjan Kuijper, editeurs, DSSCV, volume 3753 of *Lecture Notes in Computer Science*, pages 72–83. Springer, 2005. 48, 50

[Bueno 2001] G. Bueno, M. Fisher, K. Burnham, J. Mills et O. Haas. *Automatic segmentation of clinical structures for RTP: Evaluation of a morphological approach.* In Medical Image Understanding and Analysis, pages 73–76, 2001. 47, 52

[Bueno 2004] G. Bueno, A. Martínez-Albalá et A. Adán. *Fuzzy-Snake Segmentation of Anatomical Structures Applied to CT Images.* In Aurélio C. Campilho et Mohamed S. Kamel, editeurs, ICIAR (2), volume 3212 of *Lecture Notes in Computer Science*, pages 33–42. Springer, 2004. 48, 50

[Cachier 2003] P. Cachier, E. Bardinet, D. Dormont, X. Pennec et N. Ayache. *Iconic Feature Based Nonrigid Registration: The PASHA Algorithm.* CVIU, vol. 89, no. 2-3, pages 272–298, Feb.-march 2003. 66

[Camapum 2004] Juliana Fernandes Camapum, Alzenir O. Silva, Alan N. Freitas, H. de F. Bassani et F. Mendes O. Freitas. *Segmentation of Clinical Structures from Images of the Human Pelvic Area.* In SIBGRAPI, pages 10–16. IEEE Computer Society, 2004. 47, 50

[Caselles 1995a] Vicent Caselles, Ron Kimmel et Guillermo Sapiro. *Geodesic Active Contours.* In ICCV, pages 694–699, 1995. 44

[Caselles 1995b] Vincent Caselles, Ron Kimmel et Guillermo Sapiro. *Geodesic Active Contours.* In ICCV, pages 694–699, 1995. 55

[C.C. 2003] Parker C.C., Damyanovich A., Haycocks T., Haider M., Bayley A. et Catton C.N. *Magnetic resonance imaging in the radiation treatment planning of localized prostate cancer using intra-prostatic fiducial markers for computed tomography co-registration.* Radiotherapy and Oncology, vol. 66, no. 2, pages 217–224, 2003. 34

[Chan 2001] T. F. Chan et L. A. Vese. *Active contours without edges.* Image Processing, IEEE Transactions on, vol. 10, no. 2, pages 266–277, 2001. 44, 45, 55

[Chen 2004] J. Chen et A.A. Amini. *Quantifying 3D vascular structures in MRA images using hybrid pde and geometric deformable models.* IEEE Transactions on Medical Imaging, vol. 23, no. 10, pages 1251–1261, 2004. 55

[Clark 2003] JA Clark, TS Inui et RA Silliman. *Patients' perceptions of quality of life after treatment for early prostate cancer.* J Clinical Oncology, vol. 21, pages 3777–3784, 2003. 32

[Cohen 1991] L. D. Cohen. *On active contour models and balloons.* Computer Vision, Graphics, and Image Processing. Image Understanding, vol. 53, no. 2, pages 211–218, 1991. 45

[Cohen 1993] L.D. Cohen et I. Cohen. *Finite-Element Methods for Active Contour Models and Balloons for 2-D and 3-D Images.* PAMI, vol. 15, no. 11, pages 1131–1147, November 1993. 44

[Coleman 1979] Guy B. Coleman et Harry C. Andrews. *Image Segmentation by Clustering.* Proceedings of the IEEE, vol. 67, no. 5, pages 773–785, May 1979. 42

[Collier 2003] D.C. Collier, S.S.C. Burnett et M. Amin. *Assessment of consistency in contouring of normal-tissue anatomic structures. .* Journal of Applied Clinical Medical Physics, vol. 4, no. 1, 2003. 40

[Commowick 2006] O. Commowick, V. Arsigny, J. Costa, N. Ayache et G. Malandain. *An Efficient Locally Affine Framework for the Registration of Anatomical Structures.* In IEEE International Symposium on Biomedical Imaging 2006, pages 478–481, Crystal Gateway Marriott, Arlington, Virginia, USA, April 2006. 8, 64, 65

[Commowick 2008] Olivier Commowick, Vincent Arsigny, Aurélie Isambert, Jimena Costa, Frédéric Dhermain, François Bidault, Pierre-Yves Bondiau, Nicholas Ayache et Grégoire Malandain. *An Efficient Locally Affine Framework for the Smooth Registration of Anatomical Structures.* Medical Image Analysis, 2008. In Press. 8

[Cootes 1995a] T. F. Cootes, C. J. Taylor, D. H. Cooper et J. Graham. *Active shape models - Their training and application.* Computer Vision and Image Understanding, vol. 61, pages 38–59, January 1995. 45, 90

[Cootes 1995b] Timothy F. Cootes, Christopher J. Taylor, David H. Cooper et Jim Graham. *Active Shape Models-Their Training and Application.* Computer Vision and Image Understanding, vol. 61, no. 1, pages 38–59, 1995. 91

[Cosío 2005] Fernando Arámbula Cosío. *Prostate Segmentation Using Pixel Classification and Genetic Algorithms*. In Alexander F. Gelbukh, Alvaro de Albornoz et Hugo Terashima-Marín, editeurs, MICAI, volume 3789 of *Lecture Notes in Computer Science*, pages 910–917. Springer, 2005. 50

[Costa 2005] J. Costa, H. Delingette, J.-C. Diaz, W. Wibault et A. Egelmeers. *Towards an automatic delineation of lower abdomen structures for conformational radiotherapy based on CT images*. In Proceedings of the 44èmes journées scientifiques de la Société Française de Physique Médicale (SFPM 2005), June 2005. 8

[Costa 2007a] Jimena Costa, Hervé Delingette, Sebastien Novellas et Nicholas Ayache. *Automatic Segmentation of Bladder and Prostate Using Coupled 3D Deformable Models*. In Proceedings of Medical Image Computing and Computer-Assisted Intervention, LNCS 4791, pages 252–260, Brisbane, Australia, 2007. 8, 96

[Costa 2007b] M.J. Costa, H. Delingette et N. Ayache. *Automatic Segmentation of the Bladder Using Deformable Models*. In ISBI 2007, Crystal Gateway Marriott, Arlington, Virginia, USA, April 2007. 8, 82

[Cremers 2004] D. Cremers, S. J. Osher et S. Soatto. *Kernel density estimation and intrinsic alignment for knowledge-driven segmentation: Teaching level sets to walk*. In C. E. Rasmussen, editeur, Pattern Recognition (Proc. DAGM), volume 3175 of *LNCS*, pages 36–44. Springer, 2004. 45

[Crook 1995] J.M. Crook, Y. Raymond et D. . Salhani. *Prostate motion during standard radiotherapy as assessed by fiducial markers*. Radiation Oncology, vol. 1, pages 35–42, 1995. 33

[Dam 2004] Erik Dam, P. Thomas Fletcher, Stephen M. Pizer, Gregg Tracton et Julian Rosenman. *Prostate Shape Modeling Based on Principal Geodesic Analysis Bootstrapping*. In Christian Barillot, David R. Haynor et Pierre Hellier, editeurs, Medical Image Computing and Computer-Assisted Intervention, volume 3217 of *Lecture Notes in Computer Science*, pages 1008–1016. Springer, 2004. 45, 50

[Davis 2005] B. C. Davis, Mark Foskey, Julian Rosenman, L. Goyal, S. Chang et S. Joshi. *Automatic Segmentation of Intra-treatment CT Images for Adaptive Radiation Therapy of the Prostate*. In James S. Duncan et Guido Gerig, editeurs, Medical Image Computing and Computer-Assisted Intervention, volume 3749 of *Lecture Notes in Computer Science*, pages 442–450. Springer, 2005. 50

[de Bruijne 2003] M. de Bruijne, B. van Ginneken, M. Viergever et W. Niessen. *Adapting active shape models for 3D segmentation of tubular structures in medical images*. IPMI, vol. 2732, pages 136–147, 2003. 55

[Dearnaley 1999a] D.P. Dearnaley, V.S. Khoo et A.R. Norman. *Comparison of radiation side–effects of conformal and conventional radiotherapy in prostate cancer: a randomised trial.* Lancet, vol. 353, pages 267–272, 1999. 29

[Dearnaley 1999b] DP Dearnaley, VS Khoo et AR Norman. *Comparison of radiation side-effects of conformal and conventional radiotherapy in prostate cancer: a randomised trial.* vol. 353, pages 267–272, 1999. 30

[Delingette 1994] H. Delingette. *Simplex Meshes: a General Representation for 3D Shape Reconstruction.* In Proc. of Int. Conf. on Computer Vision and Pattern Recognition (CVPR'94), pages 856–857, Seattle, USA, June 1994. 44, 74

[Delingette 1999] Hervé Delingette. *General Object Reconstruction Based on Simplex Meshes.* Int. J. Comput. Vision, vol. 32, no. 2, pages 111–146, 1999. 77

[Delingette 2001] H. Delingette et J. Montagnat. *Shape and topology constraints on parametric active contours.* Comput. Vis. Image Underst., vol. 83, no. 2, pages 140–171, 2001. 4

[Dempster 1977] A. Dempster, N. Laird et D. Rubin. *Maximum Likelihood from incomplete data via the EM algorithm.* Journal of the Royal Statistical Society, vol. 39 (Series B), 1977. 131

[Deschamps 2001] T. Deschamps et L.D. Cohen. *Fast extraction of minimal paths in 3D images and applications to virtual endoscopy.* Medical Image Analysis, vol. 5, no. 4, December 2001. 55

[Duda 1973] R.O. Duda et P.E. Hart. Pattern classification and scene analysis. John Wiley and Sons., New York, 1973. 42

[Dunn 1974] J. C. Dunn. *A fuzzy relative of the ISODATA process and its use in detecting compact well-separated clusters.* Journal of Cybernetics, vol. 3, pages 32–57, 1974. 42

[Fenster 2001] S.D. Fenster, C.B.G. Kuo et J.R. Kender. *Nonparametric Training of Snakes to Find Indistinct Boundaries.* In MMBIA01, 2001. 48

[Fiorino 1998] C. Fiorino, M. Reni, A. Bolognesi, G. M. Cattaneo et R. Calandrino. *Intra- and Inter-observer variability in contouring prostate and seminal vesicles: implications for conformal treatment planning .* Radiation Oncol, vol. 47, pages 285–292, 1998. 40

[Fiorino 2002] C. Fiorino, V. Vavassori et G. Sanguineti. *Rectum contouring variability in patients treated for prostate cancer: impact on rectum dose-volume histograms and normal tissue complication probability.* Radiotherapy and Oncology, vol. 63, no. 3, pages 249–255, 2002. 101

[Fischler 1973] M. Fischler et R. Elschlager. *The Representation and Matching of Pictorial Structures*. IEEE Trans. on Computers, vol. 22, no. 1, pages 67–92, 1973. 44

[Flandin 2004] Guillaume Flandin. *Utilisation d'informations géométriques pour l'analyse statistique des données d'IRM fonctionnelle*. PhD thesis, Université de Nice-Sophia Antipolis, April 2004. 131, 132

[Flasque 2000] Nicolas Flasque, Michel Desvignes, Jean-Marc Constans et Marinette Revenu. *Accurate Detection of 3D Tubular Tree Structures*. In ICIP, 2000. 54

[Frangi 1998] Alejandro F. Frangi, Wiro J. Niessen, Koen L. Vincken et Max A. Viergever. *Multiscale Vessel Enhancement Filtering*. Medical Image Computing and Computer-Assisted Intervention, pages 130–137, 1998. 54, 55

[Freedman 2004] D. Freedman, R.J. Radke, T. Zhang, Jeong Y. et Chen G.T.Y. *Model-Based Multi-Object Segmentation via Distribution Matching*. In Computer Vision and Pattern Recognition Workshop, volume 1, page 11, Washington, DC, USA, 2004. IEEE Computer Society. 48, 50, 51, 53

[Freedman 2005a] D. Freedman et T. Zhang. *Interactive Graph Cut Based Segmentation with Shape Priors*. In CVPR '05, volume 1, pages 755–762, Washington, DC, USA, 2005. IEEE Computer Society. 33, 48, 50

[Freedman 2005b] Daniel Freedman, Richard J. Radke, Tao Zhang, Yongwon Jeong, D. Michael Lovelock et George T. Y. Chen. *Model-based segmentation of medical imagery by matching distributions*. IEEE Transactions on Medical Imaging, vol. 24, no. 3, pages 281–292, 2005. 45, 53

[Fridman 2004] Y. Fridman, S.M. Pizer, S. Aylward et E. Bullitt. *Extracting branching tubular object geometry via cores*. Medical Image Analysis, vol. 8, no. 3, pages 176–196, 2004. 55

[Gao 2007] Z. Gao, D. Wilkins, L. Eapen, C. Morash, Y. Wassef et L. Gerig. *A study of prostate delineation referenced against a gold standard created from the visible human data*. Radiotherapy and Oncology, pages 239–246, 2007. 32

[Ge 1999] Y. Ge, D.R. Stelts, J. Wang et D. Vining. *Computing the centerline of a colon: a robust and efficient method based on 3D skeletons*. Journal of Computer Assisted Tomography, vol. 23, no. 5, pages 786–794, 1999. 54

[Geman 1984] S. Geman et D. Geman. *Stochastic relaxation, Gibbs distributions, and the Bayesian restoration of images*. IEEE Trans. Pattern Anal. Machine Intell., vol. 6, no. 6, pages 721–741, Nov. 1984. 43

[Ghosh 2006] P. Ghosh et M. Mitchell. *Segmentation of medical images using a genetic algorithm.* In Genetic and Evolutionary Computation Conference, pages 1171–1178, New York, NY, USA, 2006. ACM Press. 50

[Gibou 2005] F. Gibou, D. Levy et C. Cárdenas. *Partial differential equations–based segmentation for radiotherapy treatment planning.* Mathematical biosciences and engineering, vol. 2, no. 2, pages 209–226, 2005. 48, 52

[Goldszal 1998] A. Goldszal, C. Davatzikos, D. L. Pham, M. X. H. Yan, R. N. Bryan et S. M. Resnick. *An Image Processing System for Qualitative and Quantitative Volumetric Analysis of Brain Images.* J. Comp Assist. Tomogr., vol. 22, no. 5, pages 827–837, 1998. 43

[Gonzalez 1992] R. C. Gonzalez et R. E. Woods. Digital image processing. Addison-Wesley, Reading, MA, 1992. 41

[Grosclaude 1998] P. Grosclaude, F. Menegoz, P. Schaffer, J. Mace Lesec'h, P. Arveux, G. Le Mab, M. Soulie et A. Villers. *Dépistage du cancer de la prostate (II): Le cancer de la lprostate estil un problème de sangé publique? Actualisation des chiffres d'incidence et de mortalité en France de 1982 á 1990.* Prog. Urol., vol. 7, pages 647–654, 1998. 11

[Guckenberger 2006] M. Guckenberger, J. Meyer, K. Baier, D. Vordermark et M. Flentje. *Distinct effects of rectum delineation methods in 3D–conformal vs. IMRT treatment planning of prostate cancer.* Radiation Oncol, vol. 1, pages 1–34, 2006. 101

[Haken 1991] R.K. Ten Haken, J.D. Forman et D.K. Heimburge . *Treatment planning issues related to prostate movement in response to differential filling of the rectum and the bladder.* Int. J. Radiation Oncology. Biol. Phys., vol. 1, pages 1317–1324, 1991. 33

[Haralick 1985] R M Haralick et L G Shapiro. *Image segmentation techniques.* CVGIP, vol. 29, pages 100–132, 1985. HARALICK85. 41

[Held 1997] K. Held, Elena Rota Kops, Bernd J. Krause, William M. Wells-III, Ron Kikinis et Hans-Wilhelm Mller-Gï£¡tner. *Markov Random Field Segmentation of Brain MR Images.* Rapport technique, Institute of Medicine. Research Center Jlich GmbH, 1997. 43

[Hernandez 2004] M. Hernandez et A.F. Frange. *Geodesic active regions using non–parametric statistical regional description and their application to aneurysm segmentation from CTA.* Medical Imaging and Augmented Reality. In: Lecture Notes in Computer Science (LNCS), vol. 3150, pages 94–102, 2004. 55

[Huang 2004] Xiaolei Huang, Dimitris N. Metaxas et Ting Chen. *MetaMorphs: Deformable Shape and Texture Models.* In CVPR (1), pages 496–503, 2004. 45

[Huttenlocher 1993] D. P. Huttenlocher, G. A. Klanderman et W. A. Rucklidge. *Comparing Images Using the Hausdorff Distance*. IEEE Trans. Pattern Anal. Mach. Intell., vol. 15, no. 9, pages 850–863, 1993. 80, 82

[ICR 1993] *Prescribing, Recording and Reporting Photon Beam Therapy*. ICRU Report 50, vol. 1, no. 50, 1993. 25

[ICR 1999] *Prescribing, Recording and Reporting Photon Beam Therapy*. ICRU Report, vol. 1, no. 62, 1999. 25

[Jain 1988] Anil K. Jain et Richard C. Dubes. Algorithms for clustering data. Prentice Hall, 1988. Jain. 42

[Jemal 2002] Ahmedin Jemal, Andrea Thomas, Taylor Murray et Michael Thun. *Cancer statistics, 2002*. CA Cancer J Clin, vol. 52, no. 1, pages 23–47, Jan-Feb 2002. Erratum in CA Cancer J Clin 2002 May-Jun;52(3):181-2. 11

[Jolliffe 2002] I.T. Jolliffe. Principal component analysis. Springer, 2002. 90

[Kass 1988] M. Kass, A. Witkin et D. Terzopoulos. *Snakes: Active Contour Models*. International Journal of Computer Vision, vol. 1, pages 321–331, 1988. 3, 44, 45

[Khoo 1999] V.S. Khoo, D.P. Dearnaley, D.J. Finnigan, A. Padhani, S.F. Tanner et M.O. Leach. *Magnetic resonance imaging (MRI): considerations and applications in radiotherapy treatment planning*. Radiother Oncol, vol. 42, pages 1–15, 1999. 34

[Kirbas 2004] Cemil Kirbas et Francis Quek. *A review of vessel extraction techniques and algorithms*. ACM Computing Surveys., vol. 36, no. 2, pages 81–121, June 2004. 54

[Koss 1999] J. E. Koss, F. D. Newman, T. K. Johnson et D. L. Kirch. *Abdominal organ segmentation using texture transforms and a Hopfield neural network*. IEEE Trans. Med. Imaging, vol. 18, no. 7, pages 640–648, 1999. 43

[Krissian 2000] K. Krissian, G. Malandain, N. Ayache, R. Vaillant et Y. Trousset. *Model-Based Detection of Tubular Structures in 3D Images*. Computer Vision and Image Understanding, vol. 80, no. 2, pages 130–171, 2000. 55

[Kupelian 2005] P. Kupelian, D. Kuban, H. Thames et L. Levy . *Improved biochemical relapse–free survival with increased external radiation doses in patients with localized prostate cancer: The combined experience of nine institutions in patients treated in 1994 and 1995*. Int. J. Radiation Oncology. Biol. Phys., vol. 2, pages 415–419, 2005. 29

[Lawton 1991] CA Lawton, M Won et MV Pilepich. *Long-term treatment sequelae following external beam irradiation for adenocarcinoma of the prostate:*

analysis of RTOG studies 7506 and 7706. Int J Radiat Oncol Biol Phys., vol. 21, pages 935–939, 1991. 30, 31

[Lecellier 2006] François Lecellier, Stéphanie Jehan-Besson, Jalal Fadili, Gilles Aubert, Marinette Revenu et Eric Saloux. *Region-Based Active Contour with Noise and Shape Priors.* In ICIP, pages 1649–1652. IEEE, 2006. 45

[Lee 1996a] W.R. Lee, G.E. Hanks et A.L. Hanlon . *Lateral rectal shielding reduces late rectal morbidity following high dose three–dimensional conformal radiation therapy for clinically localized prostate cancer: further evidence for a significant dose effect.* Int. J. Radiation Oncology. Biol. Phys., vol. 2, pages 251–257, 1996. 30

[Lee 1996b] WR Lee, TE Schultheiss, AL Hanlon et GE. Hanks. *Urinary incontinence following external-beam radiotherapy for clinically localized prostate cancer.* Urology, vol. 48, pages 95–99, 1996. 31

[Lee 2004] C.C. Lee et P.C. Chung. *Identifying abdominal organs using robust fuzzy inference model.* In IEEE International Conference on Networking, Sensing and Control, volume 2, pages 1289–1294, Washington, DC, USA, 2004. IEEE Computer Society. 33, 50

[Lei 1992] T Lei et W Sewchand. *Statistical approach to X-ray CT imaging and its applications in image analysis-part I: statistical analysis of X-ray CT imaging.* IEEE Tr. Med. Im., vol. 11, no. 1, page 53, March 1992. 42

[Leibel 1984] S.A. Leibel, G.E. Hanks et S. Kramer. *Patterns of care outcome studies: results of the national practice in adenocarcinoma of the prostate.* Int. J. Radiation Oncology. Biol. Phys., vol. 3, pages 401–409, 1984. 29

[Leventon 2000] Michael E. Leventon, W. Eric L. Grimson et Olivier D. Faugeras. *Statistical Shape Influence in Geodesic Active Contours.* In CVPR, pages 1316–1323. IEEE Computer Society, 2000. 45

[Li 1995] S. Z. Li. *Markov random field modeling in computer vision.* Springer-Verlag, New York, 1995. 43

[Liang 1994] Z. Liang et J. R. Macfall. *Parameter estimation and tissue segmentation from multispectral MR images.* IEEE Transactions on Medical Imaging, vol. 13, no. 3, pages 441–449, 1994. 42

[Lorenz 2000] C. Lorenz et N. Krahnstöver. *Generation of point–based 3D statistical shape models for anatomical objects.* vol. 77, pages 175–91, 2000. 90

[Maintz 1998] J. Maintz et M. Viergever. *A survey of medical image registration.* Medical Image Analysis, vol. 2, no. 1, pages 1–36, 1998. 45

[Malsch 2006] Urban Malsch, Christian Thieke et Rolf Bendl. *Fast Elastic Registration for Adaptive Radiotherapy.* In Rasmus Larsen, Mads Nielsen et Jon Sporring, editeurs, Medical Image Computing and Computer-Assisted Intervention, volume 4191 of *Lecture Notes in Computer Science*, pages 612–619. Springer, 2006. 50

[Manly 2004] B.F.J. Manly. Multivariate statistical methods: A primer. Chapman and Hall/CRC, 3rd edn. édition, 2004. 90

[Marchal 2005] Maud Marchal, Emmanuel Promayon et Jocelyne Troccaz. *Simulating Complex Organ Interactions: Evaluation of a Soft Tissue Discrete Model.* In George Bebis, Richard D. Boyle, Darko Koracin et Bahram Parvin, editeurs, ISVC, volume 3804 of *Lecture Notes in Computer Science*, pages 175–182. Springer, 2005. 48

[Mazonakis 2001] M. Mazonakis, J. Damilakis, H. Varveris, P. Prassopoulos et N. Gourtsoyiannis. *Image segmentation in treatment planning for prostate cancer using the region growing technique.* Br J Radiol, vol. 74, no. 879, pages 243–8, March 2001. 47, 50, 52

[McInerney 1996] T. McInerney et D. Terzopoulos. *Deformable Models in Medical Image Analysis: a survey.* In Proceedings of the IEEE Workshop on Mathematical Methods in Biomedical Image Analysis, pages 171–180, San Francisco, CA, USA, June 1996. 3, 44

[Melian 1997] E. Melian, G.S. Mageras et Z. . Fuks. *Variation in prostate position quantitation and implications for three-dimensional conformal treatment planning.* Int. J. Radiation Oncology. Biol. Phys., vol. 1, pages 73–81, 1997. 33

[Metaxas 1993] D. Metaxas et D. Terzopoulos. *Shape and Nonrigid Motion Estimation through Physics-Based Synthesis.* IEEE Transactions on Pattern Analysis and Machine Intelligence, vol. 15, no. 6, pages 580–591, 1993. 44

[Michalski 2003] JM Michalski, K Winter et JA Purdy. *Preliminary evaluation of low-grade toxicity with conformal radiation therapy for prostate cancer on RTOG 9406 dose levels I and II.* Int J Radiat Oncol Biol Phys., vol. 56, pages 192–198, 2003. 30

[Michalski 2006] J.M. Michalski, M. Roach et G. Merrick . *External beam radiation therapy treatment planning for clinically localized prostate cancer.* Expert Panel on Radiation Oncology-Prostate. Online publication, 2006. 29

[Montagnat 1998] J. Montagnat et H. Delingette. *Globally constrained deformable models for 3D object reconstruction.* Signal Processing, vol. 71, no. 2, pages 173–186, December 1998. 74

[Montagnat 1999a] J. Montagnat. *Modéles déformables pour la segmentation et la modélisation d'images médicales 3D et 4D*. Thèse de sciences, Université de Nice-Sophia Antipolis, December 1999. 4, 75

[Montagnat 1999b] Johan Montagnat, Hervé Delingette et Grégoire Malandain. *Cylindrical Echocardiographic Image Segmentation Based on 3D Deformable Models*. In Medical Image Computing and Computer-Assisted Intervention, pages 168–175, 1999. 55

[Montagnat 2001] J. Montagnat, H. Delingette et N. Ayache. *A review of deformable surfaces: topology, geometry and deformation*. Image and Vision Computing, vol. 19, no. 14, pages 1023–1040, December 2001. 44

[Mumford 1989] D. Mumford et J. Shah. *Optimal Approximations by Piecewise Smooth Functions and Associated Variational Problems*. Comm. Pure Appl. Math, vol. 42, pages 577–684, 1989. 44, 45

[National Comprehensive Cancer Network 2007] Inc. National Comprehensive Cancer Network. *NCCN Clinical Practice Guidelines in Oncology: Prostate Cancer v.1.2007*. 2007. 14

[Oh 1999] C.E. Oh, K. Antes et M. Darby . *Comparison of 2D conventional, 3D conformal, and intensity–modulated treatment planning techniques for patients with prostate cancer with regard to target–dose homogeneity and dose to critical, uninvolved structures*. Int. J. Radiation Oncology. Biol. Phys., vol. 4, pages 255–263, 1999. 30

[Ohno-Machado 1999] L. Ohno-Machado et T. Rowland. *Neural network applications in physical medicine and rehabilitation*. Am. J. Phys. Med. Rehab., vol. 78, pages 392–398, 1999. 44

[Osher 1988] Stanley Osher et James A. Sethian. *Fronts propagating with curvature-dependent speed: algorithms based on Hamilton-Jacobi formulations*. J. Comput. Phys., vol. 79, no. 1, pages 12–49, 1988. 44

[Osher 2003] Stanley Osher et N. Paragios. Geometric level set methods in imaging, vision and graphics. Springer, 2003. OShE st 03:2 1.Ex. 44

[Paik 1998] D.S. Paik, C.F. Beaulieu, R. Brooke Jeffrey, G.D. Rubin et S. Napel. *Automated path planning for virtual endoscopy*. Medical Physics, vol. 25, pages 629–637, 1998. 54

[Pappas 1992] T. N. Pappas. *An adaptive clustering algorithm for image segmentation*. Signal Processing, IEEE Transactions on Signal Processing, vol. 40, no. 4, pages 901–914, 1992. 43

[Paragios 2000] Nikos Paragios et Rachid Deriche. *Geodesic Active Regions and level set methods: contributions and applications in artificial vision*. Ph.D. thesis, University of Nice Sophia–Antipolis, France., 2000. 55

[Paragios 2002] N. Paragios et R. Deriche. *Geodesic active regions: a new paradigm to deal with frame partition problems in computer vision.* Journal of Visual Communication and Image Representation, Special Issue on Partial Differential Equations in Image Processing, Computer Vision and Computer Graphics, vol. 13, no. 1/2, pages 249–268, march/june 2002. 51

[Park 2003] Hyunjin Park, Peyton Bland et Charles R. Meyer. *Construction of an Abdominal Probabilistic Atlas and its Application in Segmentation.* IEEE Trans. Med. Imaging, vol. 22, no. 4, pages 483–492, 2003. 46

[Peeters 2006] S.T. Peeters, J.V. Lebesque et W.D. Heemsbergen . *Localized volume effects for late rectal and anal toxicity after radiotherapy for prostate cancer.* Int J Radiat Oncol Biol Phys., vol. 4, pages 1151–61, 2006. 102

[Pekar 2004] V. Pekar, T.R. McNutt et M.R. Kaus. *Automated model–based organ delineation for radiotherapy planning in prostatic region.* vol. 60, pages 973–80, 2004. 50, 90

[Pichon 2004] E. Pichon, A. Tannenbaum et R. Kikinis. *A statistically based flow for image segmentation.* Medical Image Analysis, vol. 8, pages 267–274, 2004. 55

[Pilepich 1988] MV. Pilepich. *Radiation Therapy Oncology Group studies in carcinoma of the prostate. NCI Monogr.* Int J Radiat Oncol Biol Phys., vol. 7, pages 61–65, 1988. 30, 31

[Pizer 2003] Stephen M. Pizer, P. Thomas Fletcher, Sarang Joshi, Andrew Thall, James Z. Chen, Yonatan Fridman, Daniel S. Fritsch, A. Graham Gash, John M. Glotzer, Michael R. Jiroutek, Conglin Lu, Keith E. Muller, Gregg Tracton, Paul Yushkevich et Edward L. Chaney. *Deformable M-Reps for 3D Medical Image Segmentation.* Int. J. Comput. Vision, vol. 55, no. 2-3, pages 85–106, 2003. 55

[Pizer 2005] Stephen M Pizer, P Thomas Fletcher, Sarang Joshi, A Graham Gash, Joshua Stough, Andrew Thall, Gregg Tracton et Edward L Chaney. *A method and software for segmentation of anatomic object ensembles by deformable M–Reps.* Med Phys, vol. 32, no. 5, pages 1335–45, May 2005. 51

[Pollack 2002] A Pollack, GK Zagars et G Starkschall. *Prostate cancer radiation dose response: results of the M.D. Anderson phase III randomized trial.* Int J Radiat Oncol Biol Phys., vol. 53, pages 1097–1105, 2002. 30, 31

[Potosky 2004] AL Potosky, WW Davis et RM Hoffman. *Five-year outcomes after prostatectomy or radiotherapy for prostate cancer: the Prostate Cancer Outcomes Study.* J Natl Cancer Inst., vol. 96, pages 1358–1367, 2004. 32

[Rajapakse 1997] Jagath C. Rajapakse, Jay N. Giedd et Judith L. Rapoport. *Statistical Approach to Segmentation of Single-Channel Cerebral MR Images.* IEEE Trans. Med. Imaging, vol. 16, no. 2, pages 176–186, 1997. 43

[Ripoche 2004] X. Ripoche, J. Atif et A. Osorio. *A 3D discrete deformable model guided by mutual information for medical image segmentation.* In Proceedings of the Medical Imaging Conference 2004. SPIE, 2004. 48, 50

[Roach 2004] M Roach, K Winter et JM Michalski. *Penile bulb dose and impotence after three-dimensional conformal radiotherapy for prostate cancer on RTOG 9406: findings from a prospective, multi-institutional, phase I/II doseescalation study.* Int J Radiat Oncol Biol Phys., vol. 60, pages 1351–1356, 2004. 31

[Robinson 1997] JW Robinson, MS Dufour et TS. Fung. *Erectile functioning of men treated for prostate carcinoma.* Cancer, vol. 79, pages 538–544, 1997. 31

[Ron 1994] vol. 13, no. 2, pages 229–251, October 1994. 45

[Rousson 2003] M. Rousson, T. Brox et R. Deriche. *Active unsupervised texture segmentation on a diffusion based feature space.* IEEE Comput. Vis. Pattern Recognition, 2003. 55

[Rousson 2004] Mikael Rousson, Nikos Paragios et Rachid Deriche. *Implicit Active Shape Models for 3D Segmentation in MR Imaging.* In Christian Barillot, David R. Haynor et Pierre Hellier, editeurs, Medical Image Computing and Computer-Assisted Intervention, volume 3216 of *Lecture Notes in Computer Science*, pages 209–216. Springer, 2004. 45

[Rousson 2005a] M. Rousson, A. Khamene, M. Diallo, J.C. Celi et F. Sauer. *Constrained Surface Evolutions for Prostate and Bladder Segmentation in CT Images.* In Yanxi Liu, Tianzi Jiang et Changshui Zhang, editeurs, CVBIA, volume 3765 of *Lecture Notes in Computer Science*, pages 251–260. Springer, 2005. 48, 50, 57, 88

[Rousson 2005b] Mikael Rousson et Daniel Cremers. *Efficient Kernel Density Estimation of Shape and Intensity Priors for Level Set Segmentation.* In James S. Duncan et Guido Gerig, editeurs, Medical Image Computing and Computer-Assisted Intervention (2), volume 3750 of *Lecture Notes in Computer Science*, pages 757–764. Springer, 2005. 45

[Ryu 2002] JK Ryu, K Winter et JM Michalski. *Interim report of toxicity from 3D conformal radiation therapy (3D-CRT) for prostate cancer on 3DOG/RTOG 9406, level III (79.2 Gy).* Int J Radiat Oncol Biol Phys., vol. 54, pages 1036–1046, 2002. 30, 31

[Saarnak 2000] A. E. Saarnak, M. Boersma, B. N. van Brunningen, R. Wolterink et M. J. Steggerd. *Interobserver variation in delineation of bladder and rectum*

contours for brachytherapy of cervical cancer . Radiother Oncol., vol. 42, pages 37–42, 2000. 40

[Sahoo 1988] P. K. Sahoo, S. Soltani, A. K. C. Wong et Y. C. Chen. *A Survey of Thresholding Techniques*. j-CVGIP, vol. 41, no. 2, pages 233–260, February 1988. 41

[Santamaría-Pang 2007] A. Santamaría-Pang, C.M. Colbert, P. Saggau et I.A. Kakadiaris. *Automatic Centerline Extraction of Irregular Tubular Structures Using Probability Volumes from Multiphoton Imaging*. In Nicholas Ayache, Sébastien Ourselin et Anthony Maeder, editeurs, Medical Image Computing and Computer-Assisted Intervention, volume 4792 of *LNCS*, pages 486–494. Springer, 2007. 54

[Schalkoff 1992] R J Schalkoff. Pattern recognition: Statistical, structural and neural approaches. Wiley, New York, 1992. 42

[Schild 1993] S.E. Schild, H.E. Casale et L.P. Bellefontaine. *Movements of the prostate due to rectal and bladder distention: Implications for radiotherapy*. Med. Dosim., vol. 18, pages 13–15, 1993. 33

[Schultheiss 1997] T.E. Schultheiss, W.R. Lee et M.A. Hunt . *Late GI and GU complications in the treatment of prostate cancer*. Int. J. Radiation Oncology. Biol. Phys., vol. 1, pages 3–11, 1997. 29

[Sethian 2001] James A. Sethian. Level set methods and fast marching methods. Cambridge University Press, 2001. Sethian. 44

[Sezgin 2004] M. Sezgin et B. Sankur. *Survey over image thresholding techniques and quantitative performance evaluation*. J. Electron. Imaging, vol. 1, no. 13, pages 146–165, 2004. 41

[Silva 2004] A.O. Silva, J.F.C. Wanderley, A.N. Freitas, H.D.F. Bassani, R.A. de Vasconcelos et F.M.O. Freitas. *Watershed transform for automatic image segmentation of the human pelvic area*. In ICASSP 2004: Proceedings of the International Conference on Acoustics, Speech, and Signal Processing., volume 5, pages 597–600. IEEE, 2004. 52

[Society 2007] American Cancer Society. *Cancer Facts and Figures 2007*. 2007. 11, 12

[Sonka 2000] Milan Sonka et J. Michael Fitzpatrick. Handbook of medical imaging - medical image processing and analysis, volume 2. SPIE Press, 2000. 39

[Staib 1992] L. H. Staib et J. S. Duncan. *Boundary Finding with Parametrically Deformable Models*. IEEE Trans. Pattern Anal. Machine Intell., vol. 14, no. 11, pages 1061–1075, 1992. 44

[Stough 2007] J.V. Stough, R.E. Broadhurst, S.M. Pizer et E.L. Chaney. *Clustering on local appearance for deformable model segmentation.* ISBI, pages 960–963, 2007. 48

[Suri 2002] Jasjit S. Suri, Kecheng Liu, Sameer Singh, Swamy Laxminarayan, Xiaolan Zeng et Laura Reden. *Shape recovery algorithms using level sets in 2-D/3-D medical imagery: a state-of-the-art review.* IEEE Transactions on Information Technology in Biomedicine, vol. 6, no. 1, pages 8–28, 2002. 44

[Tapley 1995] D.F. Tapley, T.Q. Morris et L.P. Rowland . The columbia university college of physicians and surgeons complete home medical guide. Crown Publishing Inc., New York, 1995. 42

[Terzopoulos 1987] D. Terzopoulos, A. Witkin et M. Kass. *Symmetry-Seeking Models and 3D Object Reconstruction.* International Journal of Computer Vision, vol. 1, no. 3, pages 211–221, 1987. 55

[Terzopoulos 1988] D. Terzopoulos et K. Fleisher. *Deformable Models.* Visual Computer, vol. 4, no. 6, pages 306–331, 1988. 3

[Terzopoulos 1991] D. Terzopoulos et D. Metaxas. *Dynamic 3D Models with Local and Global Deformations: Deformable Superquadrics.* IEEE Transactions on Pattern Analysis and Machine Intelligence, vol. 13, no. 7, pages 703–714, July 1991. 44

[Tsai 2003] Andy Tsai, Anthony J. Yezzi, William M. Wells III, Clare Tempany, Dewey Tucker, Ayres Fan, W. Eric L. Grimson et Alan S. Willsky. *A Shape-Based Approach to the Segmentation of Medical Imagery Using Level Sets.* IEEE Trans. Med. Imaging, vol. 22, no. 2, pages 137–154, 2003. 50

[Tsai 2004] A. Tsai, W. Wells, C. Tempany, E. Grimson et A. Willsky. *Mutual information in coupled multi-shape model for medical image segmentation.* Medical Image Analysis, vol. 8, no. 4, pages 429–445, December 2004. 45, 52

[Unal 2005] G. Unal et G. Slabaugh. *Coupled PDEs for Non-Rigid Registration and Segmentation.* In CVPR '05, volume 1, pages 168–175, Washington, DC, USA, 2005. IEEE Computer Society. 47, 50

[van Dalen J.A.] van Dalen J.A., Huisman H.J., Welmers A. et Barentsz J.O. *Semi–automatic Image Registration of MRI to CT Data of the Prostate Using Gold Markers as Fiducials.* In Biomedical Image Registration. Lecture Notes in Computer Science, Springer Berlin / Heidelberg. 34

[van Herk 1995] M. van Herk, A. Bruce, APG Kroes, T Shouman, A Touw et JV. Lebesque. *Quantification of organ motion during conformal radiotherapy of the prostate by three-dimensional image registration.* Int. J. Radiation Oncology. Biol. Phys., vol. 1, pages 1311–1320, 1995. 33

[van Herk 1998] M. van Herk, JC de Munck, JV Lebesque, S Muller, C Rasch et A. Touw. *Automatic registration of pelvic computed tomography data and magnetic resonance scans including a full circle method for quantitative accuracy evaluation.* Med Phys, vol. 25, no. 10, pages 2054–2067, May 1998. 34

[Van Leemput 1999] K. Van Leemput, F. Maes, D. Vandermeulen et P. Suetens. *Automated model-based tissue classification of MR images of the brain.* IEEE Trans Med Imaging, vol. 18, no. 10, pages 897–908, October 1999. 131

[Vese 2002] Luminita A. Vese et Tony F. Chan. *A Multiphase Level Set Framework for Image Segmentation Using the Mumford and Shah Model.* Int. J. Comput. Vision, vol. 50, no. 3, pages 271–293, 2002. 51

[Vilariño 2003] David López Vilariño, Diego Cabello, Xose Manuel Pardo et Victor M. Brea. *Cellular neural networks and active contours: a tool for image segmentation.* Image Vision Comput., vol. 21, no. 2, pages 189–204, 2003. 43

[Vincent 1991] L. Vincent et P. Soille. *Watersheds in digital spaces: an efficient algorithm based on immersion simulations.* IEEE Transactions on Pattern Analysis and Machine Intelligence, vol. 13, no. 6, pages 583–598, June 1991. 41

[Volkau 2005] I. Volkau, Z. Weili, R. Baimouratov, A. Aziz et W.L. Nowinski. *Geometric modeling of the human normal cerebral arterial system.* IEEE Transactions on Medical Imaging, vol. 24, no. 4, pages 529–539, 2005. 55

[Warfield 2004] S.K. Warfield, K.H. Zou et W.M. Wells. *Simultaneous truth and performance level estimation (STAPLE): an algorithm for the validation of image segmentation.* IEEE Trans. Med. Imaging, vol. 23, no. 7, pages 903–921, 2004. 96, 97, 131

[Wei 2002] JT Wei, RL Dunn et HM Sandler. *Comprehensive comparison of health-related quality of life after contemporary therapies for localized prostate cancer.* J Clinical Oncology, vol. 20, pages 557–566, 2002. 32

[Wernicke 2004] AG Wernicke, R Valicenti, K Dieva, C Houser et E. Pequignot. *Radiation dose delivered to the proximal penis as a predictor of the risk of erectile dysfunction after three-dimensional conformal radiotherapy for localized prostate cancer.* Int J Radiat Oncol Biol Phys., vol. 60, pages 1357–1363, 2004. 31

[Wink 2004] O. Wink, W.J. Niessen et M.A. Viergever. *Multiscale vessel tracking.* IEEE Trans. Med. Imaging, vol. 23, no. 4, pages 130–133, 2004. 54, 55

[Xiao 2001] Di Xiao, Wan Sing Ng et U.R. . Abeyratne. *Rectal wall structure delineation and broken layer recognition by multigradient field active contour.* In

The Seventh Australian and New Zealand Intelligent Information Systems Conference, pages 123–127, 2001. 53

[Xu 1998] C. Xu et J. L. Prince. *Snakes, Shapes, and Gradient Vector Flow*. Transactions on Image Processing, vol. 7, no. 3, pages 359–369, 1998. 44

[Xu 2003] W. Xu, S.A. Amin, O.C.L. Haas et J.A. Mills. *Contour detection by using radial searching for CT images*. In 4th International IEEE EMBS Special Topic Conference on Information Technology Applications in Biomedicine, pages 346–349, Washington, DC, USA, 2003. IEEE Computer Society. 50

[Yezzi 2002] A.J. Yezzi Jr., A. Tsai et A.S. Willsky. *A Fully Global Approach to Image Segmentation via Coupled Curve Evolution Equations*. Journal of Visual Communication and Image Representation, vol. 13, no. 1/2, pages 195–216, March 2002. 51

[Yim 2001] P.J. Yim, J.R. Cebral, R. Mullick, H.B. Marcos et P.L. Choyke. *Vessel surface reconstruction with a tubular deformable model*. IEEE Transactions on Medical Imaging, vol. 20, no. 12, pages 1411–1421, 2001. 55

[Zadeh 1965] L.A. Zadeh. *Fuzzy Sets*. Information Control, vol. 8, pages 338–353, 1965. 42

[Zaim 2005] Amjad Zaim et Jerzy Jankun. *A Kohonen Clustering based Approach to Segmentation of Prostate from TRUS Data using Gray-Level Co-occurrence Matrix*. In M. H. Hamza, editeur, Computer Graphics and Imaging, pages 66–69. IASTED/ACTA Press, 2005. 43

[Zelefsky 1998] MJ Zelefsky et JF. Eid. *Elucidating the etiology of erectile dysfunction after definitive therapy for prostatic cancer*. Int J Radiat Oncol Biol Phys., vol. 40, pages 129–133, 1998. 31

[Zelefsky 2000] M.J. Zelefsky, Z. Fuks et L. Happersett . *Clinical experience with intensity modulated radiation therapy (IMRT) in prostate cancer*. Int. J. Radiation Oncology. Biol. Phys., vol. 3, pages 241–249, 2000. 30

[Zelefsky 2001] MJ Zelefsky, Z Fuks et M Hunt. *High dose radiation delivered by intensity modulated conformal radiotherapy improves the outcome of localized prostate cancer*. Journal of Urology, vol. 166, pages 876–881, 2001. 30, 31

[Zelefsky 2002] M.J. Zelefsky, Z. Fuks et H. Hunt. *High–dose intensity modulated radiation therapy for prostate cancer: early toxicity and biochemical outcome in 772 patients*. Int. J. Radiation Oncology. Biol. Phys., vol. 5, pages 1111–1116, 2002. 30

[Zhang 1994] Zhengyou Zhang. *Iterative point matching for registration of free-form curves and surfaces*. Int. J. Comput. Vision, vol. 13, no. 2, pages 119–152, 1994. 75

[Zhu 1995] S.C. Zhu, T.S. Lee et A. Yuille. *Region Competition: Unifying Snakes, Region Growing Energy/Bayes/Mdl For Multi-Band Image Segmentation.* In ICCV 95, pages 416–423, 1995. 45

[Zimmer 2005] Christophe Zimmer et Jean-Christophe Olivo-Marin. *Coupled Parametric Active Contours.* IEEE Transactions on Pattern Analysis and Machine Intelligence, vol. 27, no. 11, pages 1838–1842, 2005. 50

[Zwiggelaar 2003] Reyer Zwiggelaar, Yanong Zhu et Stuart Williams. *Semi–automatic Segmentation of the Prostate.* In Francisco J. Perales López, Aurélio C. Campilho, Nicolas Pérez de la Blanca et Alberto Sanfeliu, editeurs, IbPRIA, volume 2652 of *Lecture Notes in Computer Science*, pages 1108–1116. Springer, 2003. 50